Magnetic antiskyrmions in tetragonal Heusler materials with D_{2d} structure

Dissertation

zur Erlangung des Doktorgrades der Naturwissenschaften
(Dr. rer. nat.)

der

Naturwissenschaftlichen Fakultät II
Chemie, Physik und Mathematik

der Martin-Luther-Universität
Halle-Wittenberg

vorgelegt von

Herrn Tianping Ma
geb. am 13.10.1988 in Nanjing, China

Gutachter:

Prof. Dr. Stuart S. P. Parkin

Prof. Dr. G. Woltersdorf

Prof. Dr. D. Süss

Tag der öffentlichen Verteidigung:

08.03.2021

Acknowledgements

First of all, I would like to express my very great appreciation to Prof. Stuart S. P. Parkin, my Ph.D. supervisor. One of my long-cherished wishes in life is to become a Physicist. By providing me the opportunity to join his group at MPI-Halle, Prof. Parkin helped me to get closer to this goal. Under his supervision, I got a chance to study the cutting edge topics such as current-induced domain wall motion and antiskyrmion. He always proposes exciting new ideas and provides substantial support to achieve them. His hard-working attitude and enthusiastic spirit inspired me a lot.

Besides, I am grateful to Prof. Georg Woltersdorf, my co-supervisor at the International Max Planck Research School for Science and Technology of Nano-Systems (IMPRS-STNS). He provided me guidance throughout my Ph.D., especially during my first year.

Another thank you goes to Prof. Yizheng Wu and Prof. Haibin Zhao for their commitment in publishing jointly the results of my master's project. Even beyond my master's degree, they provided valuable advices during our scientific discussions.

A special thank you goes to my colleagues from the IBM Almaden Research Center in Almaden, including See-Hun Yang, Chirag Garg, Timothy Phung, et al. All of them provided significant help, especially with the set-up of the Kerr microscope systems.

Next, I want to thank my colleagues from MPI-Halle, including Fasil Kidane Dejene, Kumari Rana Gaurav, Neeraj Kumar, Simone Altendorf, Hakan Deniz, Kai Chang, Peter Werner, Edouard Lesne, et al. They taught me a lot, and it was a pleasant experience working together with them.

I enjoyed a lot working with Ajaya Nayak, Rana Saha, Abhay Kant Srivastava, Ankit Sharma, Jagannath Jena, and Börge Göbel on the antiskyrmion project; with Robin Bläsing, Yicheng Guan, Xilin Zhou, Fang Gao, Jae-Chun Jeon, Jiho Yoon, and Andrea Migliorini et al. on thee racetrack project; and with Bharat Grover, Binoy Krishna Hazra, Samiran Choudhury, et al. on the ultrafast time-resolved magnetism project.

I want to thank Winfried Heichler, Pierre-Jean Zermatten, Dirk Sander, René Kunze, and technicians of MPI-Halle, who provided me constant help so that the lab could run smoothly.

I want to thank Yan Sun, Vivek Kumar, Roshnee Sahoo, Prof. Claudia Felser, and other collaborators from the Max Planck Institute for Chemical Physics of Solids in Dresden. Our collaboration, especially the high-quality single-crystal sample provided by them, played a key role in the antiskyrmion experiments.

A carefully organized administrative infrastructure ensured always a good atmosphere and helped me to overcome hurdles that scientists sometimes would just overlook. Therefore, I would like to thank Simone Jäger and Antje Paetzold for their valuable support, event organization and Beyond!

Finally, I would like to thank my parents and friends for their support during all these years of my academic training and respecting my wish to become a Physist.

Abstract

Within the last decades, various types of magnetic skyrmions were experimentally discovered, and their static and dynamical properties were intensively studied. This trend continues, and the Zootopia of skyrmions is still expanding. In this thesis, we investigated magnetic antiskyrmions in tetragonal Heusler materials with the D_{2d} structure, initiated with the first experimental discovery of magnetic antiskyrmions above room temperature, as well as several follow up studies, all performed during my Ph.D. study. Magnetic antiskyrmions have a special chirality that originates from the underlying D_{2d} crystal structure. The in-plane magnetization of the anti-skyrmion rotates in the opposite direction with respect to the coordinate azimuthal angle. Such chiral structures give rise to a boundary of the antiskyrmion that has alternating Bloch and Néel type walls with opposite chiralities. This special structure of the anti-skyrmion leads to its high stability and its rich dynamical behavior under current-induced spin Hall injection. These properties make anti-skyrmions highly interesting for next generation spintronic devices.

This thesis is organized as follows. In the 1st chapter the background information of the development of skyrmions is introduced. In the 2nd and 3rd chapters the basic theory of skyrmions, the micromagnetic simulation methods, and various experimental techniques (especially Lorentz transmission electron microscopy (**LTEM**)) related to the skyrmion studies are summarized. In the 4th chapter the first experimental work on the discovery of magnetic antiskyrmions is discussed. A unique 4-spot LTEM pattern with alternating black and white contrast confirms the existence of antiskyrmions. The 5th chapter contains follow-up studies on the intrinsic stability of antiskyrmions. Due to the zero value of the Dzyaloshinskii–Moriya interaction (**DMI**) along the [001] crystal direction, the thickness-dependent phase diagram shows distinct behavior as compared to other skyrmion systems, e.g., the B20 Bloch skyrmion system. In the 6th chapter our work on the wide-range tunability of the antiskyrmion size and helix period is presented. Due to the significant influence of both the DMI and magnetic dipolar interactions, which is unique to the D_{2d} material system, the size of the antiskyrmion and the corresponding helix period can be tuned by up to one order of magnitude when the thickness of the host lamella varies from ~100 nm to ~4 µm. Finally, the 7th chapter presents the conclusion and outlook.

Contents

Abstract **5**

1 Introduction **11**
- 1.1 Magnetic ordering 12
- 1.2 Magnetic domain 15
- 1.3 Magnetic domain wall 16
- 1.4 Chiral magnetic domain wall 16
- 1.5 Magnetic bubble and stripe domain 19
- 1.6 Previous studies of skyrmions 19
  - 1.6.1 Early discovery of skyrmion 20
  - 1.6.2 Bloch skyrmion in B20 structure system 23
  - 1.6.3 Néel skyrmion in C_{nv} crystal structure system 26
  - 1.6.4 Skyrmion in interface system 27
  - 1.6.5 Other skyrmion systems 28
  - 1.6.6 Current induced skyrmion motion 30
- 1.7 Heusler material 31

2 Skyrmion theory and micromagnetic simulation **33**
- 2.1 Skyrmion theory 33
  - 2.1.1 Exchange interaction between two atoms 33
  - 2.1.2 Exchange interaction under different crystal symmetries 35
  - 2.1.3 Magnetic topology of skyrmion under different crystal symmetry 38
- 2.2 Micromagnetic simulation 41
  - 2.2.1 Working principle of micromagnetic simulations 41
  - 2.2.2 Popular micromagnetic simulation software 43
  - 2.2.3 Batch calculation and result analysis 44

3 Experimental techniques 47
3.1 Focused ion beam (FIB) 47
3.2 Lorentz transmission electron microscopy (LTEM) 49
3.3 Magnetic force microscope (MFM) 51
3.4 Kerr microscope 52
3.5 Scanning transmission X-ray microscope (STXM) 54

4 Magnetic antiskyrmions above room temperature in tetragonal Heusler materials 57
4.1 Material and its structure and magnetization characterization 58
4.2 Magnetic structure and LTEM pattern 59
4.3 LTEM measurement of antiskyrmion 63
4.4 Micromagnetic simulations of antiskyrmions 66
4.5 Temperature and field dependent phase diagram of antiskyrmions 68
4.6 Summary and outlook 71

5 Thickness dependent phase diagram: Intrinsic stability of magnetic antiskyrmions in the tetragonal inverse Heusler compound $\mathbf{Mn_{1.4}Pt_{0.9}Pd_{0.1}Sn}$ 73
5.1 LTEM measurement 74
5.2 Phase diagram analysis 76
5.3 Micromagnetic simulation 80
5.4 Summary 85

6 Tunable magnetic antiskyrmion size and helical period from nanometers to microns in a D_{2d} Heusler compound 87
6.1 LTEM measurement 88
6.2 MFM measurement 90
6.3 Model and calculation 94
    6.3.1 E_{Dip} for a Bloch helix 94
    6.3.2 Numerical confirmation of the E_{Dip} 95
    6.3.3 E_{Dip} for other types of helices, cycloids or in-between geometries 96
    6.3.4 Finite size effect of the dipolar interaction 99
    6.3.5 Position dependence of the magnetic dipolar energy density 100
    6.3.6 Helix wavelength calculation 102
6.4 Discussion 105

6.5 Summary 106

7 Conclusion and outlook **107**

Appendix DMI energy term under various crystal **109**

Bibliography **111**

List of figures **122**

Abbreviations **128**

Parameter definition **129**

Curriculum vitae **131**

List of publications **133**

Eidesstattliche Erklärung **137**

Chapter 1

Introduction

The performance of information processing and data storage is one of the critical indicators of the status of human technology development. Exploring novel materials and physical mechanisms which enable next generation information technology is incredibly demanding [1, 2]. For example, over the last few decades, the rise of spintronics, especially the Giant Magnetoresistance (**GMR**) effect [3, 4] has enabled a rapid increase in hard disk drive storage density and the read-out speed. Recently, progress continues to be made; for example, Magnetoresistive Random Access Memory (**MRAM**) devices are already commercially available from mainstream companies including Samsung [5].

Non-collinear nanometer-size magnetic structures are one of the major candidates for next generation spintronics technologies. The simplest 1-Dimensional non-collinear magnetic nanostructure is a magnetic domain wall (**DW**) [6], which is the transition region between two magnetic domains. With perpendicular magnetic anisotropy, the domain wall can have a width as small as a few nanometers, which allows for today's high density magnetic data storage devices. Such 1D DWs can be moved under injected current along magnetic conduits to allow them to be detected using a reading device that is integrated at a given point along the conduit. This is in contrast to today's magnetic disk drives in which the static domain walls (that are usually called ”transitions”) are embedded into a magnetic film on a disk which is moved to the reading sensor which is on a moving mechanical arm. This concept was proposed by Prof. Stuart Parkin who named it “Racetrack memory” [1]. By integrating with novel physical effects such as DMI, perpendicular magnetic anisotropy (**PMA**), Spin Hall effect (**SHE**), and synthetic antiferromagnet structure (**SAF**), Racetrack memory is already in the 4th generation. It gradually enters into the industrial application phase [7].

2-Dimensional magnetic structures are also of great interest. In early developments magnetic bubble memory was intensively investigated [6]. The magnetic bubbles are round shaped magnetic structures in which the magnetization inside and outside has opposite directions. In the last two decades, with the experimental and theoretical development of especially DMI, various types of magnetic skyrmions have been discovered [8, 9, 10]. Unlike trivial magnetic bubbles, which are achiral, the chirality of a skyrmion is determined by the DMI, which arises from the underlying crystal symmetry [11, 12]. Under the influence of DMI, the skyrmions are topologically protected; thus, on the one hand, they are much more stable and, on the other hand, enjoy a rich dynamical behavior, such as current induced motion in the Racetrack memory [13]. Skyrmions have the advantages of small size and low threshold currents for current-induced motion since they can move around pinning defects rather than overcoming them [14]. Within the last two decades, various types of skyrmions have been discovered. For example, Bloch skyrmions were discovered in B20 materials, and Néel skyrmions were discovered in C_{nv} and interface systems [10, 15]. The study of magnetic skyrmions is not only interesting for understanding the fundamental underlying physical mechanisms of these nano-size chiral magnetic structures but also will contribute to developments in technological applications, such as Racetrack memory devices.

In this chapter, I will first introduce some magnetic skyrmion related basic concepts and then summarize the progress made on research of skyrmions in the past two decades.

1.1 Magnetic ordering

The origin of magnetization comes from how the magnetic moments of atoms are aligned. Based on the ordering of atomic magnetic moments, the magnetic systems can be classified, such as diamagnetism, paramagnetism, ferromagnetism(**FM**), anti-ferromagnetism(**AFM**), and ferrimagnetism [16, 17, 18].

The phenomenon of having a magnetization in the opposite direction to the external magnetic field is called diamagnetism. It occurs in materials whose atoms have no net magnetic moment. The origin of diamagnetism is that when the magnetic field is turned on, the change in the flux of the electron orbit will induce an electromotive force which acts to oppose the change in flux, thus inducing the diamagnetic effect. This magnetism is quite weak with a magnitude around 10^{-6} per unit volume. The magnetic susceptibility is given by $\chi = -\frac{N\mu_0 Ze^2}{6m_e}\langle r^2\rangle_{av}$, where χ is the magnetic susceptibility, N is number of atoms per unit volume, $\langle r^2\rangle_{av}$ is the average value of all occupied orbital radii and Z is the number of electrons.

Paramagnetism is also a kind of weak magnetism. Generally, the amplitude of χ is between 10^{-6} to 10^{-3}. In paramagnetic materials, there is no significant interaction between magnetic particles. Under external field, the relationship between the Boltzmann factor and the magnetic moment direction is $e^{-\frac{E}{k_bT}} = e^{\frac{mHcos\theta}{k_bT}}$, where T is the temperature, m is the magnetic moment, H is the external field and θ is the angle between magnetic moment to the applied field. Then the magnetization $I = Nm(cot\alpha - \frac{1}{\alpha})$, with $\alpha = \frac{mH}{k_bT}$, where N is the number of magnetic atom. When the external field increases, so does α, thus all the magnetic moments tend to align in the same direction. It can be deduced that $\chi = \frac{I}{H} = \frac{Nm^2}{3k_bT}$, so that the magnetic susceptibility is inversely proportional to the absolute temperature T.

Distinct from diamagnetism and paramagnetism, ferromagnetism is a kind of strong magnetic behavior. In a ferromagnetic material, all the moments are almost aligned in the same direction, as shown in Fig. 1.1a. This parallel alignment of the magnetic moments induces a spontaneous magnetization. In 1907 [16, 17], Weiss proposed a mechanism for this phenomena. He assumed there is an internal “molecule field” H_m that exists between one magnetic moment and the nearby moments. He assumes the strength of the “molecular field” is proportional to the magnetization, $H_m = \omega I$. Under the influence of the external field and “molecular field”, the magnetization is $I = NmL(\alpha)$, where $L(\alpha)$ is the Langevin function. Unlike in paramagnetism, here $\alpha = \frac{m(H+I)}{k_bT}$.

Antiferromagnetism is the counterpart of ferromagnetism, as illustrated in Fig. 1.1b. In antiferromagnetism, the nearby magnetic moments are antiparallel to each other. Thus the moments cancel each other. Above the Néel temperature, the magnetic ordering disappears; thus, the behavior is the same as paramagnetism. The critical temperature of the antiferromagnetic and paramagnetic behavior is the Néel temperature point. Antiferromagnetism can further be divided into several types, such as A-type, C-type, and G-type, depending on how the magnetic moments are aligned opposite to each other [19]. In A-type antiferromagnetism, there are layers within which the magnetic moments are aligned parallel and between which the magnetic moments are antiparallel aligned. In C-type, in two directions of the crystal, the moments are antiparallel and, in the other direction, are parallel. In G-type, in all three directions, the moments are antiparallel aligned.

In ferrimagnetism, the magnetic moments are subdivided into two sublattices, as illustrated in Fig. 1.1c. Within each sublattice, the magnetic moments are ferromagnetically aligned. Between the two sublattices, the magnetic moments have different amplitudes and are antiferromagnetically aligned. In a ferrimagnet, the magnetic moments between the two sublattices are not the same, thus resulting in a non-zero net magnetization. Sometimes, ferrimagnetism can be simplified to be treated as ferromagnetism. However, sometimes the more complex ferrimagnetic magnetic structure needs to be considered. For example, the magnetization compensation temperature (the temperature when the magnetic moments are the same in the two sublattices) and the angular magnetic moment compensation temperature (the temperature where the angular magnetic moments, which are the magnetic moment divided by the g factor, are the same in the two sublattices) usually is not the same. The latter temperature is recently reported to have a high efficiency of current-induced magnetic dynamics [20]. Magnetic antiskyrmions were also discovered in a ferrimagnetic material, which will be discussed in detail in later chapters.

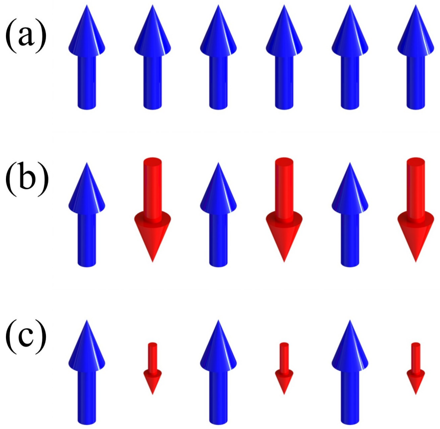

Figure 1.1: Illustration of magnetic ordering. (a) ferromagnetism, (b) antiferromagnetism and (c) ferrimagnetism.

In 1928, Heisenberg used a quantum mechanical-based concept of "exchange interaction" to explain the existence of the large-amplitude "molecular field". This effect comes from the exchange symmetry's influence on the wave function of indistinguishable particles. Due to the Pauli exclusion principle, if the spins of two electrons are antiparallel to each other, they share the same orbit. In contrast, if the two electron spins are parallel to each other, then their orbit needs to be separated in order to decrease the Coulomb interaction. The strength of the exchange interaction is related to the overlap of the electron orbits. Depending on the sign of the exchange integral, ferromagnetic or antiferromagnetic ordering is established. The origin of antiferromagnetism might also occur due to a superexchange interaction. The detailed theory of exchange interaction in various crystal structures will be discussed in chapter 2.1.2.

Besides the above magnetic ordering, there are other more complex magnetic order systems, such as helimagnetism, parasitic ferromagnetism, mictomagnetism, and spin glass etc.

1.2 Magnetic domain

On the atomic scale, due to the exchange interaction, the magnetic moments prefer to align parallel to each other in a ferromagnetic material. However, on a larger scale, the sample might be separated into lots of small magnetic regions. Within these small regions, the magnetization is the same. However, the directions of magnetization between these regions are different. This small region is the magnetic domain. A similar situation happens in ferrimagnetic and even antiferromagnetic materials.

The origin of the formation of the magnetic domain is that this lowers the energy of the whole sample system. All the magnetic moments, that are aligned in the same direction, is preferred by the exchange interaction; however, not preferred by other energy terms such as the magnetic dipolar interaction. The magnetic domain structure will be stable if it induces a lower energy of other energy terms at the cost of not too much increase in the exchange interaction energy term, thus the total energy of the system decreases. Various sample properties and external parameters influence the size of the magnetic domains. Some typical magnetic domain structures can be found in the book [21].

If we cool down the sample from above the Curie temperature to below without an external magnetic field (zero-field cooling, **ZFC**), it is more likely to be in a multi magnetic domain state. However, if we apply large enough field during the cooling procedure (field cooling, **FC**), it is more likely to be in a single magnetic domain state. For some material systems, applying an AC magnetic field with a gradually decreasing field can also lead to a multi magnetic domain state. Such behavior of the magnetic domain is complex and is a result of a competition between various energy terms. The study of these provides a way to understand the material and physical mechanisms behind them in depth.

1.3 Magnetic domain wall

The magnetic domain wall is the transition region between different magnetic domains. As there are various type of magnetic domains, there are also various type of magnetic domain walls. One of the simplest domain wall structures is in a ferromagnetic exchange coupling system with PMA. In this model, the ferromagnetic exchange interaction prefers the magnetization to align in the same direction, which means the domain wall width is infinitely long. On the other hand, the PMA prefers the magnetization to be always along the perpendicular direction. Thus, the domain wall width should be preferentially zero but the two energy terms compete with each other, resulting in a final domain wall profile [6]: $\theta(y) = \pm 2\tan^{-1}\left(e^{\frac{y}{\Delta}}\right)$ and $\phi(y) = \psi = \text{const}$, where $\Delta = \sqrt{A/K}$ is the width of the magnetic domain wall, θ and ϕ are the polar and azimuthal angles of the magnetization, A is the exchange stiffness, and K is the anisotropy. Thus, the total wall energy per unit area is $\sigma = 4\sqrt{AK}$. The detailed magnetic domain wall structure will be more complicated, for example, if we consider local magnetostatic energies, an in-plane field H_p which has origin in the XY plane at an angle ψ_H to the wall plane and in-plane anisotropy K_p which has an easy axis with an angle ψ_p to the wall plane, the magnetic domain wall width and energy will become $\Delta = \sqrt{A/\kappa}$ and $\sigma = 4\sqrt{A\kappa}$, where $\kappa = K + 2M^2\sin^2\psi + K_p\sin^2(\psi - \psi_p) - (\pi M H_p/2)\cos(\psi - \psi_H)$.

1.4 Chiral magnetic domain wall

In a perpendicularly magnetized system, the Bloch type domain wall is preferred [22]. The stabilization of Bloch type DWs is due to long-range dipolar effects. This Bloch type domain is achiral, which means the two types of Bloch wall magnetic geometry, Left-hand (**LH**) type, and Right-hand (**RH**) type, are degenerate in energy, as shown in Fig. 1.2a-b. However, recent studies [23, 24] shows that in some systems, e.g., an interface system with a heavy metal and a ferromagnetic metal heterostructure, a DMI energy term is induced that not only forces the domain wall to have a Néel type geometry, but also to have a fixed chirality, as shown in Fig. 1.2c-d.

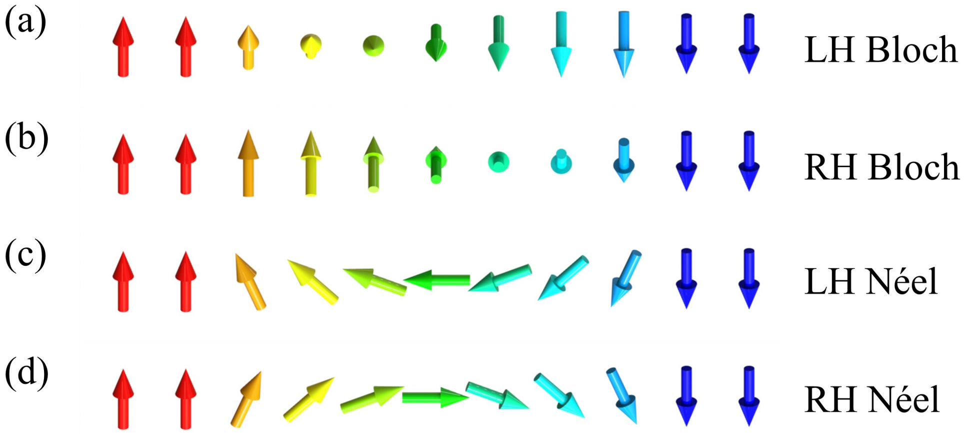

Figure 1.2: Illustration of the magnetic structure of different types of magnetic domain walls. (a) Left-hand Bloch wall, (b) Right-hand Bloch wall, (c) Left-hand Néel wall, and (d) Right-hand Néel wall.

As in my previous work [23, 24], we used a Spin-Polarized Low Energy Electron Microscope to study the domain wall chirality. In the thin-film structure of Fe (1.3ML)/Ni(10ML)/Cu(001), the domain wall is Bloch type, whereas in the structure Fe (2ML)/Ni(7ML)/Cu(001), the domain wall is Néel type with a Right-hand chirality, where **ML** is the abbreviation of the monolayer. The physics origin is that: on the one hand, the energy terms such as Heisenberg exchange, anisotropy (that have the same energy regardless of the type and chirality of the domain wall); on the other hand, the long-range dipolar interaction which prefers a Bloch wall and the interface DMI which prefers specific type chirality of the Néel type domain wall are competing. Thus, by controlling the film thickness, which corresponds to the dipolar energy, the strength of the DMI can be estimated. We also presented an experiment in which the sign of the DMI can be manipulated by thickness control in Pt/Ir heterostructures, as shown in Fig. 1.3.

The chiral domain wall provides a promising platform for novel spintronics applications, such as current-induced magnetization switching [25] and

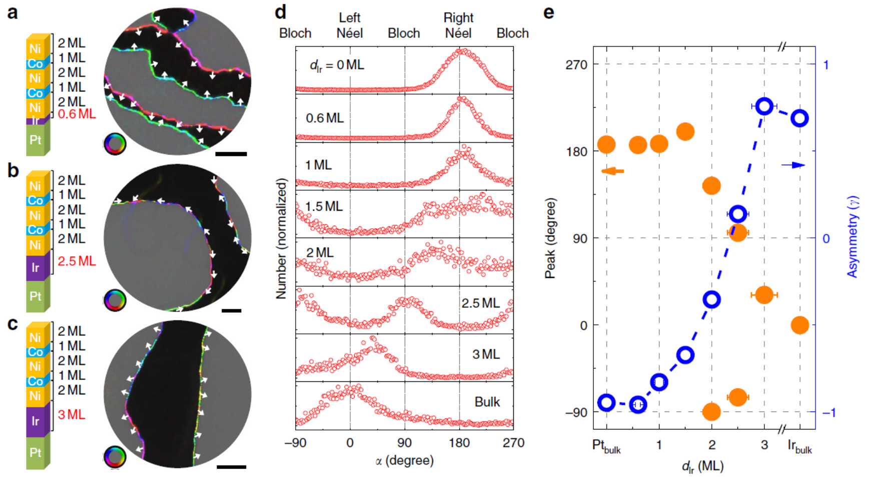

Figure 1.3: Chirality of magnetic domain wall as a function of Ir inserting layer thickness in Ni/[Co/Ni]$_2$/Ir/Pt(111) sample structure. (Material from: Chen, G., Ma, T., N'Diaye, A. T., Kwon, H., Won, C., Wu, Y., & Schmid, A. K., Tailoring the chirality of magnetic domain walls by interface engineering, Nature communications, published 2013, Springer Nature. [24])

current-induced domain wall motion in Racetrack Memory [1, 7].

1.5 Magnetic bubble and stripe domain

One type of material is called "bubble material", where bubble shape magnetic domains are stabilized. The magnetization within the bubble points up or down represents one bit of information as "0" or "1". In the 1980s, magnetic bubble material was a promising candidate for magnetic memory devices. The "bubble material" is also named as "high-Q material" [6], where Q is the "quality factor" defined as $Q = \frac{K}{2\pi M^2}$. For the bubble material, the quality factor needs to be larger than 1, the coercivity field needs to be low and the characteristic length needs to meet the size of the bubble, which was usually in the micrometer range. In the bubble material, depending on the external applied field, the magnetic structure can have several phases, such as stripe domain phase, isolated bubble phase, hexagonal bubble lattice phase, and mixtures of them.

Early research into magnetic bubble provides an important source of reference for the study of skyrmions. The stripe domain, bubble lattice, and isolated bubble phase in bubble materials have their counterpart in the helix, skyrmion lattice, and isolated skyrmion phase in skyrmion materials. However, there are some important distinctions between these two concepts. First of all, the magnetic bubble is achiral. Second, their size usually has a significant dependence on the external field, and the bubble size is much larger compared to the boundary wall width. These are usually not the case in skyrmion systems. However, the boundary of bubbles and skyrmions have some "gray zone", thus the round shape magnetic domain has both the properties of a bubble and a skyrmion. Thus it can be called an "skyrmion bubble". A typical example is the Néel skyrmion in interfacial DMI systems [26].

1.6 Previous studies of skyrmions

The magnetic domain wall is a one-dimensional topological structure in which the magnetization changes along one direction. The magnetic skyrmion is topologically more complicated as the magnetization changes in two-dimensions. Magnetic skyrmions usually have a bubble-like round shape. The boundary region, defined as the region in between the magnetic region in and out of the skyrmion, has a chirality preferred by the DMI. A skyrmion can be characterized by the topological skyrmion number as $N_{sk} = \frac{1}{4\pi} \iint \overrightarrow{M} \cdot \left(\frac{\partial \overrightarrow{M}}{\partial x} \times \frac{\partial \overrightarrow{M}}{\partial y} \right) \mathrm{d}x \, \mathrm{d}y$.

This number is widely used in studies of the static and dynamical behavior of skyrmions, such as the topological Hall effect [13, 27] and nucleation [14].

1.6.1 Early discovery of skyrmion

In 2009, the research group of Prof. C. Pfleiderer reported the observation of a skyrmion lattice by the experimental method of neutron scattering [28]. Instead of observing in real space, the neutron scattering method can provide the magnetization structure information in momentum space. They used a bulk crystal of MnSi, which has the B20 crystal structure with the size scale in millimeters. As shown in Fig. 1.4, the six peaks in the typical small-angle neutron scattering(**SNAS**) intensity indicate a magnetic modulation along all three crystal directions, thus confirming the skyrmion lattice structure.

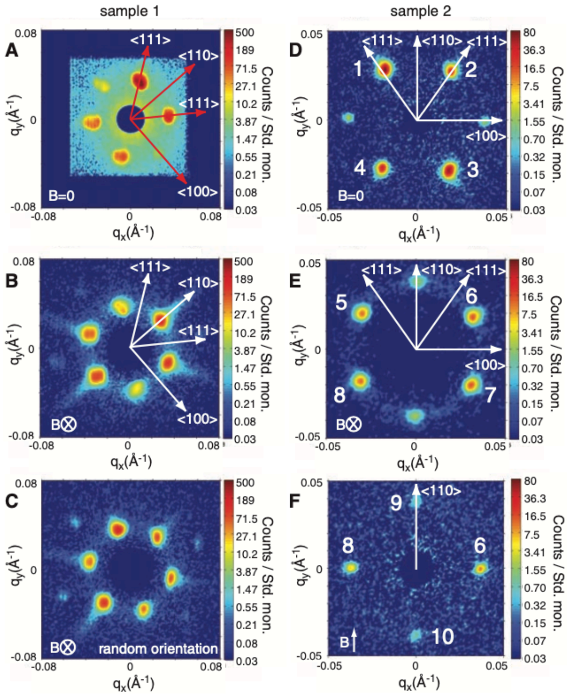

Figure 1.4: Typical neutron small-angle scattering intensity, which indicating the stabilization of skyrmion lattice. (From [28]. Reprinted with permission from AAAS.)

In 2010, the research group of Prof. Y. Tokura reported the real-space observation of a two-dimensional skyrmion crystal [8]. The material they report is a $Fe_{0.5}Co_{0.5}Si$ single-crystal grown by the floating-zone technique. The material also has a B20-type crystal structure, thus having the type of DMI which supports Bloch-type skyrmions. The crystal is then shaped into a thin lamella with the thickness less than the helical wavelength. The real-space measurement is performed by the LTEM technique, which will be introduced in detail in Chapter 3. The analytical method of solving the transport-of-intensity equation (**TIE**) is used to interpret the LTEM measurement to obtain the local magnetization distribution. They also performed a Monte Carlo simulation to reproduce the measured magnetic skyrmion structure. The magnetic structure of a helix and a Bloch skyrmion is in good agreement with the simulation results, as shown in Fig. 1.5.

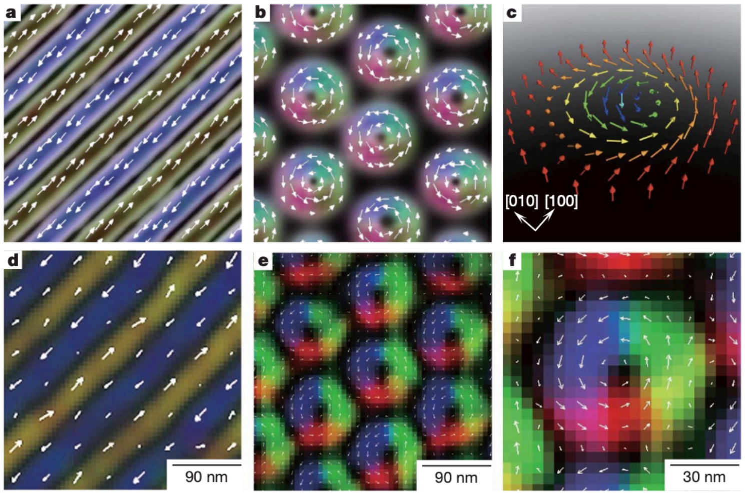

Figure 1.5: Simulation and experiment result of magnetization distribution of helix and skyrmion lattice. (Reprinted by permission from Springer Nature Customer Service Centre GmbH: Springer Nature, Nature, [8] (Real-space observation of a two-dimensional skyrmion crystal, X. Z. Yu et al.), COPYRIGHT (2010))

Furthermore, they showed the temperature and field dependence of the phase diagram of the magnetic structure. At low temperatures, the system is in a helix state when there is no external field. As the field increases, the system then gradually transitions into a helix/skyrmion mixed state, skyrmion lattice state, skyrmion/ferromagnetic mixed state, and finally a pure ferromagnetic state, when the field is strong enough. When the temperature is high enough, the skyrmion phase disappears. The simulation well reproduces the experiment results, as shown in Fig. 1.6.

This work demonstrated in real space the magnetization of Bloch type skyrmions. The experimental phase diagram behavior of skyrmions, as well

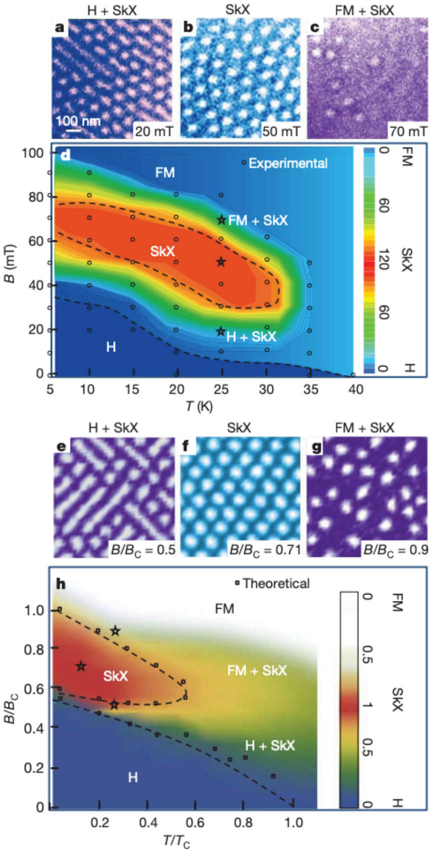

Figure 1.6: Simulation and experiment result of temperature and field dependence of the magnetic structure phase diagram. (Reprinted by permission from Springer Nature Customer Service Centre GmbH: Springer Nature, Nature, [8] (Real-space observation of a two-dimensional skyrmion crystal, X. Z. Yu et al.), COPYRIGHT (2010))

as the methodology used, inspired much follow-up research, including lots of interesting work from their own group.

In 2013, researchers at the University of Hamburg reported the observation of skyrmions in the ultrathin film system by the method of spin-polarized scanning tunneling microscopy (**SP-STM**) [29]. The SP-STM technique can measure the magnetization distribution with atomic spatial resolution, which enables the study of the fine structure of skyrmions. In the ultrathin film system, the origin of the DMI is the interface structure, thus supporting the Néel-type skyrmion instead of the Bloch-type skyrmion that was observed in the B20 system. The spin spiral phase, skyrmion phase, and ferromagnetic phase are measured in real space, as shown in Fig. 1.7. Furthermore, they demonstrated that the skyrmions could be “write” and “delete” by using the magnetic tip of the **STM**.

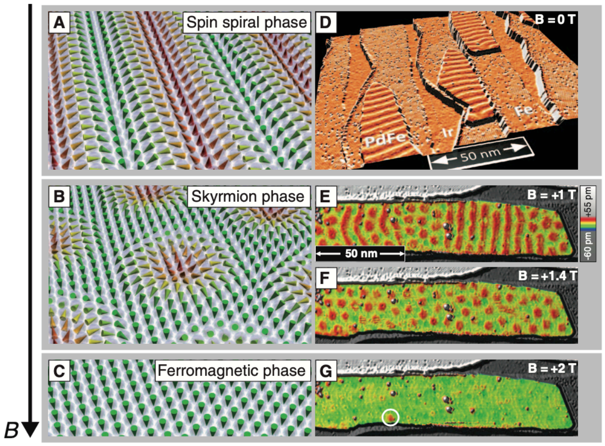

Figure 1.7: Skyrmion magnetic structures measured by SP-STM technique. (From [29]. Reprinted with permission from AAAS.)

These early experiments unambiguously demonstrated the existence of magnetic skyrmions of different types and their interesting phase change behavior. The underlying physical mechanisms and rich application potential resulted in great research interest and numerous follow-up works. In the next few sections, I will briefly introduce some of these most interesting works.

1.6.2 Bloch skyrmion in B20 structure system

Following up on their previous study, the research group of Prof. Tokura continued their research on skyrmions in B20 structure systems. In 2011, they showed that the Bloch skyrmion could be found in the B20 material

FeGe up to near room temperature [30]. They also studied the sample thickness-dependent of the skyrmion phase and found that as the thickness of the sample becomes larger, the skyrmion region shrinks dramatically in the temperature and field phase diagram, as shown in Fig. 1.8. In 2013, they showed that the size and chirality of the skyrmions could be tuned by changing the material composition by varying x in $Mn_{1-x}Fe_xGe$ [31]. In 2014, they observed a thermally-induced unidirectional rotation of the microscale skyrmion-crystal domains [32]. In 2015, they reported a study of the stability of the skyrmion phase along various crystal directions [33].

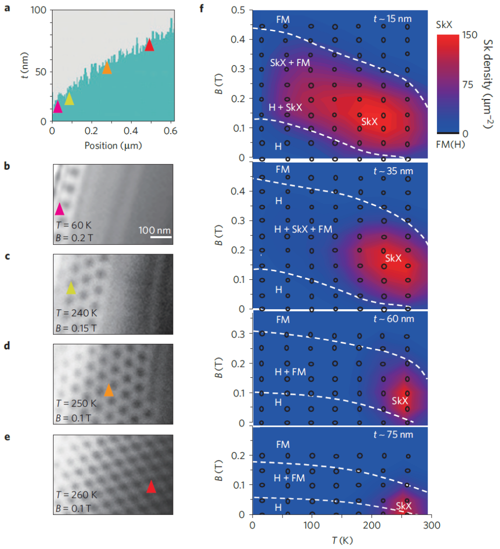

Figure 1.8: Thickness dependence of the skyrmion lattice phase in the temperature-field phase diagram in FeGe. (Reprinted by permission from Springer Nature Customer Service Centre GmbH: Springer Nature, Nature Materials [30] (Near room-temperature formation of a skyrmion crystal in thin-films of the helimagnet FeGe, X. Z. Yu et al.), COPYRIGHT (2010))

In 2012, Prof. Tokura's group showed that skyrmion could also be stabilized in a multiferroic material Cu_2OSeO_3 [34], as shown in Fig. 1.9. The discovery of the skyrmion in a multiferroic material could enable the possibility of manipulating a skyrmion by applying an external electric field.

The study and understanding of the B20 skyrmion went further in-depth. Theory predicted that, as the thickness of the sample becomes thicker, the Bloch skyrmion will have an increasing twist in the thickness direction, and when up to a critical thickness, the tube-like structure will break into "chiral bobber" [35, 36], as shown in Fig. 1.10.

In 2018, the chiral bobber was experimentally measured by the method of off-axis electron holography [37], as shown in Fig. 1.11.

Besides using real-space experimental measurements and bulk samples, the B20 type of Bloch skyrmion can also be detected by transport methods

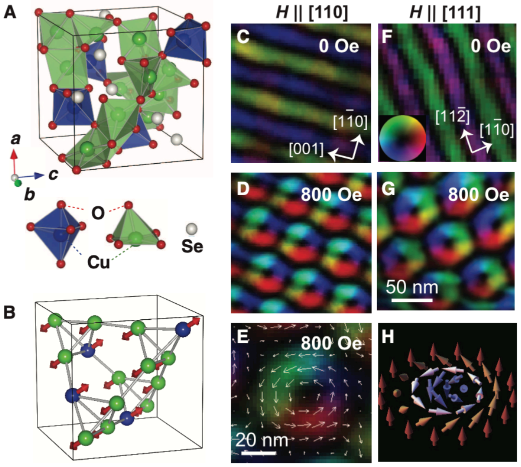
A
B
a
b
c
O
Cu
Se
H || [110]
H || [111]
C
0 Oe
[1$\bar{1}$0]
[001]
F
0 Oe
[11$\bar{2}$]
[1$\bar{1}$0]
D
800 Oe
G
800 Oe
50 nm
E
800 Oe
20 nm
H

Figure 1.9: The discovery of magnetic skyrmion in multiferroic material Cu_2OSeO_3. (From [34]. Reprinted with permission from AAAS.)

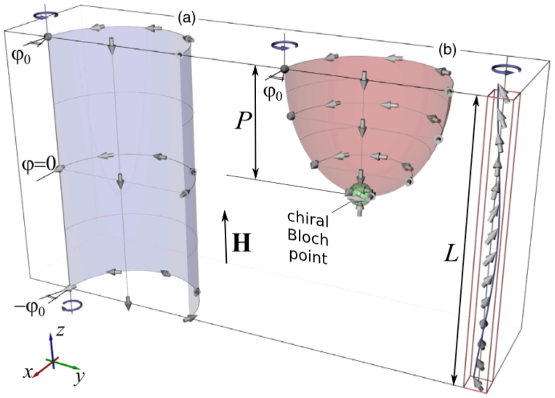
(a)
(b)
φ_0
φ=0
$-\varphi_0$
φ_0
P
H
chiral Bloch point
L
z
x
y

Figure 1.10: Schematic drawing of the magnetization and cross-section of the (a) skyrmion tube, and (b) chiral bobber. (Reprinted figure with permission from [35] Rybakov, F. N., Borisov, A. B., Blügel, S., & Kiselev, N. S., Physical review letters, 115, 117201 (2015)] Copyright (2015) by the American Physical Society.)

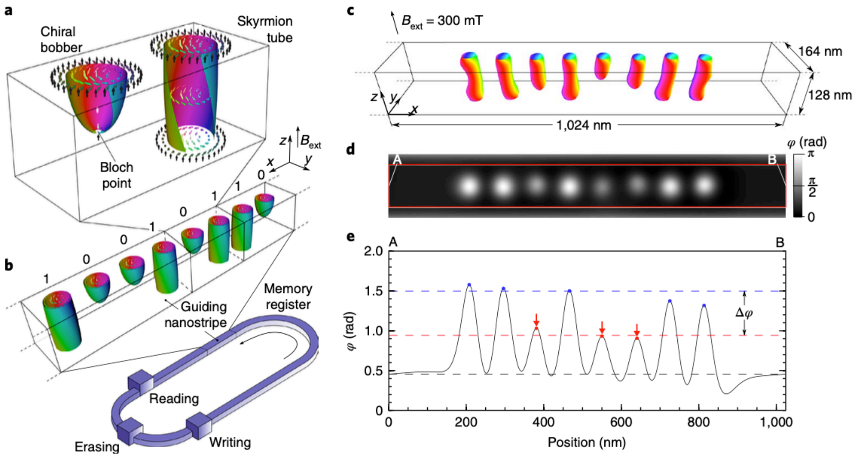
a
Chiral bobber
Skyrmion tube
Bloch point
z
B_{ext}
x
y
b
1
0
0
1
0
1
1
0
Guiding nanostripe
Memory register
Reading
Erasing
Writing
c
B_{ext} = 300 mT
164 nm
128 nm
1,024 nm
z
y
x
d
A
B
φ (rad)
π
π/2
0
e
A
B
2.0
1.5
1.0
0.5
0
φ (rad)
Δφ
0
200
400
600
800
1,000
Position (nm)

Figure 1.11: Experimental confirmation of the existence of chiral bobber. (Reprinted by permission from Springer Nature Customer Service Centre GmbH: Springer Nature, Nature Nanotechnology [37] (Experimental observation of chiral magnetic bobbers in B20-type FeGe, Fengshan Zheng et al.), COPYRIGHT (2018))

and using thin film deposition techniques [27]. In this work, by studying the temperature/field phase diagram and sample thickness dependence of the measured Hall resistance, a similar phase diagram behavior to that found in bulk single crystals was also found in thin film systems prepared by the magnetron sputtering technique.

1.6.3 Néel skyrmion in C_{nv} crystal structure system

Besides the B20 system, there are also other crystal symmetries that can have a DMI, and thus stabilize skyrmions. For example, in the crystal structure with C_{nv} (where n=3, 4, 6), the Néel type of skyrmion can be stabilized. In 2015, the material GaV_4S_8 with C_{3v} structure was found to host Néel skyrmions by the experimental method of magnetic force microscopy (**MFM**) and small-angle neutron scattering [10]. In 2017, the tetragonal polar magnet $VOSe_2O_5$ with the C_{4v} crystal structure was also discovered to stabilize Néel-type skyrmion lattices by the small-angle neutron scattering measurements [15].

In 2020, we observed robust Néel skyrmions stabilized in metallic PtMnGa crystals with C_{3v} structure [38]. We used LTEM and MFM measurement techniques, which will be briefly summarized in Chapter 3.

1.6.4 Skyrmion in interface system

In interfacial thin film systems, which are widely studied for current-induced domain wall motion, the DMI originates from interface symmetry breaking and results in Néel type domain wall structures. There, Néel type skyrmions can also be stabilized. For example, such skyrmions have been detected by the method of spin-polarized low-energy electron microscopy (**SPLEEM**) technique in the multilayer thin film system of Fe(2.5 ML)/Ni(2)/Cu(8.4)/Ni(15)/Cu(001) system [9]. The SPLEEM can measure all three components of the magnetization, thus confirming the skyrmions are of the Néel type, as shown in Fig. 1.12.

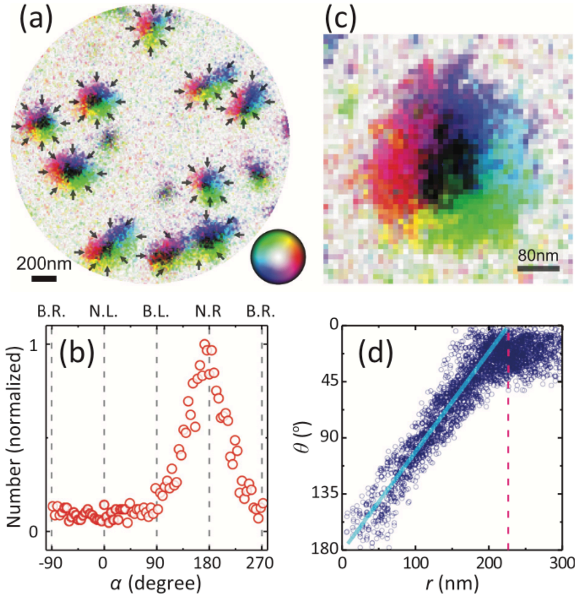

Figure 1.12: Experimental confirmation of the existence of interface DMI induced Néel skyrmion. (Reprinted from [9], with the permission of AIP Publishing.)

In 2015, by the method of Kerr-microscopy, "skyrmion bubbles" were observed using the magnetron sputtering grown thin-film structures with Ta(5 nm)/$Co_{20}Fe_{60}B_{20}$(1.1 nm)/TaO_x(3 nm) trilayer [26]. They showed that by applying current pulses under certain device geometries,that skyrmion bubbles can be created.

1.6.5 Other skyrmion systems

Besides the above introduced typical skyrmion systems, there are other types of skyrmions that have been identified, which will be briefly introduced below.

In 2013, the research group of Prof. Tokura reported the observation of magnetic biskyrmions [39]. The material is a bilayered manganese oxide $\mathrm{La}_{2\text{-}2x}\mathrm{Sr}_{1+2x}\mathrm{Mn}_2\mathrm{O}_7$ with $x = 0.35$ and its crystal structure is centrosymmetric. Due to the centrosymmetric space group, the system does not have DMI, which is needed to stabilize a skyrmion with a well defined chirality as introduced above. From the LTEM pattern, which shows two dots structure with black and white contrast, they deduce the magnetic structure to have two core structures, as shown in Fig. 1.13. In 2019, it was reported in the material of MnNiGa that the LTEM pattern of biskyrmions might rather correspond to type-II magnetic bubbles [40].

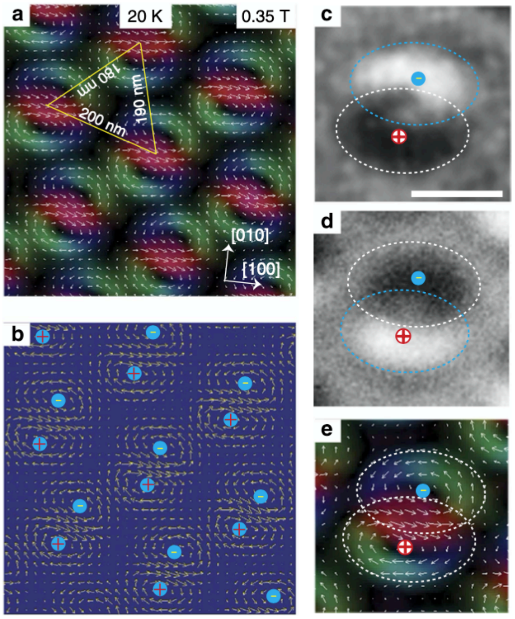

Figure 1.13: Magnetic structure of a biskyrmion and its corresponding LTEM pattern. (Reprinted by permission from Springer Nature Customer Service Centre GmbH: Springer Nature, Nature Communications, [39] (Biskyrmion states and their current-driven motion in a layered manganite, X. Z. Yu et al.), COPYRIGHT (2014))

In 2018, the research group of Prof. Tokura reported that in the B20 material structure, there might be a magnetically induced transformation of a square (anti)meron lattice to a hexagonal skyrmion lattice in the (001) plate of $\mathrm{Co}_8\mathrm{Zn}_9\mathrm{Mn}_3$ [41], as shown in Fig. 1.14.

Another kind of skyrmion is in a frustrated J1-J2-J3 ferromagnetic [42]. In this system, there is no DMI; however, the exchange interaction not only

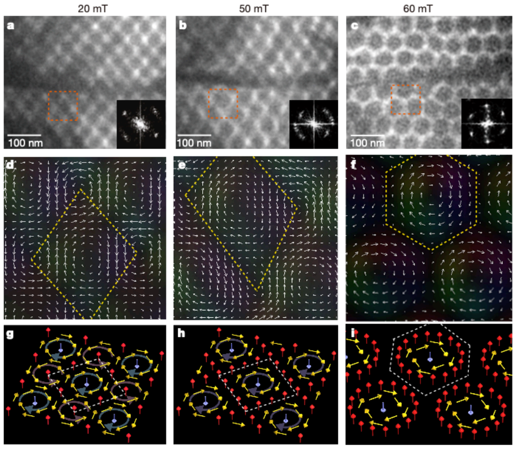

Figure 1.14: Magnetic structure of square (anti)meron lattice, hexagonal skyrmion lattice, and the transition state in between. (Reprinted by permission from Springer Nature Customer Service Centre GmbH: Springer Nature, Nature, [41] (Transformation between meron and skyrmion topological spin textures in a chiral magnet, X. Z. Yu et al.), COPYRIGHT (2018))

plays an essential role for the nearest-neighbor but also has a pronounced value for the next nearest-neighbor and next next nearest-neighbor. By the competition of these complex exchange interactions, various complex skyrmions with different topologies can be stabilized, as shown in Fig. 1.15.

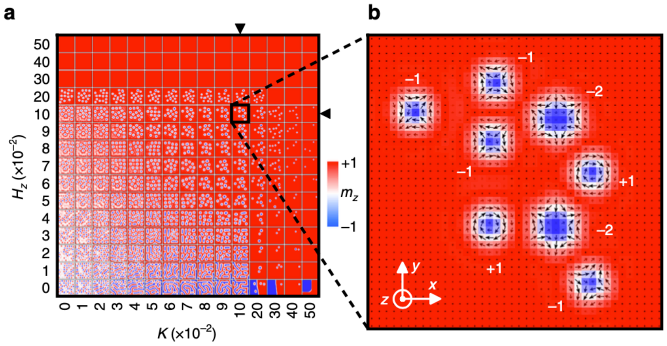

Figure 1.15: Magnetic structure of skyrmions in frustrated J1-J2-J3 ferromagnetic. (Reprinted from [42]. Link to the Creative Commons license: https://creativecommons.org/licenses/by/4.0/)

The family of skyrmions already has lots of members, and the number is still growing. The rich types of skyrmion enable the high potential of novel magnetic textures as well as non-trivial dynamical prosperities.

1.6.6 Current induced skyrmion motion

Besides research on the static properties of skyrmions, there are also lots of reports on their dynamical behavior, especially their current-induced motion. Due to the possibility of moving around defects, the critical current density of motion should be low. In B20 materials, the critical current density to trigger skyrmion motion can be as low as about $5\,\mathrm{A\,cm^{-2}}$ [43]. Current-induced skyrmion motion is also found in interface thin film systems [44], as shown in Fig. 1.16.

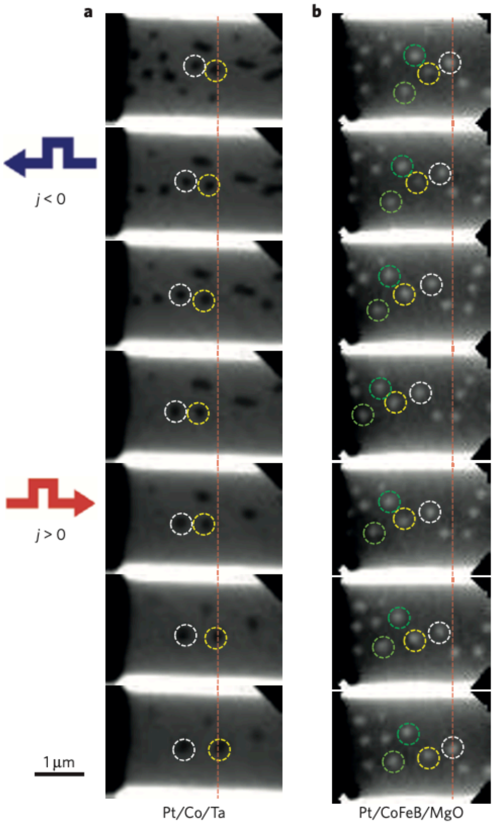

Figure 1.16: Current-induced skyrmion motion measured by magnetic transmission soft X-ray microscopy. (Reprinted by permission from Springer Nature Customer Service Centre GmbH: Springer Nature, Nature Materials [44] (Observation of room-temperature magnetic skyrmions and their current-driven dynamics in ultrathin metallic ferromagnets, Seonghoon Woo et al.), COPYRIGHT (2016))

Moreover, when the current induced skyrmion motion is triggered by spin currents generated from Spin Hall Effects in heavy metal layers, the skyrmion will move along a trajectory at an angle to the electrical current direction: this effects has been named the “skyrmion Hall effect”. The skyrmion Hall effect can be observed using Kerr microscopy mmeasurements [45] and scanning transmission X-ray microscopy (**STXM**) [46] technique. It has also recently been reported that, in the ferrimagnetic sample, the skyrmion Hall angle could be tuned and even vanish [47]. The above-mentioned current-induced motion in various skyrmions shows promising potential for next generation Racetrack memory applications [2].

1.7 Heusler material

Here, the concept of a Heusler Material, in which the antiskyrmion was discovered, will be briefly introduced. The Heusler material [48] is the name of a large family of materials with the general formula of X_2YZ where X and Y are transition metals and Z is a main group element (for half-heusler the formula is XYZ). The Heusler materials show exciting properties in topics such as spintronics, semiconductors, topological insulators, and even superconductivity. For magnetism, the interest of the Heusler compound started with Cu_2MnAl as a ferromagnetic material in which the elements involved are not ferromagnetic themselves. Recently, novel magnetic properties have been shown in several Heusler materials. For example, giant tunable exchange bias can be introduced [49] or large noncolllinearity and spin reorientation are found in novel Mn_2RhSn Heusler magnet [50]. This material has a crysta structure with a D_{2d} point group symmetry, and thus has the potential for hosting antiskyrmions.

Chapter 2

Skyrmion theory and micromagnetic simulation

In the first section of this chapter, I will introduce the basic theory of skyrmions. I will start with a symmetry analysis of the DMI exchange interaction energy term. Then, I will show how the DMI energy term determines the topology of possible non-collinear magnetic structures that the material can host. In a second section, I will first introduce the working principle of micromagnetic simulations, then, illustrate these principles with a few typical micromagnetic simulations. Finally, a self-coded program for batch calculation and analysis of the results will be presented.

2.1 Skyrmion theory

2.1.1 Exchange interaction between two atoms

The Dzyaloshinskii–Moriya interaction is named after Dzyaloshinskii and Moriya for their pioneering work [11, 12], which introduced a vector exchange interaction term in materials with a non-centrosymmetric crystal structure that allows for the alignment of neighboring magnetic moments perpendicular to each other rather than parallel/anti-parallel to each other as in conventional exchange interactions. To begin with, let us discuss the exchange interaction between two atoms.

For two arbitrary atoms: i and j, the most general exchange interaction

Hamiltonian H_{ij} can be written as:

$$H_{ij} = \overrightarrow{S_i} J_{ij} \overrightarrow{S_j} = \begin{pmatrix} S_{ix} & S_{iy} & S_{iz} \end{pmatrix} \begin{pmatrix} J_{ij,xx} & J_{ij,xy} & J_{ij,xz} \\ J_{ij,yx} & J_{ij,yy} & J_{ij,yz} \\ J_{ij,zx} & J_{ij,zy} & J_{ij,zz} \end{pmatrix} \begin{pmatrix} S_{jx} \\ S_{jy} \\ S_{jz} \end{pmatrix} \tag{2.1}$$

Here, $\overrightarrow{S_i}$ and $\overrightarrow{S_j}$ are the vectors of spin in 3-dimensional coordinates, so the most general form of exchange interaction J_{ij} is a 3 by 3 second-order tensor. This Hamiltonian can be decomposed into three parts as:

$$\begin{aligned} H_{ij} = &\begin{pmatrix} S_{ix} & S_{iy} & S_{iz} \end{pmatrix} \begin{pmatrix} J_{ij,xx} & 0 & 0 \\ 0 & J_{ij,yy} & 0 \\ 0 & 0 & J_{ij,zz} \end{pmatrix} \begin{pmatrix} S_{jx} \\ S_{jy} \\ S_{jz} \end{pmatrix} + \\ &\begin{pmatrix} S_{ix} & S_{iy} & S_{iz} \end{pmatrix} \begin{pmatrix} 0 & \frac{J_{ij,xy}-J_{ij,yx}}{2} & \frac{J_{ij,xz}-J_{ij,zx}}{2} \\ \frac{J_{ij,yx}-J_{ij,xy}}{2} & 0 & \frac{J_{ij,yz}-J_{ij,zy}}{2} \\ \frac{J_{ij,zx}-J_{ij,xz}}{2} & \frac{J_{ij,zy}-J_{ij,yz}}{2} & 0 \end{pmatrix} \begin{pmatrix} S_{jx} \\ S_{jy} \\ S_{jz} \end{pmatrix} + \\ &\begin{pmatrix} S_{ix} & S_{iy} & S_{iz} \end{pmatrix} \begin{pmatrix} 0 & \frac{J_{ij,xy}+J_{ij,yx}}{2} & \frac{J_{ij,xz}+J_{ij,zx}}{2} \\ \frac{J_{ij,yx}+J_{ij,xy}}{2} & 0 & \frac{J_{ij,yz}+J_{ij,zy}}{2} \\ \frac{J_{ij,zx}+J_{ij,xz}}{2} & \frac{J_{ij,zy}+J_{ij,yz}}{2} & 0 \end{pmatrix} \begin{pmatrix} S_{jx} \\ S_{jy} \\ S_{jz} \end{pmatrix} \end{aligned} \tag{2.2}$$

The first term corresponds to a simple exchange. Under the usual assumption that the exchange interaction is isotropic, $J_{ij,xx} = J_{ij,yy} = J_{ij,zz} = J_{ij,Hei}$, this term corresponds to the Heisenberg exchange model:

$$\begin{aligned} H_{ij,sim\_Exc} = &\begin{pmatrix} S_{ix} & S_{iy} & S_{iz} \end{pmatrix} \begin{pmatrix} J_{ij,Hei} & 0 & 0 \\ 0 & J_{ij,Hei} & 0 \\ 0 & 0 & J_{ij,Hei} \end{pmatrix} \begin{pmatrix} S_{jx} \\ S_{jy} \\ S_{jz} \end{pmatrix} \\ = &J_{ij,Hei} \overrightarrow{S_i} \cdot \overrightarrow{S_j} \end{aligned} \tag{2.3}$$

Let us define, $D_{ij,z} = \frac{J_{ij,xy}-J_{ij,yx}}{2}$, $D_{ij,y} = -\frac{J_{ij,xz}-J_{ij,zx}}{2}$,$D_{ij,x} = \frac{J_{ij,yz}-J_{ij,zy}}{2}$, so the second term becomes:

$$\begin{aligned} H_{ij,DMI} = &\begin{pmatrix} S_{ix} & S_{iy} & S_{iz} \end{pmatrix} \begin{pmatrix} 0 & D_{ij,z} & -D_{ij,y} \\ -D_{ij,z} & 0 & D_{ij,x} \\ D_{ij,y} & -D_{ij,x} & 0 \end{pmatrix} \begin{pmatrix} S_{jx} \\ S_{jy} \\ S_{jz} \end{pmatrix} \\ = &\overrightarrow{D_{ij}} \cdot \overrightarrow{S_i} \times \overrightarrow{S_j} \end{aligned} \tag{2.4}$$

where$\overrightarrow{D_{ij}} = \begin{pmatrix} D_{ij,x} & D_{ij,y} & D_{ij,z} \end{pmatrix}$ is the DMI vector.

The third term is a traceless symmetric part, which corresponds to energy terms such as anisotropy [51]. The relative magnitude of the second and third term to the first term is on the order of $\frac{\Delta g}{g}$ and $(\frac{\Delta g}{g})^2$, where g is the gyromagnetic ratio, and Δg is its deviation from the value for a free electron [12]. Their amplitudes are relatively small and thus can usually be neglected, especially for the case of the third term.

Thus the Heisenberg and DMI exchange energy terms correspond to the diagonal part and antisymmetric non-diagonal part of the general exchange tensor. Based on this mathematical formalism, by applying the crystal symmetry, we can find the corresponding Hamiltonian for various crystal symmetry systems.

2.1.2 Exchange interaction under different crystal symmetries

Let us now consider the situation of the exchange interaction in a space group. Due to the symmetry property of the space group, the exchange interaction between atoms in the group is no longer completely independent. These interactions are connected via relationships that depended on the detailed crystal symmetry properties.

For the most general situation, let us consider two arbitrary atoms in the space group $i, 1$ and $j, 1$. The coordinate of $i, 1$ and $j, 1$ are:

$$\begin{aligned}
&\overrightarrow{r_{i,1}} = \begin{pmatrix} x_{i,1} & y_{i,1} & z_{i,1} \end{pmatrix} \\
&\overrightarrow{r_{j,1}} = \begin{pmatrix} x_{j,1} & y_{j,1} & z_{j,1} \end{pmatrix} \\
&\overrightarrow{r_{ij,1}} = \overrightarrow{r_{j,1}} - \overrightarrow{r_{i,1}} = \begin{pmatrix} x_{j,1} - x_{i,1} & y_{j,1} - y_{i,1} & z_{j,1} - z_{i,1} \end{pmatrix} = \begin{pmatrix} \Delta x & \Delta y & \Delta z \end{pmatrix}
\end{aligned} \tag{2.5}$$

In this space group, there are N_{sym} general positions, which is also the number of symmetry operations. So, atom $i, 1$ and $j, 1$ and their interactions correspond to other N_{sym} atoms and interactions, as folllows:

$$\begin{aligned}
\overrightarrow{r_{i,\alpha}} &= \begin{pmatrix} x_{i,\alpha} & y_{i,\alpha} & z_{i,\alpha} \end{pmatrix} = R_\alpha \overrightarrow{r_{i,1}} \\
\overrightarrow{r_{j,\alpha}} &= \begin{pmatrix} x_{j,\alpha} & y_{j,\alpha} & z_{j,\alpha} \end{pmatrix} = R_\alpha \overrightarrow{r_{j,1}} \\
\overrightarrow{r_{ij,\alpha}} &= \overrightarrow{r_{j,\alpha}} - \overrightarrow{r_{i,\alpha}} = R_\alpha \begin{pmatrix} \Delta x & \Delta y & \Delta z \end{pmatrix} = R_\alpha \overrightarrow{r_{ij,1}}
\end{aligned} \tag{2.6}$$

where R_α is the symmetry operation and $\alpha = 1 \dots N_{sym}$.

Then the total exchange energy for the system is:

$$H_{ij} = \sum_{\alpha=1}^{N_{sym}} \begin{pmatrix} S_{ix,\alpha} & S_{iy,\alpha} & S_{iz,\alpha} \end{pmatrix} \begin{pmatrix} J_{ij,xx,\alpha} & J_{ij,xy,\alpha} & J_{ij,xz,\alpha} \\ J_{ij,yx,\alpha} & J_{ij,yy,\alpha} & J_{ij,yz,\alpha} \\ J_{ij,zx,\alpha} & J_{ij,zy,\alpha} & J_{ij,zz,\alpha} \end{pmatrix} \begin{pmatrix} S_{jx,\alpha} \\ S_{jy,\alpha} \\ S_{jz,\alpha} \end{pmatrix} \tag{2.7}$$

After R_β, the original atom and associated spin component will correspond to the new atom and spin component. Note that since the magnetization is a pseudovector, an extra determinant of the symmetry matrix needs to be multiplied.

$$\begin{aligned} \overrightarrow{r_{i,\alpha}} &\rightarrow R_\beta \overrightarrow{r_{i,\alpha}} \\ \overrightarrow{r_{j,\alpha}} &\rightarrow R_\beta \overrightarrow{r_{j,\alpha}} \\ \begin{pmatrix} S_x & S_y & S_z \end{pmatrix} &\rightarrow det(R_\beta) R_\beta \begin{pmatrix} S_x & S_y & S_z \end{pmatrix} \end{aligned} \tag{2.8}$$

In the total exchange energy, replacing the spin component of a certain atom by the one which after R_β will be moved to, we will get the new exchange energy term. After the symmetry operation, the energy of the system should not be changed.

$$R_\beta H_{ij} = H_{ij} \tag{2.9}$$

We then find the relationship between different exchange tensors.

For example, for the space group No. 111 (D_{2d}^1), if we define

$$\begin{gathered} \begin{pmatrix} J_{ij,xx,1} & J_{ij,xy,1} & J_{ij,xz,1} \\ J_{ij,yx,1} & J_{ij,yy,1} & J_{ij,yz,1} \\ J_{ij,zx,1} & J_{ij,zy,1} & J_{ij,zz,1} \end{pmatrix} = \begin{pmatrix} J_{ij,xx} & J_{ij,xy} & J_{ij,xz} \\ J_{ij,yx} & J_{ij,yy} & J_{ij,yz} \\ J_{ij,zx} & J_{ij,zy} & J_{ij,zz} \end{pmatrix} \\ D_z = \frac{J_{xy} - J_{yx}}{2}, D_y = -\frac{J_{xz} - J_{zx}}{2}, D_x = \frac{J_{yz} - J_{zy}}{2} \end{gathered} \tag{2.10}$$

then we can get for all the 8 general positions:

$$\begin{aligned}
&\overrightarrow{r_{ij,1}} = \begin{pmatrix} \Delta x & \Delta y & \Delta z \end{pmatrix}, && \overrightarrow{A_{ij,1}} = \begin{pmatrix} J_{xx} & J_{yy} & J_{zz} \end{pmatrix}, \overrightarrow{D_{ij,1}} = \begin{pmatrix} D_x & D_y & D_z \end{pmatrix} \\
&\overrightarrow{r_{ij,2}} = \begin{pmatrix} -\Delta x - \Delta y & \Delta z \end{pmatrix}, && \overrightarrow{A_{ij,2}} = \begin{pmatrix} J_{xx} & J_{yy} & J_{zz} \end{pmatrix}, \overrightarrow{D_{ij,2}} = \begin{pmatrix} -D_x & -D_y & D_z \end{pmatrix} \\
&\overrightarrow{r_{ij,3}} = \begin{pmatrix} \Delta y & -\Delta x & -\Delta z \end{pmatrix}, && \overrightarrow{A_{ij,3}} = \begin{pmatrix} J_{yy} & J_{xx} & J_{zz} \end{pmatrix}, \overrightarrow{D_{ij,3}} = \begin{pmatrix} -D_y & D_x & D_z \end{pmatrix} \\
&\overrightarrow{r_{ij,4}} = \begin{pmatrix} -\Delta y & \Delta x & -\Delta z \end{pmatrix}, && \overrightarrow{A_{ij,4}} = \begin{pmatrix} J_{yy} & J_{xx} & J_{zz} \end{pmatrix}, \overrightarrow{D_{ij,4}} = \begin{pmatrix} D_y & -D_x & D_z \end{pmatrix} \\
&\overrightarrow{r_{ij,5}} = \begin{pmatrix} -\Delta x & \Delta y & -\Delta z \end{pmatrix}, && \overrightarrow{A_{ij,5}} = \begin{pmatrix} J_{zz} & J_{xx} & J_{yy} \end{pmatrix}, \overrightarrow{D_{ij,5}} = \begin{pmatrix} -D_x & D_y & -D_z \end{pmatrix} \\
&\overrightarrow{r_{ij,6}} = \begin{pmatrix} \Delta x & -\Delta y & -\Delta z \end{pmatrix}, && \overrightarrow{A_{ij,6}} = \begin{pmatrix} J_{zz} & J_{xx} & J_{yy} \end{pmatrix}, \overrightarrow{D_{ij,6}} = \begin{pmatrix} D_x & -D_y & -D_z \end{pmatrix} \\
&\overrightarrow{r_{ij,7}} = \begin{pmatrix} -\Delta y & -\Delta x & \Delta z \end{pmatrix}, && \overrightarrow{A_{ij,7}} = \begin{pmatrix} J_{yy} & J_{xx} & J_{zz} \end{pmatrix}, \overrightarrow{D_{ij,7}} = \begin{pmatrix} D_y & D_x & -D_z \end{pmatrix} \\
&\overrightarrow{r_{ij,8}} = \begin{pmatrix} \Delta y & \Delta x & \Delta z \end{pmatrix}, && \overrightarrow{A_{ij,8}} = \begin{pmatrix} J_{yy} & J_{xx} & J_{zz} \end{pmatrix}, \overrightarrow{D_{ij,8}} = \begin{pmatrix} -D_y & -D_x & -D_z \end{pmatrix}
\end{aligned} \tag{2.11}$$

From here, we can find, under the symmetry of this space group, the relation of the exchange interaction between every pair of atoms.

Now, we make the assumptions that the magnetization changes continuously, and that atoms i and j are close enough to each other. These assumptions are usually satisfied nicely since the size of the skyrmion is usually much larger compared to the lattice constant, and the exchange interaction only is signiificant for nearby atoms. So, the magnetization on atom j can be expanded to the first order as:

$$\begin{aligned} S_{jx} &= S_{ix} + \frac{\partial M_x}{\partial x}\Delta x + \frac{\partial M_x}{\partial y}\Delta y + \frac{\partial M_x}{\partial z}\Delta z \\ S_{jy} &= S_{iy} + \frac{\partial M_y}{\partial x}\Delta x + \frac{\partial M_y}{\partial y}\Delta y + \frac{\partial M_y}{\partial z}\Delta z \\ S_{jz} &= S_{iz} + \frac{\partial M_z}{\partial x}\Delta x + \frac{\partial M_z}{\partial y}\Delta y + \frac{\partial M_z}{\partial z}\Delta z \end{aligned} \tag{2.12}$$

So, for simple exchange, assuming

$$\begin{aligned} A_1 &= -2J_{xx}(\Delta x)^2 - 2J_{yy}(\Delta y)^2 \\ A_2 &= -2J_{yy}(\Delta x)^2 - 2J_{xx}(\Delta y)^2 \\ A_3 &= -2J_{xx}(\Delta z)^2 - 2J_{yy}(\Delta z)^2 \\ A_4 &= -2J_{zz}(\Delta x)^2 - 2J_{zz}(\Delta y)^2 \\ A_5 &= -4J_{zz}(\Delta z)^2 \\ D &= 4D_x\Delta x - 4D_y\Delta y \end{aligned} \tag{2.13}$$

we can get

$$\begin{aligned} H_{sim\_Exc} = {} & A_1\left(\frac{\partial M_x}{\partial x}\right)^2 + A_2\left(\frac{\partial M_x}{\partial y}\right)^2 + A_3\left(\frac{\partial M_x}{\partial z}\right)^2 + A_2\left(\frac{\partial M_y}{\partial x}\right)^2 + A_1\left(\frac{\partial M_y}{\partial y}\right)^2 \\ & + A_3\left(\frac{\partial M_y}{\partial z}\right)^2 + A_4\left(\frac{\partial M_z}{\partial x}\right)^2 + A_4\left(\frac{\partial M_z}{\partial y}\right)^2 + A_5\left(\frac{\partial M_z}{\partial z}\right)^2 \\ H_{DMI} = {} & D\left(M_y\frac{\partial M_z}{\partial x} - M_z\frac{\partial M_y}{\partial x}\right) - D\left(M_z\frac{\partial M_x}{\partial y} - M_x\frac{\partial M_z}{\partial y}\right) \end{aligned} \tag{2.14}$$

Using this method, we can find the DMI energy terms foro ther crystal symmetries. For example, in space group No. 195 (T^1), let $D = 4D_x\Delta x + 4D_y\Delta y + 4D_z\Delta z$, then

$$H_{DMI} = D\left(M_y\frac{\partial M_z}{\partial x} - M_z\frac{\partial M_y}{\partial x}\right) + D\left(M_z\frac{\partial M_x}{\partial y} - M_x\frac{\partial M_z}{\partial y}\right) + D\left(M_x\frac{\partial M_y}{\partial z} - M_y\frac{\partial M_x}{\partial z}\right) \tag{2.15}$$

In the space group No. 75 (C_4^1), let $D_1 = 2D_x\Delta x + 2D_y\Delta y$, $D_2 = 2D_x\Delta y - 2D_y\Delta x$ and $D_z = 4D_z\Delta z$, then

$$\begin{aligned} H_{DMI} = {} & D_1\left(M_y\frac{\partial M_z}{\partial x} - M_z\frac{\partial M_y}{\partial x}\right) + D_2\left(M_y\frac{\partial M_z}{\partial y} - M_z\frac{\partial M_y}{\partial y}\right) - D_2\left(M_z\frac{\partial M_x}{\partial x} - M_x\frac{\partial M_z}{\partial x}\right) \\ & + D_1\left(M_z\frac{\partial M_x}{\partial y} - M_x\frac{\partial M_z}{\partial y}\right) + D_3\left(M_x\frac{\partial M_y}{\partial z} - M_y\frac{\partial M_x}{\partial z}\right) \end{aligned} \tag{2.16}$$

The DMI energy term for all crystal structures is summarized in Appendix A. These results agree with the previous literature [52, 53].

2.1.3 Magnetic topology of skyrmion under different crystal symmetry

After obtaining the major Hamiltonian term, we can now derive the magnetic topology of skyrmions for different crystal symmetries. We consider the situation in a 2-dimensional situation here. A polar coordinate

$$\begin{cases} x = \rho\cos\eta \\ y = \rho\sin\eta \end{cases} \tag{2.17}$$

is used, whose origin is at the center of the skyrmion, and the magnetization is defined as

$$\begin{cases} M_x = M_s\sin\theta\cos\varphi \\ M_y = M_s\sin\theta\sin\varphi \\ M_z = M_s\cos\theta \end{cases} \tag{2.18}$$

as shown in the Fig. 2.1.

For the single skyrmion which has a round shape, we can assume that:

$$\begin{cases} \theta = \theta(\rho) \\ \varphi = \varphi(\eta) \end{cases} \qquad \text{and} \qquad \begin{cases} \dfrac{\partial\theta}{\partial\eta} = 0 \\ \dfrac{\partial\varphi}{\partial\rho} = 0 \end{cases} \tag{2.19}$$

Let us first derive the situation corresponding to the B20 crystal structure. Considering the energy terms of exchange, DMI, and Zeeman energy, the

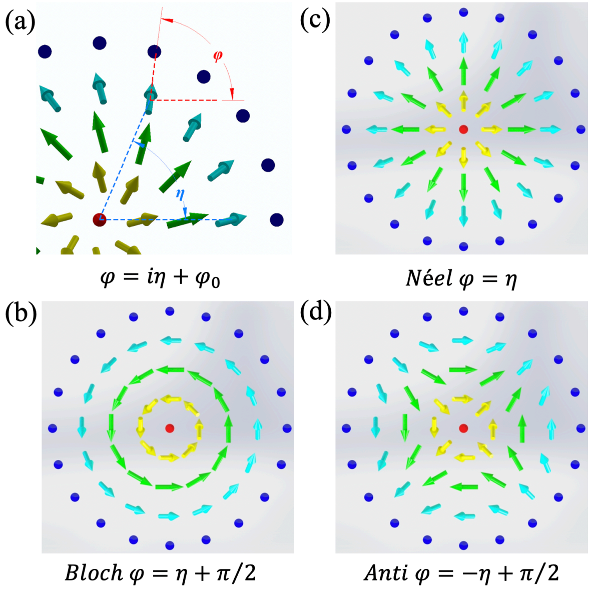

Figure 2.1: Coordinate definition and typical magnetic topology of skyrmion. (a) Coordinate definition, (b-d) magnetic topology of Bloch, Néel and antiskyrmion.

total energy is:

$$
\begin{aligned}
H_{total} &= H_{sim\_Exc} + H_{DMI} + H_{Zeeman} \\
&= AM_s^2\left(\frac{\partial\theta}{\partial\rho}\right)^2 + AM_s^2\sin^2\theta\left(\frac{1}{\rho}\frac{\partial\varphi}{\partial\eta}\right)^2 \\
&+ DM_s^2\sin(\eta-\varphi)\left(\frac{\partial\theta}{\partial\rho} + \cos\theta\sin\theta\frac{1}{\rho}\frac{\partial\varphi}{\partial\eta}\right) - HM_s\cos\theta
\end{aligned}
\tag{2.20}
$$

Thus, in order to minimize the total energy, when $D > 0$ and

$$
\theta = \begin{cases} 0, & \rho = 0 \\ \pi, & \rho = +\infty \end{cases}
\tag{2.21}
$$

we obtain the magnetic topology below, as shown in Fig. 2.1b.

$$
\varphi = \eta + \frac{\pi}{2}
\tag{2.22}
$$

Using the same method, and using the DMI energy term for other crystal structures, the typical magnetic topology of a Néel skyrmion in C_{3v} material and an antiskyrmion in D_{2d} material are shown in Fig. 2.1c-d.

In order to solve the skyrmion magnetization geometry, we need to solve the Euler equations by using functional derivatives [6]:

$$\frac{\delta H_{total}}{\delta\theta} = \frac{\delta H_{total}}{\delta\varphi} = 0 \tag{2.23}$$

Thus,

$$\begin{aligned}
&\frac{\partial H_{total}}{\partial\theta} - \frac{1}{\rho}\frac{\partial}{\partial\rho}\left[\rho\frac{\partial H_{total}}{\partial\left(\frac{\partial\theta}{\partial\rho}\right)}\right] = 0\\
&\frac{\partial H_{total}}{\partial\varphi} - \frac{1}{\rho}\frac{\partial}{\partial\eta}\left[\frac{\partial H_{total}}{\partial\left(\frac{1}{\rho}\frac{\partial\varphi}{\partial\eta}\right)}\right] = 0
\end{aligned} \tag{2.24}$$

Solving the above equations, we have

$$\begin{aligned}
&D\cos(\eta-\varphi)\left(\frac{\partial\theta}{\partial\rho} + \frac{1}{\rho}\cos\theta\sin\theta\right) + \frac{1}{\rho^2}2A\sin^2\theta\frac{\partial^2\varphi}{\partial\eta^2} = 0\\
&A\sin 2\theta\left(\frac{1}{\rho}\frac{\partial\varphi}{\partial\eta}\right)^2 + D\sin(\eta-\varphi)\cos 2\theta\frac{1}{\rho}\frac{\partial\varphi}{\partial\eta} + \frac{H}{M_s}\sin\theta - \frac{1}{\rho}2A\frac{\partial\theta}{\partial\rho} - 2A\frac{\partial^2\theta}{\partial\rho^2}\\
&\quad - \frac{1}{\rho}D\sin(\eta-\varphi) = 0
\end{aligned} \tag{2.25}$$

Solving Equ.(2.25) will provide us the magnetic structure. The solution is usually complicated and does not have a closed-form expression so nicromagnetic simulations are very useful to find a numerical solution, as will be discussed in the next section.

The skyrmion structure in 3-dimensions becomes yet more complicated. For example, in a B20 material, due to the DMI having components in all 3-dimensions, an additional twist will be induced in a skyrmion tube structure [35]. As the thickness is increased, the parameter range for a skyrmion to be stabilized will thus shrink [30] or the skyrmion can even break up into chiral bobbers. In other materials, e.g., D_{2d} antiskyrmions, the zero value of the component of the DMI vector along the 3rd dimension leads to an intrinsic stability, which will be discussed in detail in Chapter 5. Other energy terms, such as the long-range magnetic dipolar interaction, will also induce additional magnetization structures such as vertical Bloch lines [6] or “Néel Cap” [54]. These complicated 3D structures can hardly be described analytically so that they have largely been studied via micromagnetic simulations.

2.2 Micromagnetic simulation

As discussed in the section above, analytical solutions to the magnetic structure or magnetization dynamics is complicated, if not impossible, to obtain for lots of magnetic structures. So, numerical solutions play a crucial role in spintronics research. Depending on the material parameters, the characteristic size of the magnetic structure can have a wide range from nanometers to even centimeters. Thus, the numerical calculation of the magnetic structure on the atomic scale in most of the situations is not necessary. Under the assumption that the magnetization varies smoothly, the problem can be turned into solving the Landau–Lifshitz–Gilbert (LLG) equation by using finite element methods.

2.2.1 Working principle of micromagnetic simulations

In micromagnetic simulations, the goal is to fnd the magnetization as a function of space and time, $\overrightarrow{M}(x, y, z, t)$. Typically, the calculation area is separated into cuboid shaped unit cells $\Delta V = \Delta x \Delta y \Delta z$, where Δx,Δy and Δz, are the step size in the XYZ coordinate directions. Within the unit cell, the magnetization is considered to be aligned along one direction. The cell size needs to be chosen so that it is small enough compared with the characteristic size of the magnetic structure. The equation to be solved is the LLG equation [55]:

$$\begin{aligned}\frac{\mathrm{d}\overrightarrow{M}}{\mathrm{d}t} = -\frac{\gamma}{1+\alpha^2}\overrightarrow{M} \times \overrightarrow{H_{eff}} - \frac{\gamma\alpha}{(1+\alpha^2)M_s}\overrightarrow{M} \times \left(\overrightarrow{M} \times \overrightarrow{H_{eff}}\right) \\ -\gamma\overrightarrow{M} \times \vec{\sigma}\sqrt{\frac{2k_B T\alpha}{\gamma(1+\alpha^2)M_s \Delta V \Delta t}} + \tau_{Spin\_Torque}\end{aligned} \tag{2.26}$$

where, α is the damping factor, γ is the gyromagnetic ratio, $\overrightarrow{H_{eff}}$ is the effective field, M_s is the saturation magnetization and the third and fourth terms on the right hand side of the equation correspond to a temperature term and a spin torque related term, respectively. Once initial conditions and boundary conditions are set, the calculation can be performed. The effective field and spin torque terms need to be adopted to the finite element formalism, as follows.

For example, the Heisenberg exchange interaction on the atomic scale is:

$$H_{Hei} = -\sum_{<i,j>} J\overrightarrow{s_i} \cdot \overrightarrow{s_j} \tag{2.27}$$

where J is the exchange interaction constant and $< i, j >$ denotes the sum over nearest neighbors.

In a continuum formalism, the exchange interaction can be written as:

$$H_{Hei} = A \iiint_V \left[(\nabla m_x)^2 + (\nabla m_y)^2 + (\nabla m_z)^2\right] \mathrm{d}x \, \mathrm{d}y \, \mathrm{d}z \tag{2.28}$$

where A is the exchange stiffness in $\mathrm{J\,m^{-1}}$.

Finally, in the finite element method,

$$H_{Hei} = \sum_{j \in N_i} A_{ij} \frac{\overrightarrow{m_i} \cdot (\overrightarrow{m_i} - \overrightarrow{m_j})}{\Delta_{ij}^2} \tag{2.29}$$

where Δ_{ij} is the step size between cell i and j.

Thus, an effective field corresponding to the exchange interaction can be obtained. Similar methods can be used for the other energy terms, such as the DMI energy and the magnetic anisotropy energy.

Another example is for the spin Hall effect induced torque, for which the the torque term is given by:

$$-\gamma\overrightarrow{M} \times \overrightarrow{M} \times \overrightarrow{H_{SHE}} - \alpha\gamma n_{a,SHE}\overrightarrow{M} \times \overrightarrow{H_{SHE}} \tag{2.30}$$

which corresponding to the field-like and damping-like parts of the torque, where $n_{a,SHE}$ is the parameter that determines the ratio between these two parts.

The effective field corresponding to the Spin-Hall-effect is:

$$\overrightarrow{H_{SHE}} = \frac{\hbar\theta_{SHE}}{2|e|M_s\Delta}(-\overrightarrow{n} \times \overrightarrow{J}) \tag{2.31}$$

where $\overrightarrow{J}$ is the current injected, $|e|$ is the electronic charge magnitude, $\hbar$ is the Planck constant, θ_{SHE} is the spin Hall angle of the material, Δ is the thickness of the adjacent layer in which the current flows and $\overrightarrow{n}$ is the normal direction of the interface.

The long range magnetic dipolar interaction is much more complicated to include. Due to its long range interaction, the interaction between cells even far away from each other needs to be calculated, which is by contrast with the exchange interaction where only nearest beighbor cells need to be considered. The demagnetizing tensor [56] and Fast-Fourier-Transformation(**FFT**) methods [57] have been developed to take care of the long range interaction, and this part of the energy calculation can be accelerated by using specialized hardware, in particular, **GPU**s [58].

2.2.2 Popular micromagnetic simulation software

Although researchers can develop their own software to perform micromagnetic simulations this is very time-consuming especially to eliminate ”bugs” so in the spintronics community, it is now very common to use well-established, often open-source, micromagnetic simulation software programs. On the one hand, such software is more user friendly, e.g., including graphical user interfaces and tutorial documents; on the other hand, these software are usually much more optimized, bug-free, and convenient for researchers to reproduce results from each other. Here, I just briefly introduced the three most popular micromagnetic simulation software.

OOMMF [59], short for object-oriented micromagnetic framework, is a calculation platform developed by scientists at the National Institute of Standards and Technology, USA. It is the most used micromagnetic simulation software. It takes advantage of the user interface of Tcl/Tk so that each step of the calculation can be visualized. A big advantage of OOMMF is that the software can be secondary developed and has a wide range of user communities. Contributions of new functions made by scientists from all over the world makes OOMMF ever more powerful. Some of the earliest simulations in skyrmion studies were performed by OOMMF [14].

Mumax3 [58] is another popular micromagnetic simulation software program. It is developed by the group of Prof. Van Waeyenberge at Ghent University. Comparing to OOMMF, Mumax3 takes advantage of GPUs so that an acceleration of ~100 times might be achieved compared with using **CPU**. Mumax also has an active community so that new features can be added and shared by researchers. Another big advantage of the Mumax3 and OOMMF programs is that they are free to use.

LLG Simulator [55] is a commercial software programed by Michael R. Scheinfein. It is one of the earliest simulation programs that included novel physical concepts such as DMI, SHE injection, Rashba effect. It is also among the earliest software that uses GPUs to accelerate the calculation speed.

In this software, it separates the long-range dipolar magnetic interaction to be calculated in GPU, and other calculations to be performed in CPU, thus significantly increasing the calculation speed. Working together with Michael R. Scheinfein, the general form of DMI was implemented into the LLG simulator program in order to simulate antiskyrmions stabilized by the D_{2d} type of DMI.

2.2.3 Batch calculation and result analysis

Batch calculations are essential to carry out systematic research, such as varying parameters and for the calculation of phase diagrams. On the one hand, it can save time and effort to manually input the parameters and avoid typos; On the other hand, disabling the **GUI** during batch calculation can avoid wasting the calculation resource in displaying real-time results. In order to perform batch calculations, a program is coded to generate the parameter specific files (such as *.mif in OOMMF). Then the program sends the files one by one to the micromagnetic software and only the magnetization information needs to be analyzed.

For example, in order to calculate the field-dependent phase diagram of the ground state of the magnetization structure, the following steps are usually performed:

1. Start the calculation from a random state at a high temperature.
2. Perform the calculation for some time (e.g. 100 ns) at each temperature. The temperature is gradually decreased. The output magnetization structure is used as input for the next calculation.
3. Finally perform the calculation at zero temperature until the stabilized magnetization structure is found.
4. Repeat step 1-3 for different field amplitudes

Chapter 5 will discuss in detail a phase diagram calculation. Due to the extensive calculation load, it took around half a month to calculate the phase diagram. Such a type of systematic calculation can hardly be done manually.

The calculation results also need to be analyzed by software. Fig. 2.2 shows a self-programed program to analyze the current induced domain wall (DW) motion. The DW position, motion speed, and tilting angle etc. can be analyzed automatically. Using the software to analyze the batch calculation results can vastly increase the research efficiency.

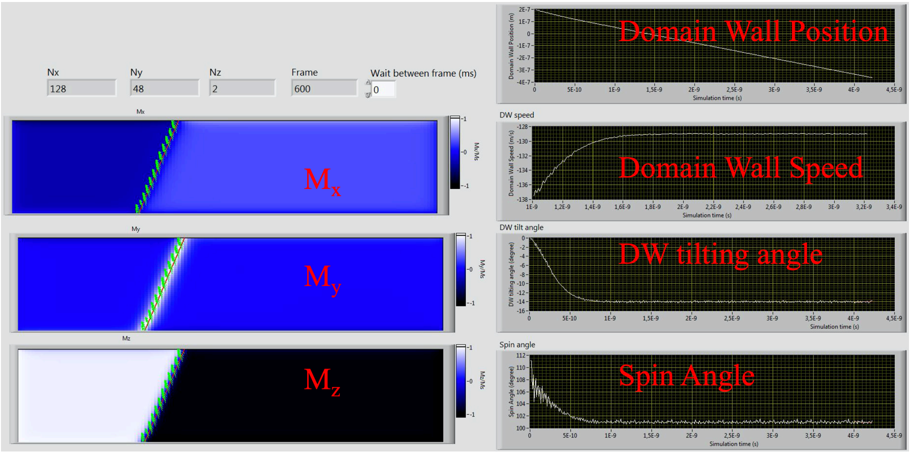

Nx: 128
Ny: 48
Nz: 2
Frame: 600
Wait between frame (ms): 0

Mx
Mx/Ms
1
0
-1
My
My/Ms
Mz
Mz/Ms
M_x
M_y
M_z
Domain Wall Position
Domain Wall Position (m)
2E-7
1E-7
0
-1E-7
-2E-7
-3E-7
-4E-7
Simulation time (s)
0
5E-10
1E-9
1,5E-9
2E-9
2,5E-9
3E-9
3,5E-9
4E-9
4,5E-9
DW speed
Domain Wall Speed
Domain Wall Speed (m/s)
-128
-130
-132
-134
-136
-138
1E-9
1,2E-9
1,4E-9
1,6E-9
1,8E-9
2E-9
2,2E-9
2,4E-9
2,6E-9
2,8E-9
3E-9
3,2E-9
3,4E-9
DW tilt angle
DW tilting angle
DW tilting angle (degree)
0
-2
-4
-6
-8
-10
-12
-14
-16
Spin angle
Spin Angle
Spin Angle (degree)
112
110
108
106
104
102
100

Figure 2.2: Self-programmed software for Current-Induced Domain Wall Motion analysis.

Chapter 3

Experimental techniques

In this chapter, several experimental techniques used in the discovery and follow up studies of antiskyrmions will be briefly introduced.

3.1 Focused ion beam (FIB)

There are two major sources of samples in the research of skyrmions: bulk materials [8] and thin film deposition [9]. Bulk materials are usually favored for the discovery of a new type of skyrmion, since the high quality of the single crystal, which is ensured in bulk crystal growth, is essential for the DMI interaction. One of the most popular experimental techniques of skyrmion research is LTEM, which will be introduced in the next section. Because the electron beam needs to be transmitted through the thickness of the sample, the thickness of the sample usually cannot be greater than ~300 nm. **FIB** technique is used to fabricate a thin lamella from the bulk crystal for LTEM studies.

The FIB technique, first developed in 1975 [60], has a commercial history of ~20 years. Instead of using electrons such as in the technique of Scanning Electron Microscopy (SEM), a beam of Ga ions is focused and used to etch the sample with the help of computer-controlled sample surface scanning. Nowadays, in a commercial FIB workstation, multiple functions are integrated into the high vacuum chamber with a multi-axis tilt stage for the TEM sample preparation, such as SEM, FIB etching, FIB imaging, FIB deposition. The two FIB systems used for the studies presented in this thesis in our institute are shown in Fig. 3.1. A typical FIB sample preparation

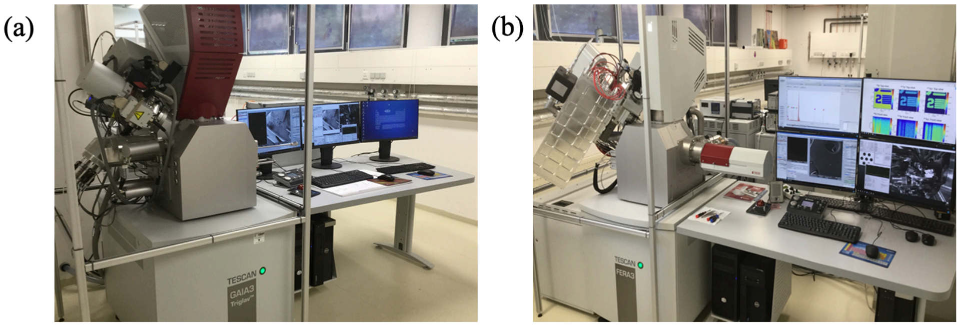

Figure 3.1: FIB workstations. (a) Model GAIA 3 Ga^+ FIB from TESCAN company with ultimate FIB spatial resolution <2.5 nm at 30 kV (b) Model FERA 3 Xe plasma FIB from TESCAN company with FIB spatial resolution <15 nm at 30 kV. Large scale milling speed ~50 times faster than Ga^+ FIB.

procedure is shown in Fig. 3.2.

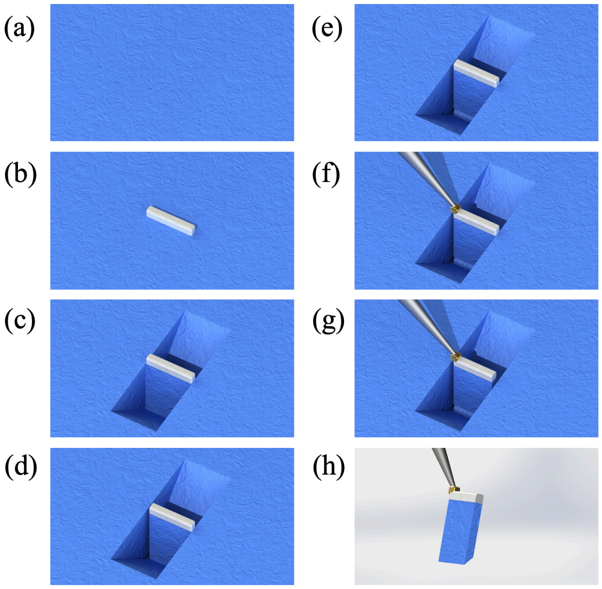

Figure 3.2: A typical FIB lamella fabrication procedure. (a) Bulk sample surface before fabrication, (b) deposit Pt protection layer, (c) etching away material using "stairs etching" technique, (d) etch away left part of the lamella, (e) etch away the bottom part of the lamella, (f) deposit Pt glue material (a different color is used just to distinguish Pt used in different steps), (g) etch away right part of the lamella and (h) final fabricated lamella.

3.2 Lorentz transmission electron microscopy (LTEM)

The transmission electron microscope is one of the most powerful tools to investigate a sample's structure. Due to the much smaller wavelength of electron compared to optical light, the spatial resolution of TEM is much higher. TEM can also be used to study the magnetization structure in the Lorentz mode [61]. When the electron wave passes through the sample, a phase gain will be added due to the magnetization of the sample according to the Aharonov–Bohm effect [62]. After propagating along the column axis, the gained phase will form the LTEM pattern. The working principle will be discussed below and in the next chapter.

Here, we only discuss the most widely used Fresnel mode of LTEM for Chiral magnetic nanostructure (**CMN**) studies. Because of the Aharonov-Bohm effect [62], when an electron passing along the LTEM column axis (defined as z-axis) and penetrates through the sample, it gains a phase shift of φ_m.

$$\varphi_m = -\frac{\pi}{\phi_0}\int A_z \,\mathrm{d}z \tag{3.1}$$

, here $\phi_0 = \frac{h}{2e} = 2.068 \times 10^{-15}\,\mathrm{Wb}$ is the magnetic flux quantum and A_z is the z-component of the magnetic vector potential. The phase shift φ_m is the measured physical object in this technique and basically determines the final LTEM pattern. The magnetic vector potential can be obtained from the magnetization distribution [63, 64]

$$\overrightarrow{A}(\overrightarrow{r}) = \frac{\mu_0}{4\pi}\int \overrightarrow{M} \times \frac{\overrightarrow{r} - \overrightarrow{r'}}{\left|\overrightarrow{r} - \overrightarrow{r'}\right|^3}\mathrm{d}^3\overrightarrow{r'} \tag{3.2}$$

, where $\overrightarrow{M}$ is the magnetization and μ_0 is the vacuum permeability. Combined with the relationship between magnetic field $\overrightarrow{B}$ and magnetic vector potential and by performing in the colum axis direction some integration, we can find:

$$\overrightarrow{B} = \overrightarrow{\nabla} \times \overrightarrow{A} \tag{3.3}$$

$$\int B_x \,\mathrm{d}z = \int \frac{\partial A_z}{\partial y}\,\mathrm{d}z - A_y\Big|_{z=-\infty}^{z=+\infty} = \frac{\partial \int A_z \,\mathrm{d}z}{\partial y} = -\frac{\pi}{\phi_0}\frac{\partial \varphi_m}{\partial y} \tag{3.4}$$

$$\int B_y \,\mathrm{d}z = -\int \frac{\partial A_z}{\partial x}\,\mathrm{d}z + A_x\Big|_{z=-\infty}^{z=+\infty} = -\frac{\partial \int A_z \,\mathrm{d}z}{\partial x} = \frac{\pi}{\phi_0}\frac{\partial \varphi_m}{\partial x} \tag{3.5}$$

, where x and y-axis are the TEM coordinates in-plane. At a far away distance with respect to the sample, the magnetic vector potential will be zero. So, the measured phase shift actually corresponds to the magnetic field $\overrightarrow{B}$ integrated, rather than directly corresponding to the magnetization [64].

LTEM is one of the most favored techniques to study magnetic nanostructures due to its several advantages. i) The measurement is in real-space, which is more straightforward compared to reciprocal space techniques such as small-angle neutron scattering [28]. ii) With high spatial resolution, the acquisition time is short compared with scanning probe techniques such as MFM [65]. iii) It can distinguish between several kind of skyrmions by the corresponding different LTEM patterns.

Fig 3.3 shows the LTEM setup used in our work. It has a spatial resolution ~40 nm that depends on the defocus distance used. A magnetic field can be applied of up to ~2.3 T. A double tilting sample holder can be used to allow for tilting the sample in all the in-plane directions up to ~30° with respect to the column axis. The measurement can be performed in liquid nitrogen or liquid helium temperatures depending on the sample holder used. By using another sample holder, it is also possible to inject current/voltage pulses to measure the magnetization dynamical behavior.

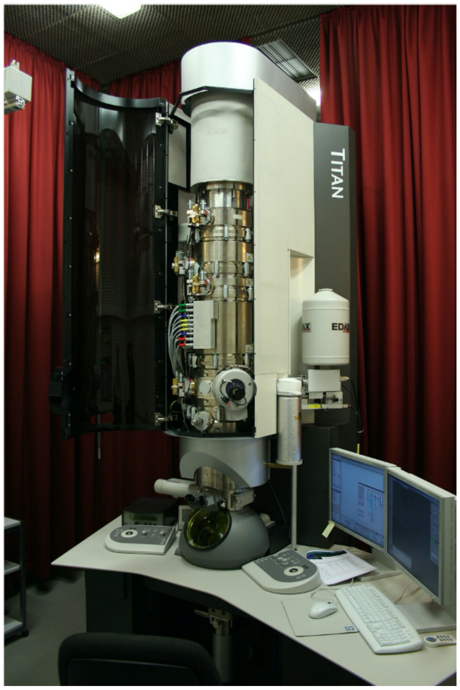

Figure 3.3: Lorentz Transmission Electron Microscopy with model Titan from the company FEI.

3.3 Magnetic force microscope (MFM)

MFM [66] is a type of atomic force microscopy. By using a tip that is magnetized, thereby interacting with the stray field created by the magnetization of the sample, the magnetization can be measured with a scanning probe microscopy technique with a spatial resolution of the order of <40 nm.

Compared to the LTEM technique, the MFM method is relatively slow. For a typical LTEM image, the acquisition time is less than 1 min. However, for MFM measurements, it is usually on the order of an hour. Due to the shape of the tip, the MFM tip is usually sensitive to the out of plane component of the magnetization, thus cannot distinguish the type of skyrmion as is possible using LTEM. However, MFM can measure the sample with thicknesses higher than that is measurable in the LTEM. Thus, MFM and LTEM are excellent complementary techniques to each other.

MFM experiments are carried out in a commercial variable temperature system in our group, as shown in Fig. 3.4, equipped with a 2D vector superconducting magnet, which can generate a magnetic field of 3 T in plane and 9 T perpendicular to the sample surface. We typically use magnetic tips purchased from Nanosensors (PPP-LM-MFMR). The soft coating on the magnetic tip ensures a low disturbance of the magnetic samples so that a higher spatial resolution (~20 nm) can be achieved. Before measuring, the tip magnetization needs to be initialized by a small permanent magnet. The topographic and magnetic contrast can be simultaneously measured. Typically, the tip first interacts with the sample in the tapping mode to acquire the surface topography and is then lifted to some distance, e.g. 80 nm, above the sample surface to record the magnetic texture. We use the phase-detection technique.

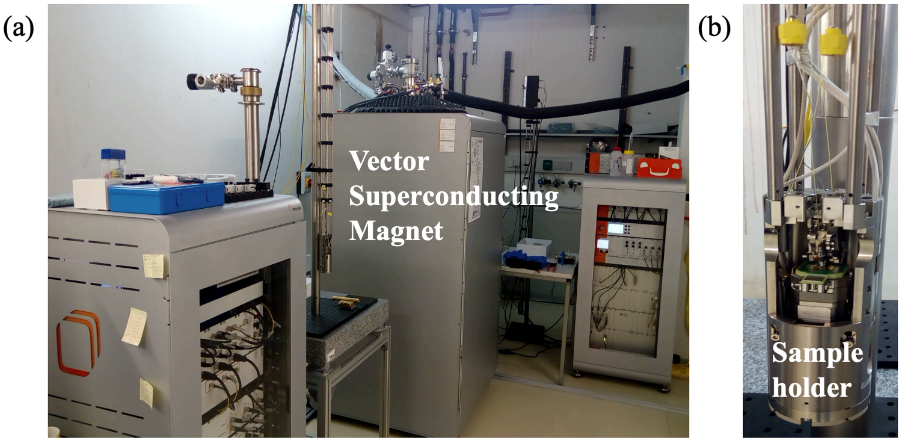

Figure 3.4: MFM setup with model AttoLiquid MFM I from the company Attocube. (a) Chambers for low-temperature measurement and superconducting vector magnet. (b) Sample holder with the magnetic tip and piezo stage.

3.4 Kerr microscope

The Magneto-optical Kerr effect (MOKE) was discovered in 1877 by John Kerr [67]. When a liner-polarized light is reflected from a magnetic material, its plane of polarization and ellipticity will change, in a manner that is proportional to the magnetization. The origin of MOKE is the spin-orbit interaction that occurs within a magnetic material between the electron spin and the electric field of the light. So, there is the antisymmetric component of the non-diagonal component of the dielectric tensor. The incoming linear light can be treated as a superposition of a left-handed and a right-handed circularly polarized light. Due to the magnetization, the absorption and refractive index for the left and right-handed circular polarized light is different, thus resulting in the rotation of the polarization plane and the change in ellipticity.

By combining the MOKE and optical microscopy we have a Kerr microscope [21]. The Kerr microscope can measure in real-time the magnetic structure at a spatial resolution in the micrometer range, limited by the wavelength of light. We use a variable temperature Kerr microscope setup, as shown in Fig. 3.5. In this Kerr microscope, a magnetic field of up to 3000 Oe can be applied along an arbitrary in-plane direction or up to 500 Oe along the out of plane direction. The measurement temperature can be varied from 4 K to 350 K. By using an image analysis-based drift compensation feedback algorithm, the sample can be stabilized within ~100 nm.

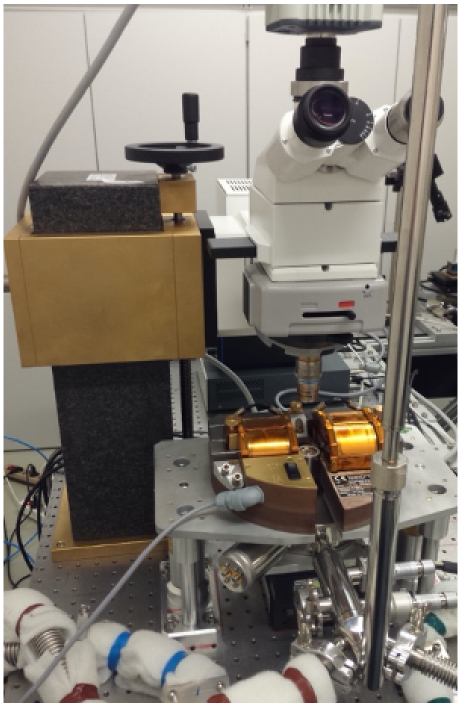

Figure 3.5: Kerr microscope system from EVICO GmbH and upgraded to variable temperature capability.

3.5 Scanning transmission X-ray microscope (STXM)

Besides electron and visible light, X-rays can also be used to measure a magnetic signal. For a ferromagnetic material, the electron state density around the Fermi suface for spin up and spin down is different. So X-rays with left/right-hand polarization are absorbed differently due to the selection rule. This effect is called X-ray Magnetic Circular Dichroism (XMCD) [68]. Since the absorbing edge for different materials corresponds to different energies, the XMCD technique is element-specific. By using the XMCD effect, the measured contrast directly corresponds to the magnetization. This is in contrast with LTEM where the contrast corresponds to the gained phase shift, or MFM, where the contrast corresponds to the stray field, so XMCD measurements are much more straightforward to interpret. By using a zone-plate, which uses diffraction rather than refraction or reflection, the X-ray beam can be focused down to ~20 nm in the beamline **MAXYMUS** (MAgnetic X-ray Microscope with UHV Spectroscopy) in the synchrotron BESSY in Berlin, Germany [69]. One disadvantage of this method is that the measurement beam time is quite limited.

In this beamline, the measurement temperature can range from room temperature down to 80 K. The magnetic field can be applied by the motor-controlled rotation of 4 permanent magnets. In this STXM, not only static measurements can be measured, but pump and probe time-resolved dynamical measurements can also be performed by using a sample holder equipped with a high-frequency capability to apply a microwave pump, which is synchronized with the synchrotron radiation probe. Several studies of current-induced skyrmion motion have been performed with this technique [44, 46].

Chapter 4

Magnetic antiskyrmions above room temperature in tetragonal Heusler materials

As discussed in previous chapters, the stabilized magnetization structure of skyrmions has been found in systems with broken inversion symmetry, where the DMI prefers a swirling magnetic state [28, 70]. Two types of skyrmions, Bloch [8, 28] and Néel types [10], where spin rotations by analogy to the the two types of Bloch and Néel domain walls, have been found by experiment. However, antiskyrmions had not been reported yet before our work. Some previous work reported antiskyrmions in Co/Pt multilayers [71], which are rather simply achiral spin textures or complex spin structures in the B20 compound MnGe are, by simulation, to be arrays of skyrmions, and antiskyrmions [72]. The crystal symmetries of these materials intrinsically do not allow for the formation of antiskyrmions. In this chapter, we present an LTEM study of antiskyrmions in a family of acentric tetragonal Heusler compounds with D_{2d} crystal symmetry.

In this work [73], our coworker Ajaya K. Nayak performed the LTEM measurements using a sample synthesized by Vivek Kumar and Ajaya K. Nayak. The neutron diffraction was performed by Ajaya K. Nayak and Roshnee Sahoo. I worked on the micromagnetic simulations, LTEM image simulations, LTEM image analysis, etc.

The figures included in this chapter are reprinted from [73], for which I am one of the main authors. (Material from: Nayak, A. K., Kumar, V., Ma, T., Werner, P., Pippel, E., Sahoo, R., ... & Parkin, S. S., Magnetic antiskyrmions above room temperature in tetragonal Heusler materials, Nature, published 2017, Springer Nature.)

4.1 Material and its structure and magnetization characterization

For the stabilization of antiskyrmions, the high quality of the single crystal is a crucial requirement. The focus has been on the Heusler compound $Mn_{1.4}Pt_{0.9}Pd_{0.1}Sn$ and $Mn_{1.4}PtSn$. In a high-purity argon atmosphere, stoichiometric amounts of the constituent elements are arc melted to produce polycrystalline ingots of $Mn_{1.4}PtSn$ and $Mn_{1.4}Pt_{0.9}Pd_{0.1}Sn$. Then, they were annealed at 1073 K for one week. Finally, they are quenched in an ice-water mixture.

Various methods were used to characterize the sample.

Firstly, X-ray powder diffraction (**XRD**)technique was used. From the Rietveld refinement of the experimental results the $Mn_{1.4}PtSn$ crystals are found to have an acentric tetragonal structure corresponding to the space group $I\bar{4}2m$ (space group number 121) [73]. According to the analysis method discussed in Section 2.1, this space group corresponds to the DMI type needed for the stabilization of antiskyrmions.

Secondly, transmission electron microscope (TEM) technique was used to study the sample structure. The TEM sample was prepared by Ga^+ FIB from a polycrystalline $Mn_{1.4}Pt_{0.9}Pd_{0.1}Sn$ ingot. A lamella with a thickness of ~100 nm in the thick flat region and ~50 to 70nm at the thinner edge was prepared. From the selected area diffraction patterns (**SAED**) and high-resolution scanning transmission electron microscope (**STEM**) results, the atomic arrangements and the crystal structure was clearly identified [73]. The structure measured in the TEM studies agrees with the conclusions derived from the XRD measurements, which together confirms the crystal structure of the sample.

Thirdly, we use a vibrating sample **SQUID** magnetometer (MPMS 3, Quantum Design) to perform magnetic hysteresis loop measurements for $Mn_{1.4}PtSn$ and $Mn_{1.4}Pt_{0.9}Pd_{0.1}Sn$ under various temperatures. A soft magnetic behavior was found [73]. At 2 K for both compounds which also show similar saturation moments of ~$4.5\mu_B$. For the compound of $Mn_{1.4}PtSn$, the Curie temperature (T_C), is around 400 K with a second transition below

~160 K. Such behavior suggests there is a temperature-dependent reorientation of the moments in the Mn sub-lattices at the lower temperature. The compound $Mn_{1.4}Pt_{0.9}Pd_{0.1}Sn$ displays a similar T_C as $Mn_{1.4}PtSn$. However, the spin-reorientation transition at low temperatures is decreased to around 125 K. Powder neutron diffraction measurements confirms a change in the magnetic structure at this temperature [73].

4.2 Magnetic structure and LTEM pattern

The LTEM pattern is one of the most straightforward techniques to distinguish different types of CMN. For antiskyrmions a 4-spot pattern with alternating black and white contrast is a unique signature, whereas the LTEM patterns are very different for Bloch and Néel skyrmions. In the last chapter, the method to calculate the phase shift is explained in detail. In this section, we will calculate the LTEM pattern.

The magnetic structure of a Bloch, skyrmion, a Néel skyrmion, and an antiskyrmion is shown in Fig. 4.1a-c. The corresponding helimagnetic structuress are shown in Fig. 4.1d-f. In an antiskyrmion, cross-sectional schematics along four different crystal directions show both helicoid and cycloid spin propagations (shown in Fig. 4.1b and Fig. 4.1e) . This unique rotation of the spin will result in a distinct LTEM pattern.

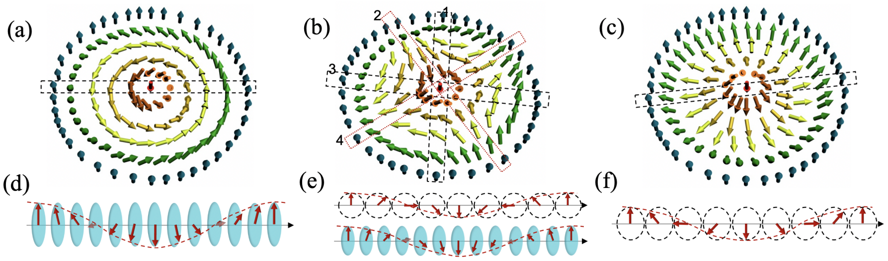

Figure 4.1: Magnetic structure of skyrmions and antiskyrmions. Magnetic structure of (a), Bloch skyrmion, (b), antiskyrmion, and (c), Néel skyrmion. (d), Cross-section of a Bloch skyrmion as indicated by the dashed rectangle in a), which shows a helix structure. (f), Cross-section of a Néel skyrmion as indicated by the dashed rectangle in c), which shows a cycloid structure. (e) Cross-section of an antiskyrmion as indicated by the dashed rectangle in b), which shows both helix and cycloid structure.

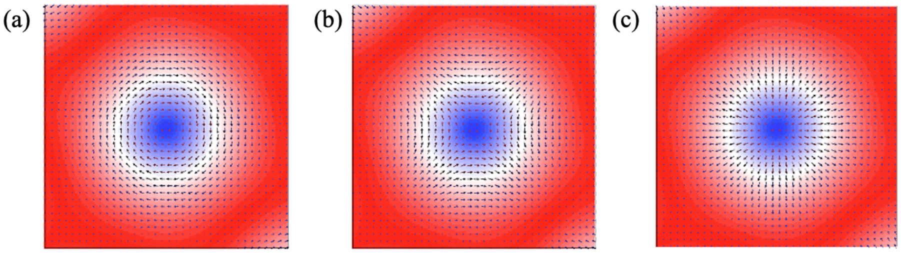

Figure 4.2: Simulated magnetic structure of skyrmions. Magnetization structure of (a) Bloch-skyrmions, (b) antiskyrmions and (c) Néel-skyrmions. The size of the shown area is 280 nm×280 nm. The arrows represent the in-plane magnetization, and the color shows the out of plane magnetization.

Micromagnetic simulated magnetization structures are used as input for the LTEM pattern simulation. Typical Bloch, Néel, and antiskyrmion magnetization simulated structures are shown in Fig. 4.2. The details of the micromagnetic simulations will be discussed in the next section. From the above magnetization texture, the LTEM image can be calculated [61, 63, 74, 75]. In reciprocal space, the magnetic phase component can be expressed as:

$$\widetilde{\varphi} = \frac{i\pi\mu_0 M_s t}{\Phi_0}\left(\frac{\widetilde{m}_x k_y - \widetilde{m}_y k_x}{k_x^2 + k_y^2}\right) \tag{4.1}$$

where μ_0 is vacuum permeability, M_s is saturation magnetization, $\widetilde{m}_x$ and $\widetilde{m}_y$ are the magnetization unit vector in reciprocal space. This calculation method is in reciprocal space, considering the thin film structure with thickness t. At the back focal plane of the objective lens, the deviation of the electron beam can be expressed as:

$$g\left(k_x, k_y\right) = \iint exp\left[i\varphi(x,y)\right] exp\left[-2i\pi(yk_y + xk_x)\right] \mathrm{d}x\,\mathrm{d}y \tag{4.2}$$

here k_x, k_y are the x and y components of k-vector in reciprocal space. From the back focal plane, the electrons propagate, thus we consider the “transfer function” as:

$$t\left(k_x, k_y\right) = A\left(k_x, k_y\right) exp\left\{-2i\pi\left(\left[\frac{C_s\lambda^3\left(k_x^2 + k_y^2\right)}{4}\right] - \left[\frac{\Delta z\lambda\left(k_x^2 + k_y^2\right)}{2}\right]\right)\right\} \tag{4.3}$$

where the λ is electron wavelength, $A(k_x, k_y)$ is the pupil function, C_s is the spherical aberration of the objective lens. The defocus distance Δz is an important experimental parameter, which largely determines the final LTEM contrast. Thus, by calculating the inverse Fourier transform, the LTEM intensity can be obtained, as:

$$I\left(x', y'\right) = \left| \iint g(k_x, k_y) t(k_x, k_y) exp\left[-2i\pi(y'k_y + x'k_x)\right] \mathrm{d}k_x \, \mathrm{d}k_y \right|^2 \tag{4.4}$$

Under different Δz, the LTEM images calculated are shown in Fig. 4.3. The LTEM images have the same feature as the phase shift. When in focus, there is no LTEM contrast. As the defocus distance becomes larger, the contrast gets larger and more divergent. When the defocus distance is rather reduced, the LTEM contrast also becomes the opposite.

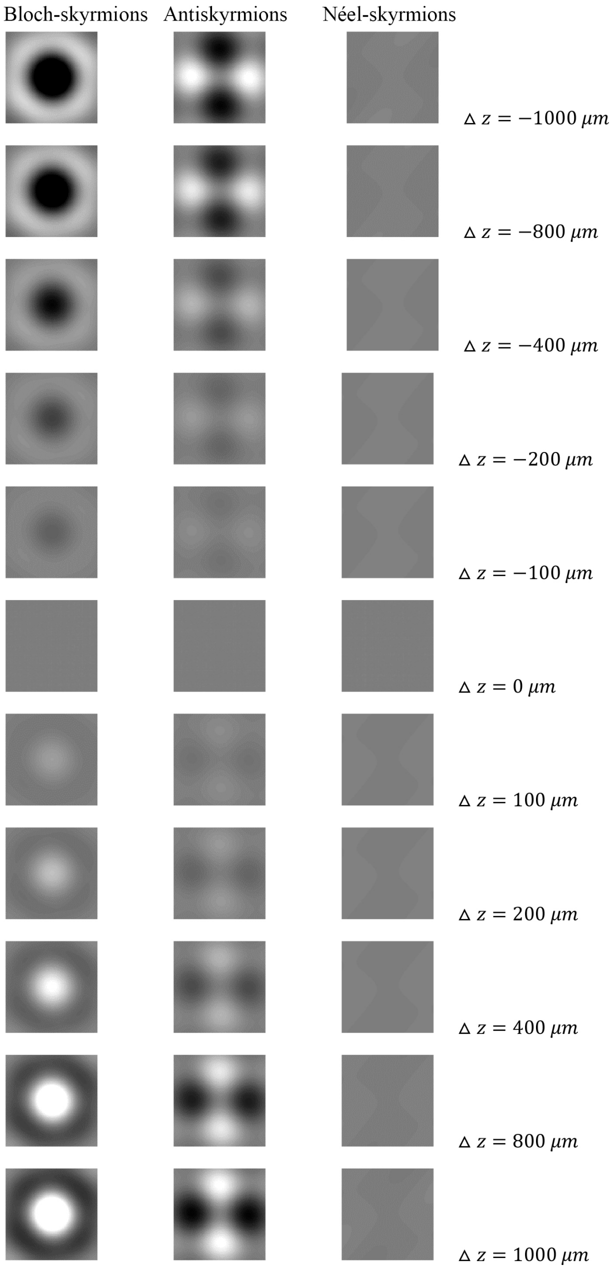

Figure 4.3: Simulated LTEM images as a function of Δz. LTEM simulated images of Bloch-skyrmions, antiskyrmions, and Néel-skyrmions as a function of Δz.

4.3 LTEM measurement of antiskyrmion

In order to get rid of the ”bend-contour” effect and to better stabilize antiskyrmions, the LTEM measurements are performed under certain protocols [73], since the temperature/field applied history is found to have a criticall influence. LTEM measurements at room temperature and zero applied magnetic field are shown in Fig. 4.4a-b. In Fig. 4.4a, there is no LTEM contrast since the measurement is performed in focus. In Fig. 4.4b, an underfocused LTEM image gives an additional contrast modulation that can be observed in the area of the sample with [001] orientation. The experimental result under different defocus distances agrees well with the LTEM pattern simulations shown in the previous section. These stripe-like contrasts correspond to a helimagnetic magnetic structure. The sinusoidal variation of the LTEM contrast has a period around ~135 nm, as shown in the inset of Fig. 4.4b. By applying magnetic field along [001], the helimagnetic state evolves into antiskyrmions, as shown in Fig. 4.4c.

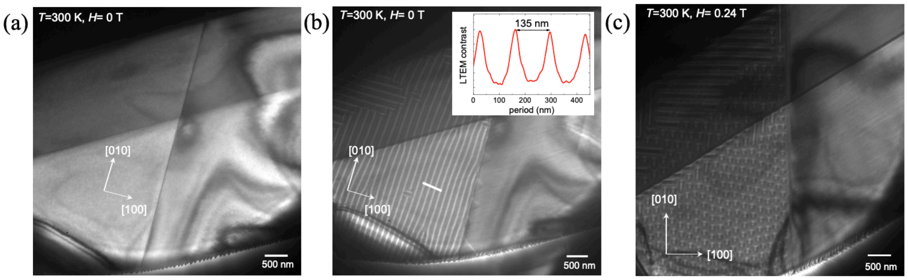

Figure 4.4: LTEM contrast at room temperature. (a) In-focus LTEM image with no LTEM contrast (b) under-focused LTEM image at zero field and (c) with a field of 0.24 T. Helical magnetic structure and antiskyrmions appears in (b-c), respectively. The inset of b depicts the sinusoidal change of the LTEM contrast with the period of the helix. The scanned region is marked by a line.

Under a field of 0.29 T field applied parallel to the [001] direction, a magnified underfocused LTEM image of a single antiskyrmion is shown in Fig. 4.5a. Clearly, it shows two bright and two dark spots along the crystal directions of [010] and [100]. In the overfocused LTEM image, the LTEM contrast is reversed, as shown in Fig. 4.5b. These pictures clearly matche the above-calculated LTEM patterns, as shown in Fig. 4.3, confirming the stabilization of antiskyrmions. Fig. 4.5c shows an hexagonal lattice of antiskyrmions. Due to a slight misorientation ($\approx \pm 3^\circ$) of the sample away from the [001] direction, a slight distortion of the lattice might be induced by the small in-plane magnetic field. Due to the tetragonal D_{2d} symmetry, it is expected that oblique fields will induce some antiskyrmion lattice distortions.

A micromagnetic simulation of the oblique field's influence on the antiskyrmion lattice is shown in Fig. 4.5d. It can be straightforwardly understood that the in-plane component of the magnetic field broadens the region of the magnetization within the antiskyrmion along the field, whereas the converse is the case of regions that are oppositely magnetized. A distortion of the antiskyrmions can be seen in Fig. 4.5e when the magnetic field was applied at an angle of about 20° with respect to the [001] direction. Up to the maximum possible tilt angle allowed by the LTEM sample holder, we find that the antiskyrmions are stable. The antiskyrmions appear as elliptical shapes in the Lorentz micrographs with the center of the antiskyrmions off-centered. This distortion originates from both the tilting of the antiskyrmions themselves as well as from contributions to the Lorentz imaging from the tilted magnetizations. The stability up to a large tilting angle is reproduced by micromagnetic simulations. As the rotation decreases from Fig. 4.5e to Fig. 4.5g, the 4-spot LTEM pattern of the antiskyrmions becomes clearer. A nearly perfect 4-spot pattern in a regular hexagonal lattice can beseen in Fig. 4.5i, where 0.29 T field is applied along the direction [001] (less than ±3° misalignment). When the field is increased to 0.33 T, the lattice is no longer hexagonal (Fig. 4.5j). A mixed antiskyrmion lattice and field polarized state start to emerge. In still higher fields, antiskyrmions start to disappear in the thinner region of the sample, as shown in Fig. 4.5k. Finally, above 0.49 T, the lattice becomes an array of single antiskyrmions, as shown in Fig. 4.5l. From the above measurements we show the high stability of antiskyrmions, even up to room temperature, for a large magnetic field region, and for large tilting angles.

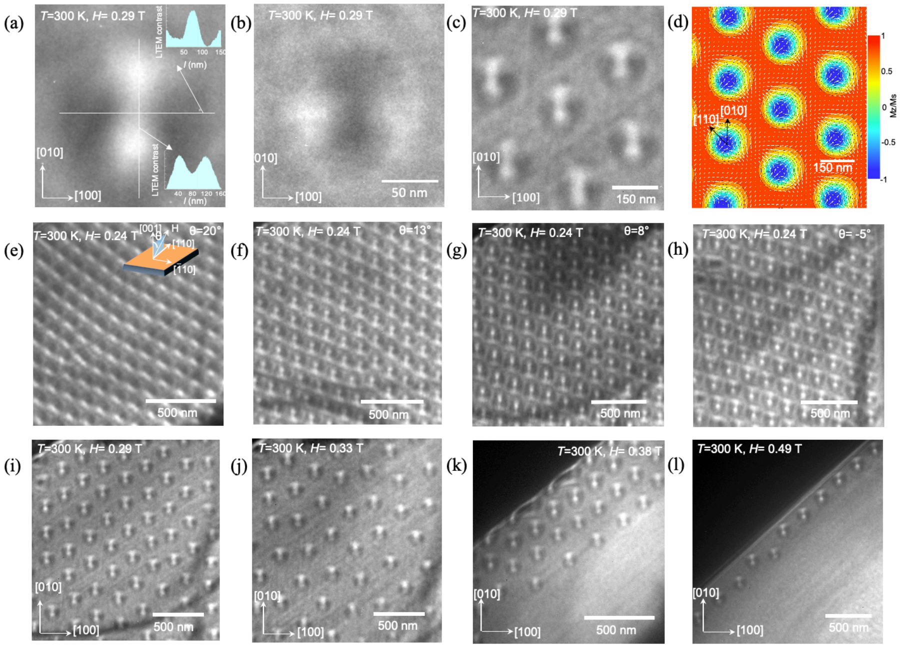
(a)
T=300 K, H= 0.29 T
LTEM contrast
50 100 150
l (nm)
LTEM contrast
40 80 120 160
l (nm)
[010]
[100]
(b)
T=300 K, H= 0.29 T
[010]
[100]
50 nm
(c)
T=300 K, H= 0.29 T
[010]
[100]
150 nm
(d)
[110]
[010]
150 nm
1
0.5
0
-0.5
-1
Mz/Ms
(e)
T=300 K, H= 0.24 T
[001]
H
θ=20°
[110]
[110]
500 nm
(f)
T=300 K, H= 0.24 T
θ=13°
500 nm
(g)
T=300 K, H= 0.24 T
θ=8°
500 nm
(h)
T=300 K, H= 0.24 T
θ= -5°
500 nm
(i)
T=300 K, H= 0.29 T
[010]
[100]
500 nm
(j)
T=300 K, H= 0.33 T
[010]
[100]
500 nm
(k)
T=300 K, H= 0.38 T
[010]
[100]
500 nm
(l)
T=300 K, H= 0.49 T
[010]
[100]
500 nm

Figure 4.5: Room temperature antiskyrmions. (a) Under-focused LTEM image of a single antiskyrmion. The insets show the LTEM intensity profiles along the [010] and [100] directions, marked by lines. (b) Over-focused LTEM image of the single antiskyrmion, where the LTEM contrast is reversed (c) Under-focused LTEM of a hexagonal lattice of antiskyrmions. (d) Simulation of an antiskyrmion lattice in a tilted field. (e-h) Under-focused LTEM images with 0.24 T field under different rotation angle (θ). (i-l) Under-focused LTEM images of different antiskyrmions phase taken under different field amplitudes.

4.4 Micromagnetic simulations of antiskyrmions

We use micromagnetic simulations to reproduce the above-measured helix to antiskyrmion lattice to field polarized state with increasing applied magnetic field. In order to obtain the ground state, a high-temperature energy term is initially used in the OOMMF simulations, as mentioned in chapter 2.2.3, to overcome local energy barriers. Then the magnetization is relaxed while the temperature is gradually decreased to zero. The evolution of the antiskyrmion phase as a function of field is calculated. The following parameters are used: exchange stiffness $A = 1.2 \times 10^{-10}\,\mathrm{J\,m^{-1}}$, DMI $D = 6 \times 10^{-3}\,\mathrm{J\,m^{-2}}$, and saturation magnetization $M_s = 445\,\mathrm{kA\,m^{-1}}$. The calculated results are shown in Fig. 4.6a-f, which reproduces the field-induced phase change behavior. In the present simulation, M_s is measured by experiment. The values of A and D are estimated based on the size of the antiskyrmion and the magnetic fields applied. Since we have not considered the dipolar interaction, the estimated values of A and D used are only approximate as discussed in later chapters.

OOMMF is also used to simulate the antiskyrmion lattice under a tilted field. We keep a constant field amplitude of 0.24 T, and adjust the field tilting angle to 20°, 10°, 0°, −10° and −20° with respect to the [110] direction, shown in Fig. 4.7a-e. Initially, using the above-discussed field cooling calculation method, the antiskyrmion phase at zero tilt angle was calculated. Then, starting from this state, a tilt angle of −20° is applied in the simulation. The tilt angle was changed in 2° increments. The resulting state of the previous calculation is used as the initial state of the next calculation. These tilting calculations are all performed at zero temperature.

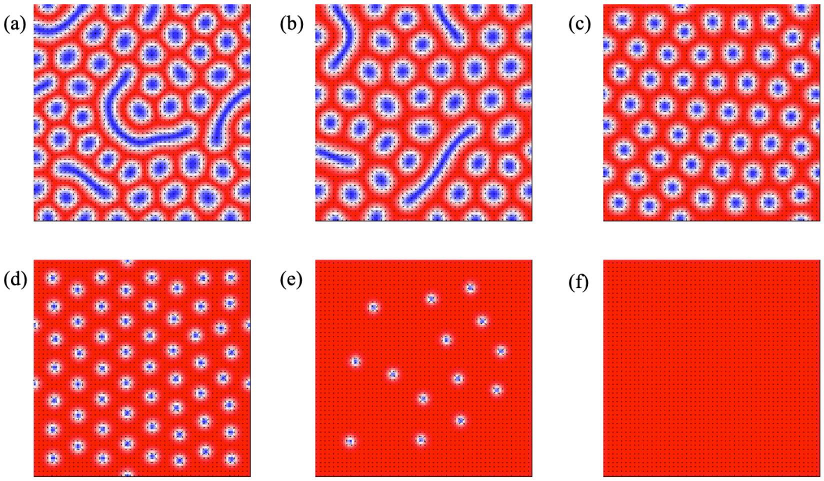

Figure 4.6: Simulated antiskyrmion phase as a function of H_z. (a) H_z =0.09 T, helix+antiskyrmion phase, (b) H_z =0.15 T, helix+antiskyrmion phase, (c) H_z =0.21 T, antskyrmion phase, (d) H_z =0.39 T, antikyrmion phase, (e) H_z =0.47 T, antiskyrmion + spin polarized state (f) H_z =0.50 T, spin polarized phase state.

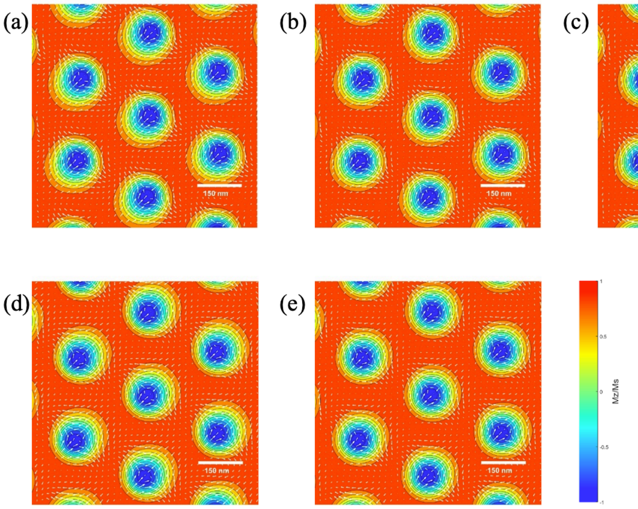

Figure 4.7: Simulated antiskyrmion lattice under tilt angle. The field amplitude is 0.24 T with a tilting angle of (a) 20°, (b) 10°, (c) 0° (d) −10° and (e) −20° away from [001] to the [110] direction.

4.5 Temperature and field dependent phase diagram of antiskyrmions

After the measurement at room temperature, we further study the temperature-field dependent phase diagram of the antiskyrmions. A typical result is shown below. At 350 K and 0.22 T, the underfocused LTEM patterns show a lattice of antiskyrmions (Fig. 4.8a). When the temperature is higher, lower fields are needed to stabilize the antiskyrmion phase. Antiskyrmions at 100 K and 0.33 T along [001] are shown in Fig. 4.8b. Then, results when the field is reduced to zero, are shown in Fig. 4.9: two symmetrical bright spots along [010] can be observed; However, the black spots become unclear. This zero-field antiskyrmion state could be a metastable state.

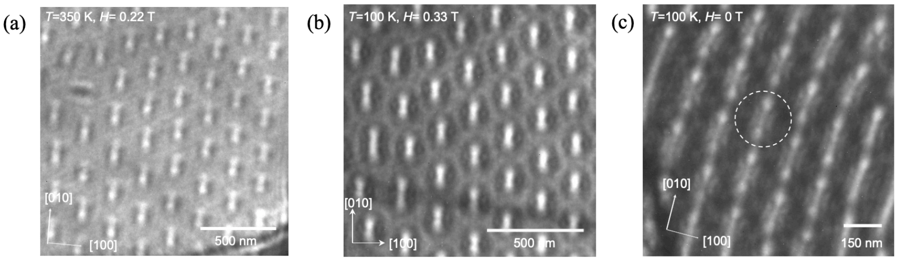

Figure 4.8: Antiskyrmions at 350 K and 100 K. Under-focused LTEM image taken at (a) 350 K in a field of 0.22 T, (b) 100 K and field of 0.33 T and (c) 100 K and zero field.

I programmed MATLAB software for the LTEM image analysis. The software has a user-friendly GUI (Graphical User Interface). After loading the image, the first left mouse click will determine the center of the antiskyrmion pattern, and the second mouse click will determine the outer edge of the antiskyrmion. Thus the size of the antiskyrmion can be estimated. By analyzing the position of the center of the antiskyrmion, the antiskyrmion lattice constant and angle can be calculated. A typical analysis result is shown in Fig. 4.9. Red circles show the antiskyrmions. The green lines indicate a hexagonal lattice. The blue numbers are the lengths of the antiskyrmion lattice (in nm). The red numbers indicate the angles of the antiskyrmion lattice(in degree).

The result of the analysis is shown in Fig. 4.10. Fig. 4.10a, shows the magnetization measurements at different temperatures of the bulk polycrys-

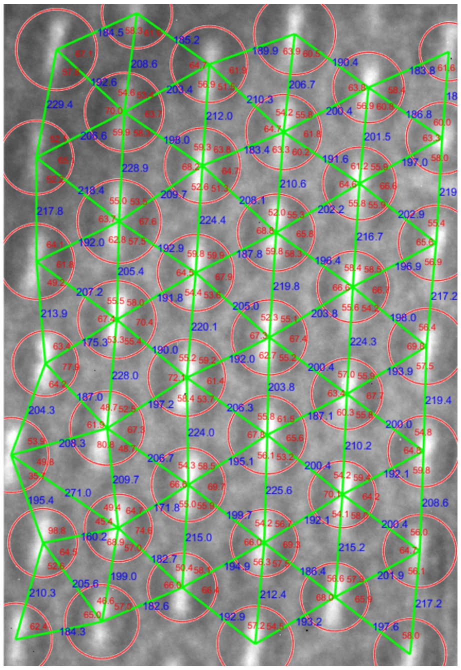

Figure 4.9: Typical image analysis result of the antiskyrmion lattice. The LTEM image used here is at 200 K under a field of 0.23 T.

talline $\mathrm{Mn_{1.4}Pt_{0.9}Pd_{0.1}Sn}$ [73]. It can be seen that $M(H)$ curves for temperatures down to 150 K exhibit a kink type of behavior. For temperatures below 100 K, the magnetization is still unsaturated up to 1 T. The LTEM image analysis results of the $H - T$ phase diagram are shown in Fig. 4.10b. The antiskyrmions can be found for the complete temperature region between 400 K down to the lowest allowed temperature in the current setup 100 K.

The antiskyrmion lattice spacing increases when H drives the system towards the field-polarized phase (Fig. 4.10c) with a decrease in the density of antiskyrmions (inset of Fig. 4.10c). The size of the antiskyrmions, however, over a wide temperature range (Fig. 4.10d) doesn't change much. The mean lattice angle and its standard derivation are shown in Fig. 4.10e and its inset, which is a good indication of the antiskyrmion lattice phase.

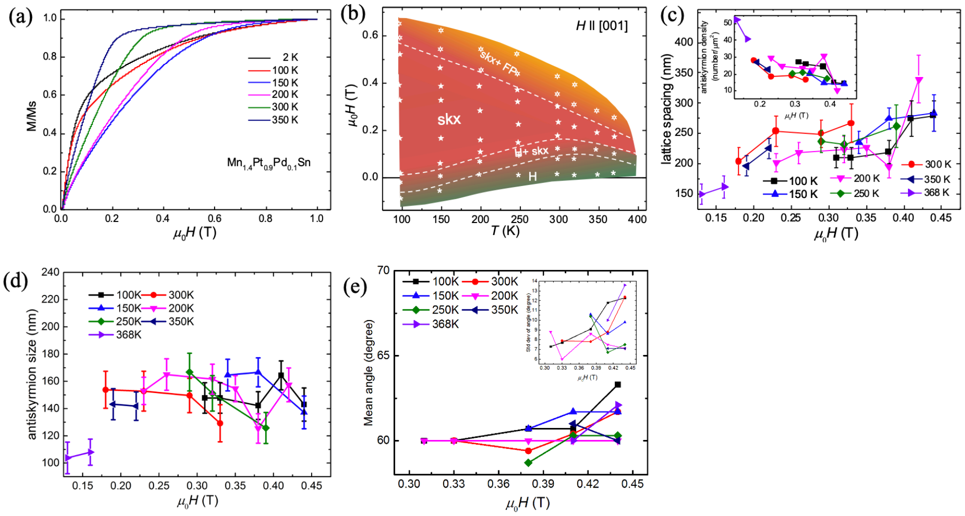

Figure 4.10: Antiskyrmions phase diagram and analysis. (a) M (H), under different temperatures for $Mn_{1.4}Pt_{0.9}Pd_{0.1}Sn$. The magnetizationis normalized with respect to the magnetization at 1 T. (b) H-T phase diagrams for $Mn_{1.4}PtSn$. The symbols used are: helical phase (H, big asterisk), antiskyrmions (skx, filled stars), mixed phase of helical and antiskyrmions (H+skx, asterisk), field polarized state (FP) and mixed phase of antiskyrmions and field-polarized (skx+FP, open stars). (c) Antiskyrmion lattice spacing at various temperatures and fields. The antiskyrmion density is shown in the inset. (d) Antiskyrmion size at various temperatures and fields. (e) Antiskyrmion lattice mean angle at various temperatures and fields. Standard deviation of the lattice angles are shown in the inset.

4.6 Summary and outlook

In this chapter, we have demonstrated the stabilization of antiskyrmions in $Mn_{1.4}Pt_{0.9}Pd_{0.1}Sn$ and it's phase diagram over a wide range of temperature and magnetic field. The antiskyrmion LTEM pattern, micromagnetic simulations and phase diagram analysis are explained in detail. The large tunable family of Heusler materials promises an even greater variety of skyrmionic structures in furure studies. For example, the number of valence electrons, the spin-orbit coupling, the symmetry of the crystal structure etc. can readily be manipulated. In particular, the ferrimagnetic structure of the family of tetragonal inverse Heusler materials makes it possible to tune the total magnetic moment to zero [49], to potentially support antiferromagnetic antiskyrmions. The most crucial condition in finding antiskyrmions in other systems is to explore material structures which have the correct crystal symmetry (D_{2d}) to stabilize antiskyrmions rather than skyrmion phases. Our extensive studies of antiskyrmions are described further in the next two chapters.

Chapter 5

Thickness dependent phase diagram: Intrinsic stability of magnetic antiskyrmions in the tetragonal inverse Heusler compound $Mn_{1.4}Pt_{0.9}Pd_{0.1}Sn$

The discovery of magnetic skyrmions in the B20 compound, such as MnSi, by the experimental method of small-angle neutron diffraction was carried out in bulk crystals. These experiments showed that skyrmions exist in three dimensions as arrays of tubes oriented along the magnetic field direction [28]. However, more recent work suggests that the lengths of these tubes is limited [76, 35, 37]. The skyrmion phase in bulk B20 compounds is found only for a very small magnetic field (B)- temperature (T) parameter range [28]. It also has been found that in thin lamellae (~100 nm) of MnSi and FeGe, that the B-T skyrmion stability region is much larger in very thin samples [30, 33]. In short, Bloch skyrmions in B20 compounds are very sensitive to the thickness of the host material.

After our experimental discovery of antiskyrmions, we were motivated to study the thickness dependence of the phase diagram for antiskyrmion systems. Using LTEM we have shown that antiskyrmions are found over a wide range of temperature and magnetic field in wedged lamellae formed from single crystals of $Mn_{1.4}Pt_{0.9}Pd_{0.1}Sn$ for thicknesses ranging up to ~250 nm. The temperature-field stability window of the antiskyrmions varies little with thickness, which is distinct from Bloch skyrmion systems. Using micromagnetic simulations, we show that this intrinsic stability of antiskyrmions can be accounted for by the symmetry of the crystal lattice, which is imposed on that of the DMI. These distinctive behaviors and stability of antiskyrmions makes them particularly attractive for spintronic applications.

In this work [77], the LTEM measurements were performed by Rana Saha and Abhay K. Srivastava. I was intimately involved in the experiment design and discussion, programed the LTEM analysis software, and performed the micromagnetic simulations.

The figures used in this chapter are reprinted from our paper [77], for which I am one of the authors. (Reprinted from [77]. Link to the Creative Commons license: https://creativecommons.org/licenses/by/4.0/)

5.1 LTEM measurement

The wedged shape lamella for LTEM studies were prepared from single-crystal grains within bulk polycrystalline $Mn_{1.4}Pt_{0.9}Pd_{0.1}Sn$. The sample has a thickness that varies from ~90 to ~250nm, a length of 8 µm and a width of 7 µm. The [001] direction is perpendicular to the lamella.

Three regions of different thicknesses are chosen for analysis. To ensure the precise position of these regions, I programmed an image analysis software (as shown in Fig. 5.1) to achieve this function by the following steps:

(i) Load the LTEM image, together with other experimental parameters (e.g., pixel to distance ratio)

(ii) Determine the boundaries of the lamella (shown as red/blue circles). The linear fitting result gives two boundary lines (shown as red/blue dashed lines).

(iii) The intersection of the two boundary lines determines the position of the origin. Two perpendicular lines (rotated slightly, as needed, with regard to the dashed lines) are determined as the X and Y coordinate axes.

(iv) Use the coordinate information to find the LTEM image in each region. The coordinates are: A (1.203 µm, 2.980 µm), B (4.123 µm, 3.053 µm) and C (5.685 µm, 3.038 µm). The size of these regions is 1 µm × 1 µm.

(v) Find the LTEM image under different temperatures and fields.

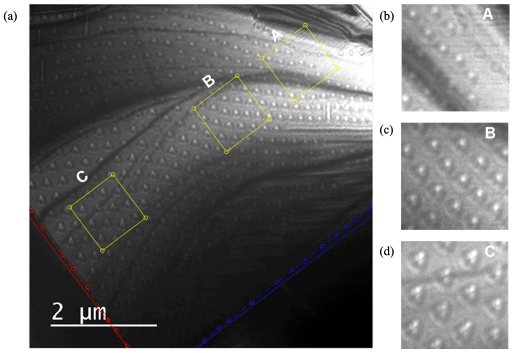

Figure 5.1: Determination of three different thickness regions. (a) The full LTEM image at 300 K and 0.192 T. (b-d) magnified LTEM images of the regions A, B and C shown in a. The thickness of them are, A: 164 nm< t < 197 nm; B: 213 nm < t <229 nm and C: 246 nm < t < 250 nm

Careful procedures are needed to ensure coherent thickness-dependent magnetic phase diagrams. A typical LTEM result at 300 K is shown in Fig. 5.2. Fig. 5.2a shows the helical phase in all the ranges of thickness at zero field: magnified images of three regions are shown in Fig. 5.2b. Fig. 5.2c-l shows LTEM imags with decreasing magnetic field strength. It can be found that the antiskyrmion region is a little enlarged as the lamella thickness becomes larger.

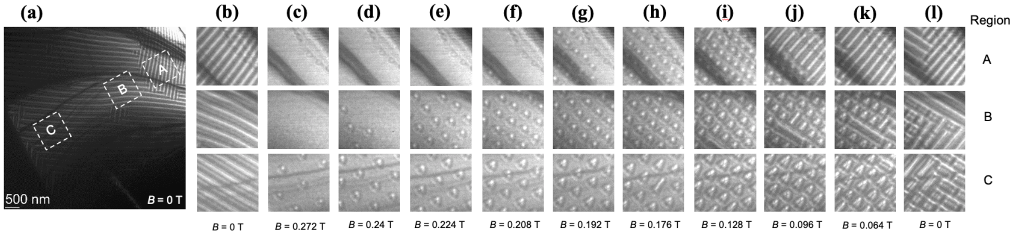

Figure 5.2: LTEM result at 300 K as a function of magnetic field. (a) LTEM image under zero magnetic field. (b-l) LTEM images as a function of magnetic field for the three thickness regions.

In Fig. 5.3, the temperature-dependence of the LTEM images under 0.16 T is shown. At 100 K, the helix state is seen for all thicknesses. At 150 K, coexistence of the antiskyrmion lattice and the helical phase is seen in regions A and B; while in region C, the helical state coexists with some isolated antiskyrmions (Fig. 5.3b). At 200 K, an antiskyrmion lattice is stabilized in A, while in B and C, an antiskyrmion lattice and a helical phase coexist (Fig. 5.3c). At 250 K and 300 K, the antiskyrmion lattice state is stabilized in all regions (Fig. 5.3d and Fig. 5.3e). At 350 K, the antiskyrmion lattice is found only in region C (Fig. 5.3f).

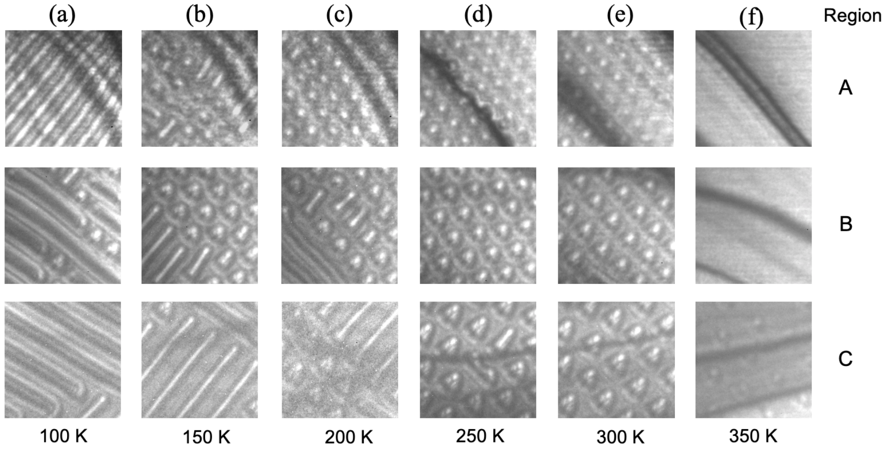

Figure 5.3: LTEM result as a function of temperature. The field applied is 0.16 T.

5.2 Phase diagram analysis

Image analysis software, similar to that discussed in the last chapter, is used to analyze the LTEM images in the selected regions. After loading the image into the LTEM image analysis software, the antiskyrmions positions and sizes are determined manually by mouse clicks. The antiskyrmions are then shown by red circles, as shown in Fig. 5.4. From the total area within the red circles divided by the total area size, the antiskyrmion area ratio is calculated. Because the size of the antiskyrmions show some dependence on the thickness of the lamella, the antiskyrmion area ratio is a better indication of which phase the system is in. The size, distance, and angles between the antiskyrmions can also be calculated, as discussed in the last chapter, as shown in Fig. 5.4.

Results of the analysis of the temperature and field dependence of the area ratio are shown in Fig. 5.5. Over a wide temperature up to above room temperature, as well as a wide magnetic field range, the antiskyrmion phase is found to be stable for all thicknesses. The antiskyrmion stability

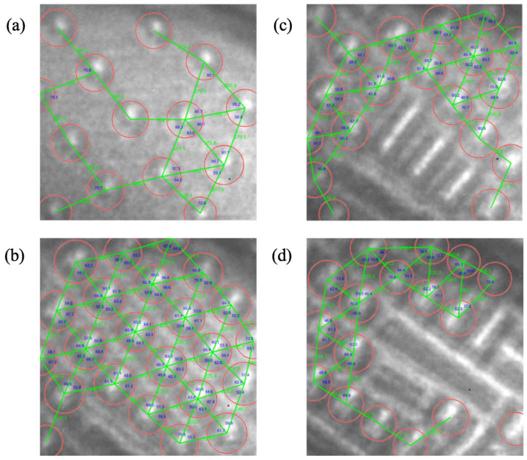

Figure 5.4: Area occupied ratio of the antiskyrmion lattice. Typical LTEM images analysed at 300 K for 4 different magnetic fields: (a) 28% area ratio (FM + aSk) at 0.224 T; (b) 53% area ratio (aSk) at 0.128 T; (c) 40% area ratio (H + aSk) at 0.112 T, and (d) 33% area ratio (H + aSk) at 0.048 T. These images correspond to region B. Here, 'H' means the helical phase; 'aSk' means the antiskyrmion phase; 'FM' means the ferromagnetic phase. The size of the above 4 LTEM images is 1 × 1µm^2.

phase range is qualitatively similar for all thicknesses with a tendency of a wider range for thicker parts of the lamella. At low temperatures, there is a greater difference between the ZFC and FC results. At 100 K, for ZFC, only a few isolated antiskyrmions can be seen (Fig. 5.5a-c), whereas for FC (Fig. 5.5d-f), many more antiskyrmions are found.

From the above LTEM phase diagram measurements, the antiskyrmion phase in $Mn_{1.4}Pt_{0.9}Pd_{0.1}Sn$ clearly shows considerable stability over a wide range of field and temperature, and which is not very sensitive to the thickness of the lamella. This is in stark contrast to the B20 materials. To explain the underlying physical origin of the very different antiskyrmion and skyrmion phase diagrams as a function of thickness, the following microscopic model is considered, which uses the Hamiltonians below for the D_{2d} and B20

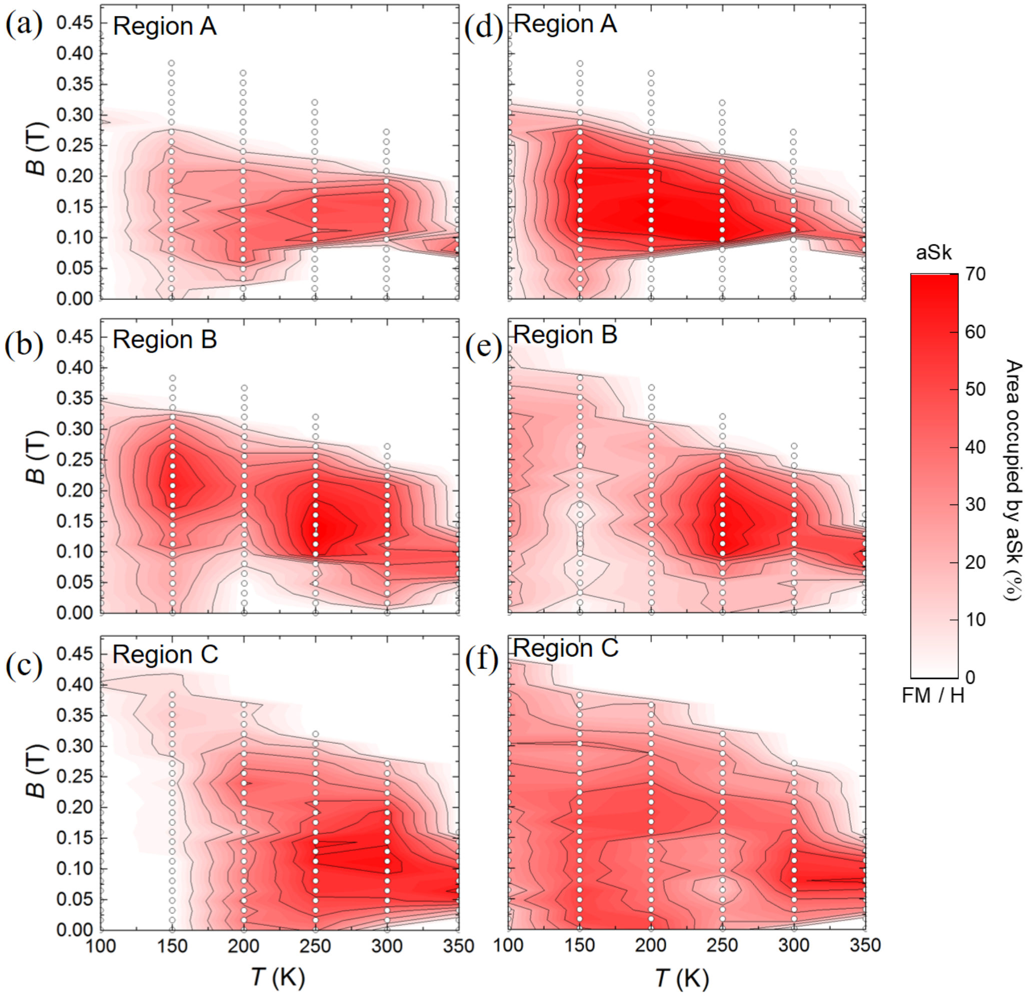

Figure 5.5: Magnetic phase diagram of different thickness. The temperature-field antiskyrmion area ratio of three regions A, B, and C of different thicknesses are analyzed, for both zero-field-cooling (ZFC) and field-cooling (FC) protocols. The area ratio around 70% corresponds to a pure antiskyrmion lattice. The white dots indicate where LTEM measurements were performed.

systems, respectively,

$$
\begin{aligned}
H_{B20} = &- J \sum_{\boldsymbol{r}} \overrightarrow{\boldsymbol{S}_{\boldsymbol{r}}} \cdot \left(\overrightarrow{\boldsymbol{S}_{\boldsymbol{r}+a\hat{\boldsymbol{x}}}} + \overrightarrow{\boldsymbol{S}_{\boldsymbol{r}+a\hat{\boldsymbol{y}}}} + \overrightarrow{\boldsymbol{S}_{\boldsymbol{r}+a\hat{\boldsymbol{z}}}} \right) - \overrightarrow{\boldsymbol{B}} \cdot \sum_{r} \overrightarrow{\boldsymbol{S}_{\boldsymbol{r}}} \\
&- D_{B20} \sum_{\boldsymbol{r}} \left(\overrightarrow{\boldsymbol{S}_{\boldsymbol{r}}} \times \overrightarrow{\boldsymbol{S}_{\boldsymbol{r}+a\hat{\boldsymbol{x}}}} \cdot \hat{\boldsymbol{x}} + \overrightarrow{\boldsymbol{S}_{\boldsymbol{r}}} \times \overrightarrow{\boldsymbol{S}_{\boldsymbol{r}+a\hat{\boldsymbol{y}}}} \cdot \hat{\boldsymbol{y}} + \overrightarrow{\boldsymbol{S}_{\boldsymbol{r}}} \times \overrightarrow{\boldsymbol{S}_{\boldsymbol{r}+a\hat{\boldsymbol{z}}}} \cdot \hat{\boldsymbol{z}} \right)
\end{aligned}
\tag{5.1}
$$

$$
\begin{aligned}
H_{D_{2d}} = &- J \sum_{\boldsymbol{r}} \overrightarrow{\boldsymbol{S}_{\boldsymbol{r}}} \cdot \left(\overrightarrow{\boldsymbol{S}_{\boldsymbol{r}+a\hat{\boldsymbol{x}}}} + \overrightarrow{\boldsymbol{S}_{\boldsymbol{r}+a\hat{\boldsymbol{y}}}} + \overrightarrow{\boldsymbol{S}_{\boldsymbol{r}+a\hat{\boldsymbol{z}}}} \right) - \overrightarrow{\boldsymbol{B}} \cdot \sum_{r} \overrightarrow{\boldsymbol{S}_{\boldsymbol{r}}} \\
&- D_{2d} \sum_{\boldsymbol{r}} \left(-\overrightarrow{\boldsymbol{S}_{\boldsymbol{r}}} \times \overrightarrow{\boldsymbol{S}_{\boldsymbol{r}+a\hat{\boldsymbol{x}}}} \cdot \hat{\boldsymbol{x}} + \overrightarrow{\boldsymbol{S}_{\boldsymbol{r}}} \times \overrightarrow{\boldsymbol{S}_{\boldsymbol{r}+a\hat{\boldsymbol{y}}}} \cdot \hat{\boldsymbol{y}} \right)
\end{aligned}
\tag{5.2}
$$

where J is the exchange stiffness, $\overrightarrow{B}$ is the external magnetic field, D_{B20} and $D_{D_{2d}}$ are the DMI coefficients of the B20 and D_{2d} structures $\overrightarrow{\boldsymbol{S}_{\boldsymbol{r}}}$ is the magnetization at position $\overrightarrow{\boldsymbol{r}}$, whereas $\overrightarrow{\boldsymbol{S}_{\boldsymbol{r}+a\hat{\boldsymbol{x}}}}$, $\overrightarrow{\boldsymbol{S}_{\boldsymbol{r}+a\hat{\boldsymbol{y}}}}$, $\overrightarrow{\boldsymbol{S}_{\boldsymbol{r}+a\hat{\boldsymbol{z}}}}$ are the magnetization values of the nearest cells in the x, y and z directions. In each case, the Heisenberg exchange and Zeeman energy terms are the same, but the DMI terms differ according to the distinct B20 and D_{2d} crystal structures [52]. For the B20 system, the DMI vector amplitude is the same in all the three directions , whereas in the D_{2d} system, the DMI vectors in the x and y directions have the same magnitude, but with opposite sign and the DMI vector amplitude is zero along z. It should be noted that the simulations are 3-dimensional since both Heisenberg and DMI exchange interactions have taken consideration of all the x, y, and z-directions. The influence of dipolar interactions is not included. This is because the dipolar energy term had been typically ignored in prior studies of skyrmions [78, 14]. The magnetic anisotropy energy term is also not included, because it will not much influence the major conclusions.

In the cubic B20-type materials, the DMI vector component along the thickness direction will give rise to a twisted structure of the magnetization along the thickness. This twist structure will result in a strong thickness dependent phase diagram as previously theoretically discussed [79, 35, 36, 78]. Experimentally, in both MnSi and FeGe materials, it has been shown that the skyrmion phase range shrinks with increasing thickness [30, 33]. Recently, experiments show that in FeGe, as the thickness increases to a critical value, the skyrmion-tube structure will break up into chiral bobbers [35, 80]. On the contrary, in the D_{2d} system, there is no such kind of DMI induced twist strcuture, which results in the much weaker thickness dependence of the phase diagram for antiskyrmions.

5.3 Micromagnetic simulation

Micromagnetic simulations based on the Hamiltonian above are performed, with OOMMF, to compare and explore the phase of antiskyrmion and skyrmion as a function of thickness. To ensure a controlled comparison, the same calculation parameters are used for the B20 and D_{2d} systems. The parameters used are: stiffness constant $J = 1.2 \times 10^{-10}\,\mathrm{J\,m^{-1}}$, saturation magnetization $M_s = 445\,\mathrm{kA\,m^{-1}}$, and $D_{B20} = D_{D_{2d}} = 6 \times 10^{-3}\,\mathrm{J\,m^{-2}}$ for the DMI, where the modified OOMMF code [81, 59] which allow for different kinds of DMI is used. These values are the same as those used in the last chapter [73]. The simulation cell size used is $40\,\mathrm{nm}\times 40\,\mathrm{nm}\times 40\,\mathrm{nm}$, since the calculation load is heavy. The total simulated size is $2000\,\mathrm{nm}\times 2000\,\mathrm{nm}\times 40\,\mathrm{nm}\times N_{Layer}$, where N_{Layer} is the layer number in the direction of the thickness. In-plane periodic boundary conditions were used. To obtain the ground state globally, an extremely high temperature is used at the beginning of the calculation to ensure any previous magnetic structure disappears. Then the temperature is decreased step by step to finally reach zero, where the calculation stops until a stable global ground state is stabilized. The UHH_ThetaEvolve, a extend class of OOMMF, is used as the temperature term. The temperature used starts at 5000000 and decreases by 1000000 in each step. At non-zero temperatures, 50000 calculation steps are performed, where each step corresponding to 1 ps. The high temperature number used is also due to the cell size used. Finally, when the temperature is decreased to zero, the calculation carries on until $\frac{\mathrm{d}m}{\mathrm{d}t}$ reaches $0.0001\,^{\circ}\,\mathrm{ns}^{-1}$.

The behavior of single skyrmions/antiskyrmions could be very different from a lattice. Since the simulation goal is arrays of skyrmion and antiskyrmion tube lattices, at least several tens of skyrmions should be calculated to form a real lattice structure. So the in-plane size of the simulation must be large. Since we wish to simulate the thickness dependent behavior, the simulation in the thickness direction is also large. In order for the calculation to be carried out in a reasonable time without losing accuracy, the size of the minimum cell was increased compared to that used in the previous chapter. Simulation results of different cell sizes of 40 nm, 20 nm and 10 nm are shown in Fig. 5.6 . The exact details in the simulations show only small differences, but the main features stay the same.

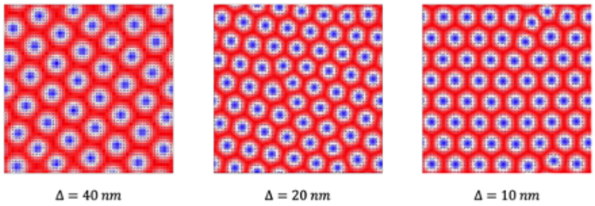

Figure 5.6: Simulation with different cell sizes. The parameters used are: 2000 nm×2000 nm×1 nm total size with $\Delta \times \Delta$×1 nm cell size, A =120 pJ m^{-1}, K_{eff} =0 MJ m^{-3}, M_s =445 kA m^{-1}, and H_z = 1800 Oe.

Some examples of simulation results are shown in Fig. 5.7-5.9. In Fig. 5.7, the magnetization structure for a calculation with 7 layers and B = 2000 Oe is shown. The color corresponds to the out-of-plane component of the magnetization, and the black arrows show the in-plane magnetization. Fig. 5.7a-c show layers 1, 4, and 7 of the simulation results for the B20 structure. A clear change of in-plane magnetization direction as a function of the thickness is shown. The thickness-averaged result is shown in Fig. 5.7d. A skyrmion lattice is stabilized, however the in-plane magnetization amplitude is reduced due to the twist along the thickness. Fig. 5.7e-h shows the corresponding magnetization structures for the D_{2d} case, where no twist is found along the thickness. The thickness averaged result is the same as any of the individual layers without any amplitude reduction.

Fig. 5.8 shows the calculation results of a 13 layer case under B = 2000 Oe. The magnetization maps for the B20 case corresponding to the 1, 4, 7, 10, and 13 layers are shown in Fig. 5.8a-e. Pronounced in-plane magnetization twist as a function of the thickness is shown. And some of the skyrmion tubes are broke in the middle. The thickness-averaged magnetization is shown in Fig. 5.8f. Much less contrast is shown because of the twist structure and a good skyrmion lattice no longer exists. Fig. 5.8g-l show the results for the D_{2d} case. There is no magnetization twist along the thickness. The thickness-averaged magnetization is the same as each layer without any reduction in the magnetization amplitude. And the antiskyrmion lattice clearly still exists.

In Fig. 5.9, we show the calculation results with 13 layers under B = 300 Oe. Fig. 5.9a-e show layer magnetizations for the 1, 4, 7, 10, and 13 layers of the B20 case. The helix struct is shown with a shift of position as

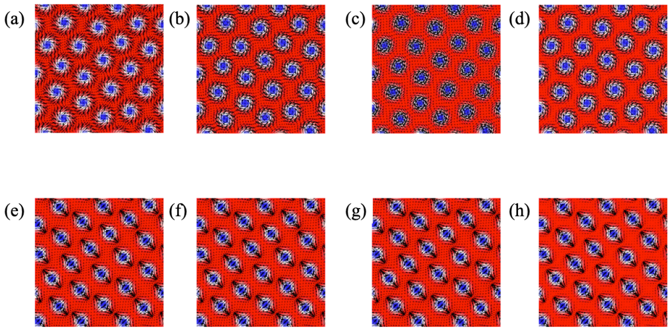

Figure 5.7: Simulations result of 7 layers with $B = 2000\,\mathrm{Oe}$. (a-d) Magnetization structure of layers 1, 4, and 7 and thickness-average result in a B20-type system. (e-h) Magnetization structure of layers 1, 4, 7 and thickness-average result for a D_{2d} system. A clear skyrmion/antiskyrmion lattice is stabilized in both systems. Color code indicates the out-of-plane component of the magnetization, and black arrows indicate the in-plane magnetization.

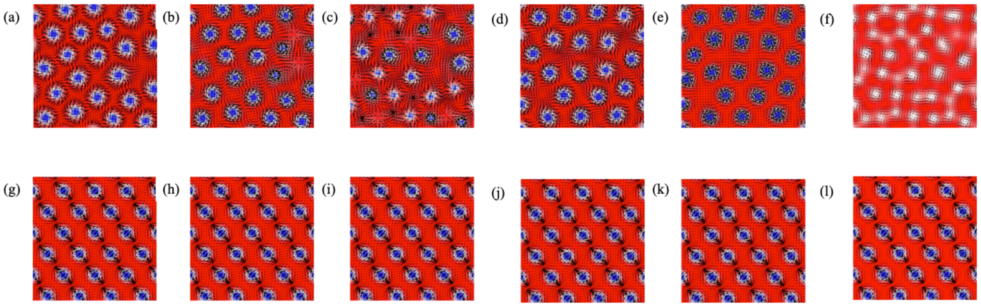

Figure 5.8: Simulations result of 13 layers with $B = 2000\,\mathrm{Oe}$. (a-f) Magnetization structure of layers 1, 4, 7, 10, and 13 and thickness-average result for a B20 type system. (g-l) Magnetization structure of layers 1, 4, 7, 10, and 13 and thickness-average result in a D_{2d} type system. The skyrmion lattice disappears in the B20 situation but still remain in the D_{2d} system. Color code indicates the out-of-plane component of the magnetization, and black arrows indicate the in-plane magnetization.

a function of thickness. The thickness-averaged magnetization of the B20 system is shown in Fig. 5.9f. There is very little contrast. Fig. 5.9g-l shows the results for the D_{2d} system, where no modulation is observed as a function of thickness. The thickness-averaged magnetization is the same as each layer without any reduction in the magnetization amplitude, where a clear helix structure is shown. These results are consistent with the DMI type that in this thickness direction a B20 material has a non-zero DMI component, whereas in the D_{2d} material it is rather zero.

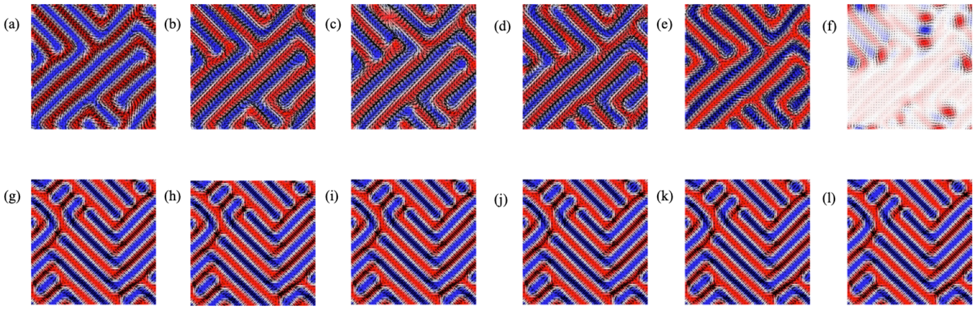

Figure 5.9: Simulations result of 13 layers with $B = 300\,\mathrm{Oe}$. (a-f) Magnetization structure of layers 1, 4, 7, 10, and 13 and thickness-average result for a B20-type system. (g-l) Magnetization structure of layers 1, 4, 7, 10, and 13 and thickness-average result for a D_{2d} system. Color code indicates the out-of-plane component of the magnetization, and black arrows indicate the in-plane magnetization.

In the above simulations, the antiskyrmion size and helix period do not change with thickness, which is different from our experiments. The size change is due to the dipolar interaction, which is not taken into consideration in the above simulation, which will be discussed in the next chapter.

The micromagnetic simulation results for various thicknesses and fields are summarized in Fig. 5.10, where the thickness-averaged out-of-plane magnetization is shown. The field range where skyrmions are stabilized in the B20 material decreases as the thickness increases. At a critical thickness, the skyrmion phase disappears, as reported previously [79, 35, 36, 78]. On the contrary, the antiskyrmion stable field range is insensitive to the thickness, which is in agreement with our LTEM results.

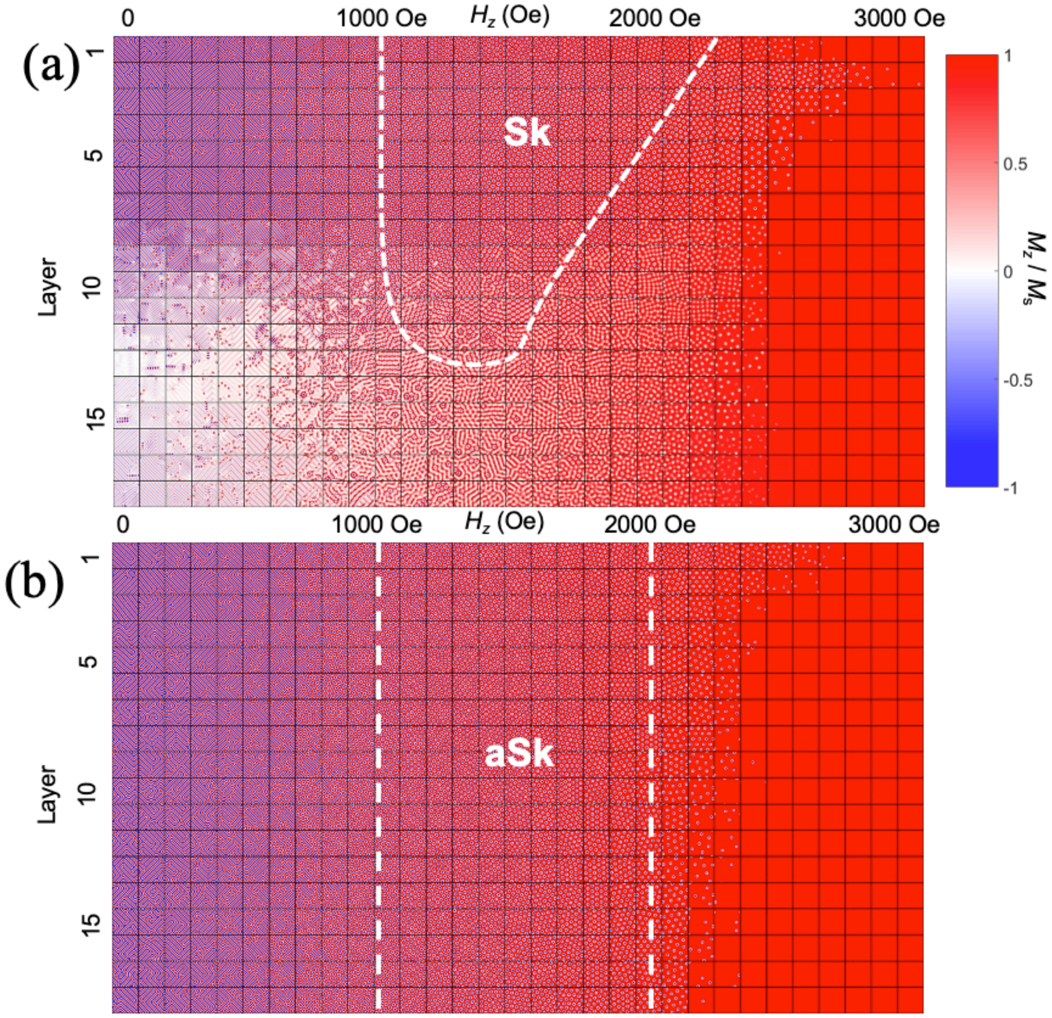

Figure 5.10: Summary of micromagnetic simulations result of the phase diagrams of B20 and D_{2d} systems. The simulation result is summarized into a table, where magnetic fields and thicknesses increase along the two axis direction. The thickness-averaged M_z is plotted, where the color indicates the normalized M_z regarding to the saturation magnetization M_s. Red/blue color corresponds to $M_z/M_s = +1/-1$. (a) In a B20-type material, the field region of the skyrmion shink as the thickness increases and finally disappears at acritical thickness. (b) In a D_{2d}-type material, the field region of the antiskyrmion phase is insensitive to the change in thickness.

5.4 Summary

LTEM experiments were performed to determine the thickness-dependent antiskyrmion phase diagram in a D_{2d} structure inverse tetragonal Heusler material. The field-temperature stability window of the antiskyrmion phase is found to be largely insensitive to the sample thickness in contrast to previous studies of the B20 system. Micromagnetic simulations were performed that reproduce our experiment results, from which we conclude that there are important differences in the phase stability of antiskyrmions and skyrmons that originates from the underlying symmetry of the DMI.

Chapter 6

Tunable magnetic antiskyrmion size and helical period from nanometers to microns in a D_{2d} Heusler compound

Following the studies of the thickness dependence of the stability of antiskyrmions as a function of temperature and field, we continue studies on the size of antiskyrmions. In several B20 materials, the dependence of the stability of skyrmions and helices on the host material thickness has been studied, including FeGe [30, 37], $Mn_{1-x}Fe_xGe$ of several compositions [31], and $Fe_{0.5}Co_{0.5}Si$ [82]. No significant thickness dependence of the helix period or the skyrmion size was found in these studies. The characteristic length scale is concluded to be determined by a competition between the Heisenberg exchange and the DMI energy term. On the contrary, in early studies of the size and behavior of achiral magnetic bubbles, they are shown to be strongly influenced by magnetic dipolar interactions [83, 84, 85]. Some types of skyrmions termed "bi-skyrmions" and "skyrmions" in centrosymmetric materials belong to this latter category [39, 86, 87].

In this chapter, we show the uniqueness of antiskyrmion systems in which both long-range magnetic dipolar interactions as well as the DMI energy term play a significant role. Due to their influence, the antiskyrmion system enjoys a wide range of size tunability as well as an intrinsic stability. By performing LTEM and MFM experiments, we find the helical period and the size of the antiskyrmion correspond to one another and both of them can be tuned by up to one order of magnitude when the host material thickness is varied. This size tunability is accounted for by an analytic model.

In this work [88] the LTEM measurements were performed by Rana Saha, FIB lamellae preparation was carried out by Abhay K. Srivastava and MFM measurements were performed by Ankit K. Sharma. I was involved in the experiment design and discussion, programed the LTEM and MFM image analysis software, and contributed to the theory part of this work.

The figures used in this chapter are reprinted from [88], for which I am one of the authors. (Reprinted from [88]. Link to the Creative Commons license: https://creativecommons.org/licenses/by/4.0/)

6.1 LTEM measurement

From a single crystal of $\mathrm{Mn_{1.4}PtSn}$, a uniform thickness lamella (L1), and several wedge-shaped lamellae (L2-L4) were prepared by FIB.

Fig. 6.1a shows a schematic drawing of the antiskyrmion magnetization structure. Bloch-like helicoids and Néel-like cycloidal magnetization structures are formed around the complex boundary of an antiskyrmion. Along the [110] and $[1\bar{1}0]$ directions, are Néel domain walls with opposite chirality, and along the [100] and [010] directions, are Bloch domain walls with opposite chirality. Without applying an in-plane magnetic field, the helix will propagate along these Bloch type directions in the D_{2d} system. The reason is that the dipolar energy is lower for the Bloch type walls, as will be explained in a later section.

It is found that the size of the spin textures in $\mathrm{Mn_{1.4}PtSn}$ varies only a little when changing the temperature, so we focused on room temperature studies. A magnified LTEM image of a single antiskyrmion in L1 is shown in Fig. 6.1b. It has the unique four-spot pattern with alternating black and white contrast, which is the same as in $\mathrm{Mn_{1.4}Pt_{0.9}Pd_{0.1}Sn}$ [73]. Thus, it confirms the stabilization of antiskyrmions in $\mathrm{Mn_{1.4}PtSn}$. Fig. 6.1c shows a SEM image of the wedge shape of L2. And Fig. 6.1d shows a schematic diagram to define the coordinate axis and tilting angles. Fig. 6.1e shows a LTEM measurement result at zero magnetic field. Importantly, it is found that the helix period changes significantly as a function of the thickness of the lamella. In the LTEM image, two representative regions A and B are magnified as shown in Fig. 6.1 h-i. Region A and B are both 1 µm × 1 µm in area, and the thicknesses of A is ~142 nm and B is ~206 nm. From region A to B, the helix period changes from ~108 ± 13nm (Fig. 6.1h) to ~185 ± 2nm (Fig. 6.1i).

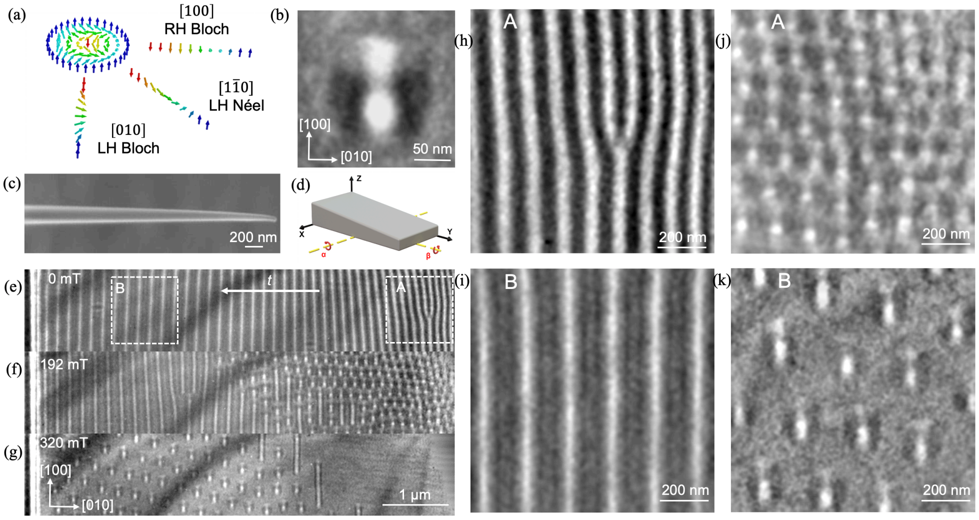
(a)
[100]
RH Bloch
[1$\bar{1}$0]
LH Néel
[010]
LH Bloch
(b)
[100]
[010]
50 nm
(c)
200 nm
(d)
z
x
Y
α
β
(e)
0 mT
B
t
A
(f)
192 mT
(g)
320 mT
[100]
[010]
1 μm
(h)
A
200 nm
(i)
B
200 nm
(j)
A
200 nm
(k)
B
200 nm

Figure 6.1: LTEM images of $Mn_{1.4}PtSn$. (a) Antiskyrmion magnetization structure and its chirality along different directions. (b) LTEM image of a single antiskyrmion in L1. (c) SEM image of lamella L2, viewed from an angle of 35° from the X axis in the XY plane. (d) Definition of coordinate axis and tilt angles α and β. (e-g) LTEM images of L2 under fields of 0, 192 and 320 mT. (h-i) Magnified LTEM image of the helix structure of regions A and B in (e). (j-k) Magnified LTEM image of the antiskyrmion structure of regions A and B in (f-g).

By applying a perpendicular field, the helical state changes into an antiskyrmion state. Fig. 6.1f-g shows typical LTEM results under fields of 192 mT and 320 mT . It is clear that the antiskyrmion size, similar to the helix period, also has a strong thickness dependence. To make this comparison clearer, Fig. 6.1j shows the LTEM image of region A under 192 mT and Fig. 6.1k shows the LTEM image of region B under 320 mT. Clearly, the antiskyrmion size is changed from ~128 ± 5nm to ~200 ± 4nm.

6.2 MFM measurement

To explore larger lamella thicknesses, the MFM technique (in which the contrast corresponds to the stray field produced mainly by the out of plane magnetization component, M_z) is used for two wedged lamellae L3 (from ~630 to ~4260nm) and L4 (~60 to ~1600nm). Fig. 6.2a shows the SEM image of the wedge-shaped L3. The inset shows the definition of the coordinate axis and the field angle φ_H which is in-plane. First, a field of 1 T is applied at φ_H which saturates the magnetization. And then the field is reduced to zero before taking the MFM image. The helix direction is found to be dependent on φ_H. Shown in Fig. 6.2, when $\varphi_H = 180°$, the helix propagates mostly along [100]. When the field is applied along $\varphi_H = 90°$, shown in Fig. 6.2c, the helix propagation direction changes to be mostly along [010]. When $\varphi_H = 135°$, as shown in Fig. 6.2d, a mixture of both helix propagation directions is shown.

Fig. 6.2e shows a line profile taken from Fig. 6.2c. Fig. 6.2f shows a helical region of a MFM result in L4 in a 3D colormap. Both these two figures show a clear sinusoidal MFM signal of M_z along the direction of the wedge. There is also a monotonic increase in the helix period and amplitude when the lamella thickness increases. The resulting analysis of the helical period as a function of thickness in these measurements is summarized in Fig. 6.2g. The results from the LTEM and MFM measurements show good agreement with one another. The inset in Fig. 6.2g shows the LTEM measured helical period as a function of thickness from wedge L2 compared to results in the sister compound $Mn_{1.4}Pt_{0.9}Pd_{0.1}Sn$ [73]. The results are similar in both compounds.

When applying a magnetic field, the helical phase will start to change into an antiskyrmion phase, as shown in Fig. 6.3. Typical MFM results under fields of 300, 420 and 480mT applied at an angle of 30° from the z-axis to the [010] direction are shown in Fig. 6.5a-d. A gradual field dependent transformation from the helical phase into an antiskyrmion phase and finally into the ferromagnetic phase is shown, where the influence of the thickness is clear. The critical transformation fields largely depend on the in-plane field component. With the tilt field angle of ~30°, antiskyrmions can be stabilized over a large thickness range at the same time. A similar tilting angle is also used in the LTEM measurements. When the field is increased to ~550mT, the whole sample area becomes fully polarized.

The antiskyrmion phase is found to be stable for all thicknesses, which

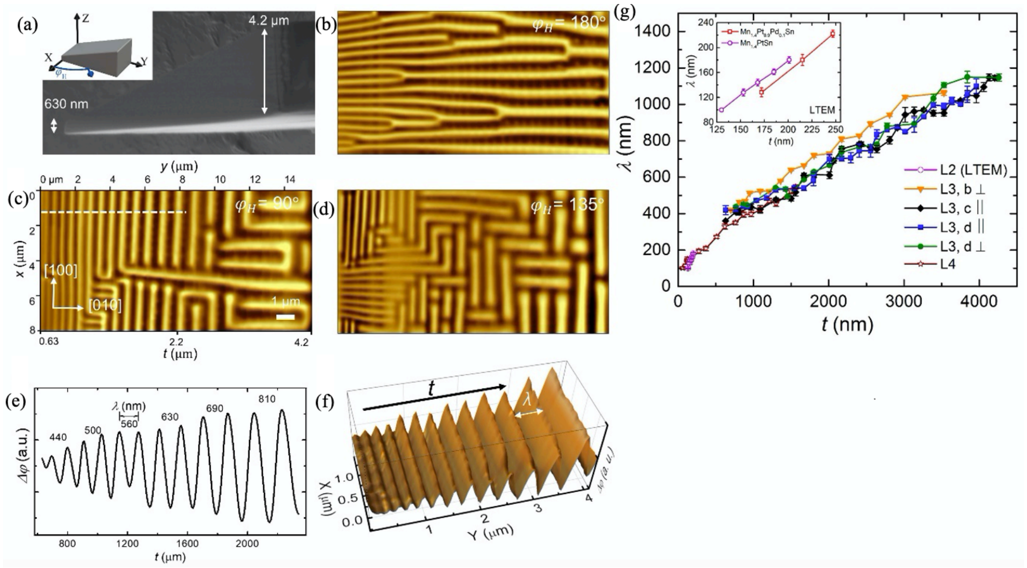

Figure 6.2: MFM images of the helical magnetization structure in $Mn_{1.4}PtSn$. (a) SEM image of L3. Inset defines the angle φ_H in-plane. (b-d) MFM measurement results under different φ_H. The MFM measurement area is $8 \times 16 \mu m^2$. From left to right, the thickness increases. (e) Line profile of MFM result, $\Delta\varphi$, taken from the white dashed line in (c). (f) 3D colormap of MFM result, $\Delta\varphi$ for the wedge L4. (g) Summary of the analyzed thickness dependent helix period. Inset shows the helix period comparison of two sister materials, measured by LTEM.

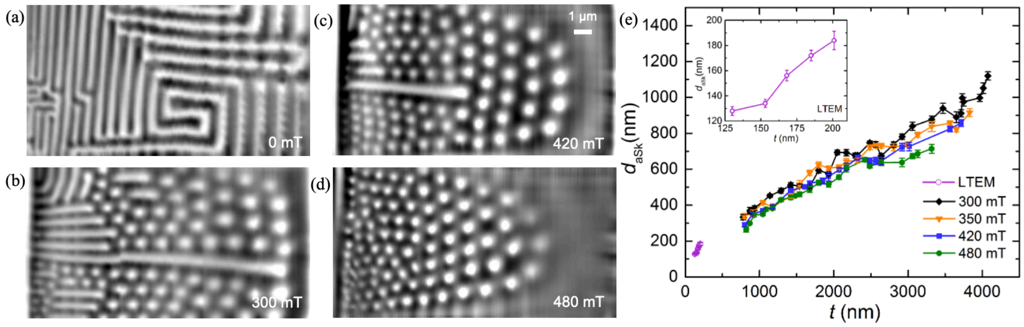

Figure 6.3: MFM measurements of the antiskyrmion phase. (a) At zero field, only the helical phase is seen. (b-d) at the field of 300 mT, (c) 420 mT and (d) 480 mT, the antiskyrmion phase starts to appear. (e) Summary of the analyzed antiskyrmion size as a function of thickness under different magnetic fields in L4. Inset shows the thickness dependence of the antiskyrmion size measured by LTEM in L2.

enabled us to determine the antiskyrmion size as a function of lamella thickness. Analysis of these results is shown in Fig. 6.3e. The protocol used to determine the antiskyrmion size is described below. Firstly, load the image into an image analysis program. The antiskyrmions are obtained manually by clicking the mouse in the center and at the boundary of each of the antiskyrmions. Typical results are shown in Fig. 6.6, where the red circles show the antiskyrmions. From the MFM images we can determine the position of each antiskyrmion. The wedge-shaped sample was analyzed from the AFM data and shown to have a linear dependence of thickness with position. Thus the position of the antiskyrmion is used to determine the thickness at the center of the antiskyrmion. The standard deviation in the sizes of antiskyrmions measured at a similar thickness is shown as the error bar in the figure.

The analyzed results demonstrate clearly that field does not much influence the antiskyrmion size. However, the thickness's influence is, by contrast, very strong. When the thickness changes from 142 nm to 4.2 µm, the antiskyrmion size changes by one order of magnitude from ~142 nm to nearly 1.2 µm. It was also found that the size of the antiskyrmion and the period of the helix are very similar, as shown in Fig. 6.5.

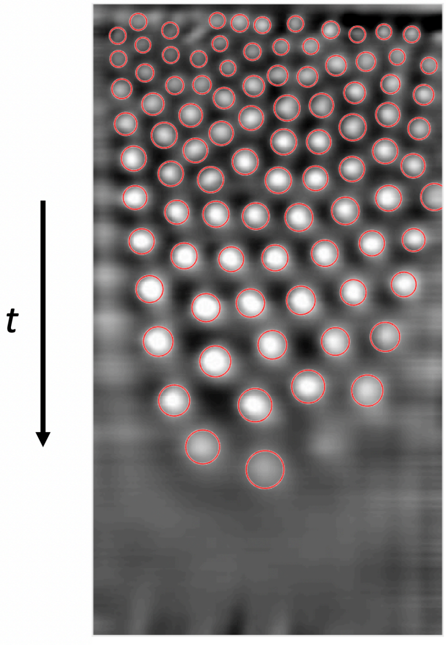

Figure 6.4: Antiskyrmion size analysis. A typical analyzed MFM image of the antiskyrmion phase under 480 mT of the lamella L3. The size and position of each antiskyrmion is shown by the red circles.

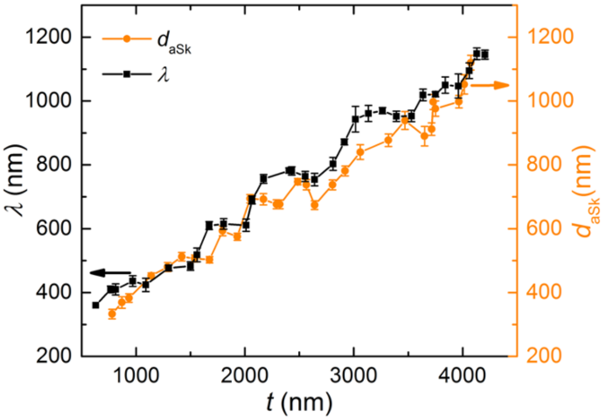

Figure 6.5: Comparison of helical period and antiskyrmion size in L3. The helical period is plotted in black symbols and line and the antiskyrmion size is plotted in orange symbols and line.

6.3 Model and calculation

In order to understand the physical mechanism of the thickness dependent behavior of the helix period and the antiskyrmion size, we developed an analytic model of the D_{2d} system.

I assume that the helix has a magnetization structure that only changes in the direction of the helix. It changes in a Bloch fashion following a sine function whose period is λ. The model assumes an infinite size in the XY plane and a thickness of t in the z direction. In a D_{2d} system, since there is no component of the DMI vector along the z-direction (which is the [001] crystal direction), it is reasonable to assume the magnetization doesn't change along z. In the B20 system, since there the DMI vector has a component in three dimensions, such an assumption is not valid.

6.3.1 E_{Dip} for a Bloch helix

The magnetization $\overrightarrow{M} = (M_x, M_y, M_z)$ is expressed as:

$$\begin{cases} M_x(x,y,z) = 0 \\ M_y(x,y,z) = M_s \sin(\frac{2\pi x}{\lambda}) \\ M_z(x,y,z) = M_s \cos(\frac{2\pi x}{\lambda}) \end{cases} \qquad \text{for} \quad -\frac{L_z}{2} < z < \frac{L_z}{2} \tag{6.1}$$

$$\begin{cases} M_x(x,y,z) = 0 \\ M_y(x,y,z) = 0 \\ M_z(x,y,z) = 0 \end{cases} \qquad \text{for} \quad z < -\frac{L_z}{2} \quad \text{or} \quad z > \frac{L_z}{2} \tag{6.2}$$

The magneto-dipolar energy per volume E_{Dip} is calculated from:

$$E_{Dip} = -\frac{\mu_0}{2V} \int \overrightarrow{M} \cdot \overrightarrow{H} \, \mathrm{d}\tau \tag{6.3}$$

where V is the volume of the sample.

We first need to calculate the field

$$\overrightarrow{H} = -\nabla U \tag{6.4}$$

where U is a scalar potential. U should satisfy the following equations [89]:

$$\nabla^2 U_{in} = \overrightarrow{\nabla} \cdot \overrightarrow{M} \qquad \text{inside the sample} \tag{6.5}$$

$$\nabla^2 U_{out} = 0 \qquad \text{outside the sample} \tag{6.6}$$

$$U_{in} = U_{out} \qquad \text{on the surface} \tag{6.7}$$

$$\frac{\partial U_{in}}{\partial n} - \frac{\partial U_{out}}{\partial n} = \overrightarrow{M} \cdot \overrightarrow{n} \qquad \text{on the surface, where } \overrightarrow{n} \text{ is the unit vector normal to the surface} \tag{6.8}$$

U can be calculated from the magnetization [89]:

$$U\left(\overrightarrow{r}\right) = \frac{1}{4\pi}\left[-\int \frac{\overrightarrow{\nabla'} \cdot \overrightarrow{M(\overrightarrow{r'})}}{|\overrightarrow{r} - \overrightarrow{r'}|} \mathrm{d}\tau' + \int \frac{\overrightarrow{n} \cdot \overrightarrow{M(\overrightarrow{r'})}}{|\overrightarrow{r} - \overrightarrow{r'}|}\right] \tag{6.9}$$

where $\overrightarrow{\nabla'}$ contains derivatives with respect $\overrightarrow{r'}$.

From Equ. (6.1-6.2) and Equ. (6.9), we can get:

$$U(x,y,z) = \frac{M_s \lambda}{4\pi} \cos\left(\frac{2\pi x}{\lambda}\right)\left(e^{-\frac{2\pi}{\lambda}|z-\frac{L_z}{2}|} - e^{-\frac{2\pi}{\lambda}|z+\frac{L_z}{2}|}\right) \tag{6.10}$$

It can be readily checked that Equ. (6.10) and Equ. (6.5-6.8) are consistent with each other.

Then the field is found:

$$\begin{aligned}\overrightarrow{H} &= -\nabla U \\ &= \left(\frac{M_s}{2}\sin\left(\frac{2\pi x}{\lambda}\right)\left[e^{-\frac{2\pi}{\lambda}\left(\frac{L_z}{2}-z\right)} - e^{-\frac{2\pi}{\lambda}\left(z+\frac{L_z}{2}\right)}\right] \quad 0 \quad -\frac{M_s}{2}\cos\left(\frac{2\pi x}{\lambda}\right)\left[e^{-\frac{2\pi}{\lambda}\left(\frac{L_z}{2}-z\right)} - e^{-\frac{2\pi}{\lambda}\left(z+\frac{L_z}{2}\right)}\right]\right)\end{aligned} \tag{6.11}$$

Based on Equ. (6.1-6.2, 6.11) and Equ. (6.3), we can calculate the final result:

$$E_{Dip} = \frac{\mu_0 M_s^2 \lambda}{8\pi L_z}\left(1 - e^{-\frac{2\pi L_z}{\lambda}}\right) \tag{6.12}$$

6.3.2 Numerical confirmation of the E_{Dip}

Numerical calculations are performed to check the validity of Equ. (6.12). The dipolar energy between two atoms is given by:

$$E_{Dip,ab} = \frac{\mu_0}{4\pi} \frac{\overrightarrow{S_a} \cdot \overrightarrow{S_b} |\overrightarrow{P_a} - \overrightarrow{P_b}|^2 - 3\overrightarrow{S_a} \cdot \left(\overrightarrow{P_a} - \overrightarrow{P_b}\right) \cdot \overrightarrow{S_b} \cdot \left(\overrightarrow{P_a} - \overrightarrow{P_b}\right)}{|\overrightarrow{P_a} - \overrightarrow{P_b}|^5} \tag{6.13}$$

where $\overrightarrow{P_a}$ and $\overrightarrow{P_b}$ are the atom positions and $\overrightarrow{S_a}$ and $\overrightarrow{S_b}$ are the magnetic moments of these atoms.

Summing up over the pairs of atoms within the sample, the total dipolar energy can be calculated. This numerical method was used in my previous work [23, 24] with modifications for the 3D case. In Fig. 6.6a, the numerical calculation and the analytical formula are found to be match nicely. Simply due to the different choice of zero-energy, there is a non-important constant energy difference ($\frac{\mu_0 M_s^2}{6}$) between the numerical and analytical mehods. Tiny differences appear, as displayed in Fig. 6.6b-c, when the thickness or the period of the helix is very small. Such differences come from the assumption of a continuous change of magnetization that is not satisfied in the analytical method [89]. This parameter range is, however, not relevant to the experimental situation.

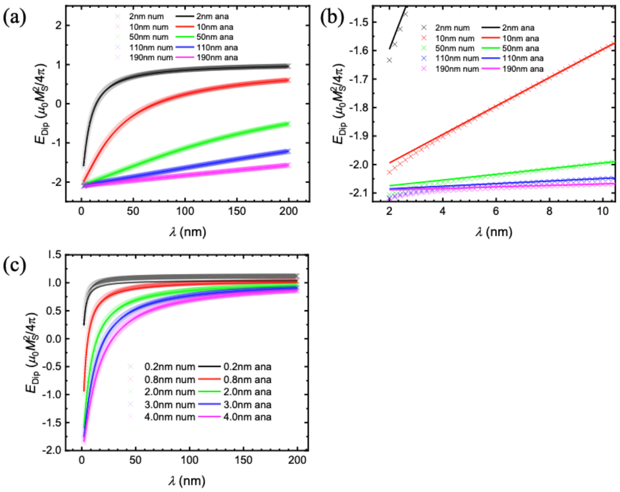

Figure 6.6: Comparison of numerical and analytical results. (a) Nice agreement is found. At (b) tiny helix periods or (c) tiny thicknesses, small differences are found.

6.3.3 E_{Dip} for other types of helices, cycloids or in-between geometries

The situation of other types of structure: Néel cycloid, or in-between state is calculated.

The magnetization $\overrightarrow{M} = (M_x, M_y, M_z)$ can be expressed by:

$$\begin{cases} M_x(x,y,z) = M_s \sin(\frac{2\pi x}{\lambda}) \sin(\varphi_0) \\ M_y(x,y,z) = M_s \sin(\frac{2\pi x}{\lambda}) \cos(\varphi_0) \\ M_z(x,y,z) = M_s \cos(\frac{2\pi x}{\lambda}) \end{cases} \quad \text{for} \quad -\frac{L_z}{2} < z < \frac{L_z}{2} \tag{6.14}$$

$$\begin{cases} M_x(x,y,z) = 0 \\ M_y(x,y,z) = 0 \\ M_z(x,y,z) = 0 \end{cases} \quad \text{for} \quad z < -\frac{L_z}{2} \quad \text{or} \quad z > \frac{L_z}{2} \tag{6.15}$$

When $\varphi_0 = 0, \pi$ a Bloch Helix structure propagates in the D_{2d} [100]/[010] directions; When $\varphi_0 = \frac{\pi}{2}, \frac{3\pi}{2}$ a Néel cycloid propagates in the [110]/[1$\bar{1}$0] directions; Other φ_0 values correspond to directions in between.

U can be calculated in a similar way as discussed in the last section. From Equ. (6.9), we find that:

$$U(x,y,z) =$$
$$\begin{cases} U_1 = \dfrac{1}{4\pi}\lambda M_s \cos\left(\dfrac{2\pi x}{\lambda}\right) e^{-\frac{2\pi}{\lambda}z}\left(e^{\frac{\pi}{\lambda}L_z} - e^{-\frac{\pi}{\lambda}L_z}\right)(1-\sin\varphi_0) & z > \dfrac{L_z}{2} \\ U_2 = \dfrac{\lambda M_s}{4\pi}\cos\left(\dfrac{2\pi x}{\lambda}\right)\left[-2\sin(\varphi_0) + \sin(\varphi_0) e^{-\frac{\pi}{\lambda}L_z}\left(e^{\frac{2\pi}{\lambda}z} + e^{-\frac{2\pi}{\lambda}z}\right) + e^{-\frac{\pi}{\lambda}L_z}\left(e^{\frac{2\pi}{\lambda}z} - e^{-\frac{2\pi}{\lambda}z}\right)\right] & \\ & -\dfrac{L_z}{2} < z < \dfrac{L_z}{2} \\ U_3 = \dfrac{1}{4\pi}\lambda M_s \cos\left(\dfrac{2\pi x}{\lambda}\right) e^{\frac{2\pi}{\lambda}z}\left(e^{-\frac{\pi}{\lambda}L_z} - e^{\frac{\pi}{\lambda}L_z}\right)(1+\sin\varphi_0) & z < -\dfrac{L_z}{2} \end{cases} \tag{6.16}$$

In the calculation, the following equation is used:

$$\int_0^{+\infty} \frac{\cos(x)}{\sqrt{x^2+A}}\,\mathrm{d}x = K_0\left(\sqrt{A}\right) \tag{6.17}$$

where $K_0(x)$ is the zero order modified Bessel function of the second kind.

$$\int_0^{+\infty} K_0\left(|a|\sqrt{x^2+b^2}\right)\mathrm{d}x = \frac{\pi}{2|a|}e^{-|a||b|} \tag{6.18}$$

Equ. (6.16) agrees with Equ. (6.5-6.8), thereby confirming its correctness.

Based on $\overrightarrow{H} = -\nabla U$, the field and dipolar energy density can be calculated:

$$E_{Dip} = \frac{\mu_0 M_s^2 \sin^2(\varphi_0)}{4} + \frac{\mu_0 M_s^2}{8L_z}\frac{\lambda}{\pi}\left(1 - e^{-\frac{2\pi}{\lambda}L_z}\right)\left(1 - \sin^2\varphi_0\right) \tag{6.19}$$

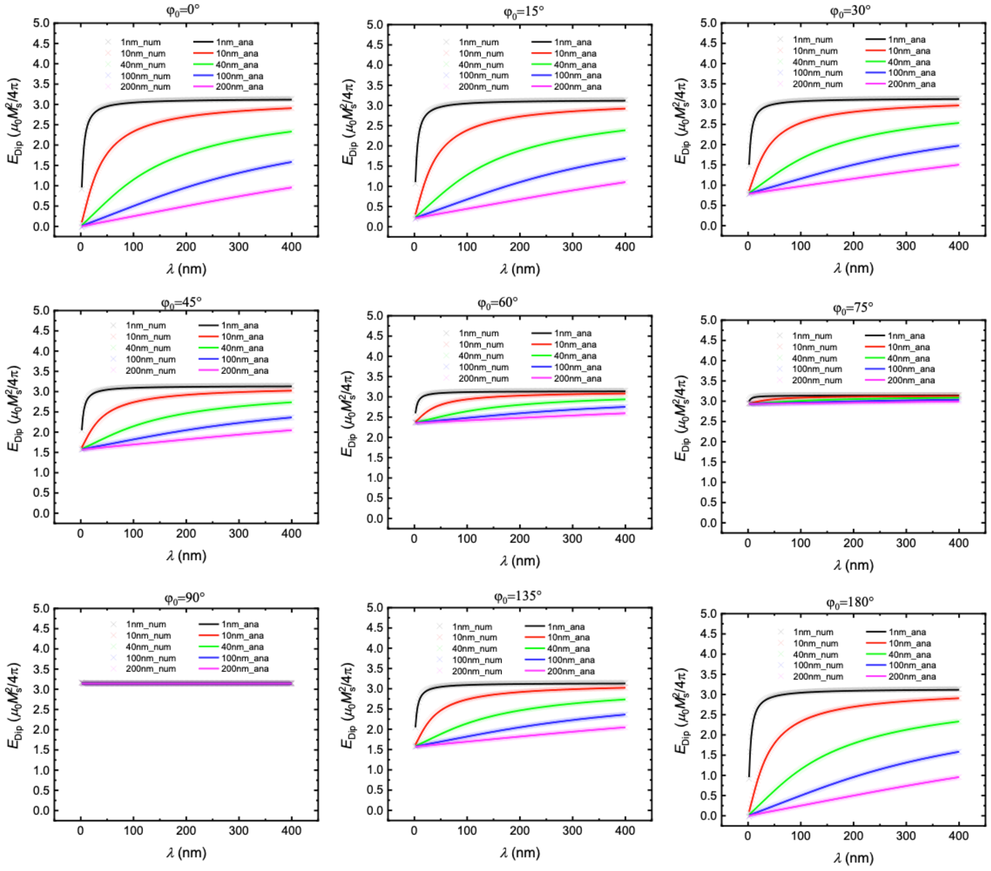

Figure 6.7: Comparison of numerical calculations with an analytical formula for various φ_0 that correspond to distinct spin textures.

I also use numerical calculations to double check the validity of Equ. (6.19), as shown in Fig. 6.7.

We now compare the energy difference for other structures compared to a Bloch geometry. The energy difference is:

$$\Delta E_{Dip} = E_{Dip,Bloch} - E_{Dip,Other} = \frac{\sin^2 \varphi_0 \mu_0 M_s^2}{4} \left[\frac{\lambda}{2\pi L_z} \left(1 - e^{-\frac{2\pi L_z}{\lambda}} \right) - 1 \right] \tag{6.20}$$

We define $x = \frac{2\pi L_z}{\lambda}$, due to the positive value of L_z and λ, $x > 0$. Thus,

$$\Delta E_{Dip} = \frac{\sin^2 \varphi_0 \mu_0 M_s^2}{4} \left(\frac{1 - e^{-x}}{x} - 1 \right) \leq 0 \tag{6.21}$$

Equ. (6.21) shows that, compared to other magnetic geometries, a Bloch helix magnetic structure will always have the lowest dipolar energy. This conclusion holds, regardless of the thickness and helix period. This explains the experimental result that, when no external field is applied, the helix in a D_{2d} system will always prefer a Bloch geometry, which is locked to the [100]/[010] directions.

6.3.4 Finite size effect of the dipolar interaction

In the calculations of the previous few sections, the sample was considered to have an infinite size in the in-plane directions. The real sample being measured in the experiments, however, is limited in size. For example, lamella L1-4 prepared by FIB used in this work, have an in-plane size of a few micrometres. To check the finite size's influence, some calculations were performed, where two methods are used.

In the first method, I use Equ. 6.13 with a finite size in the direction of X. In the second method, I use micromagnetic simulations: the fixed helix structure is used as input, and the internal energy calculator of OOMMF is used to calculate the dipolar energy [59] . The results of the calculation are shown in Fig. 6.8, where a nice agreement is found. An additional feature of a thickness dependence oscillation is shown. This oscillation's period and amplitude increase together with the period of the helix structure.

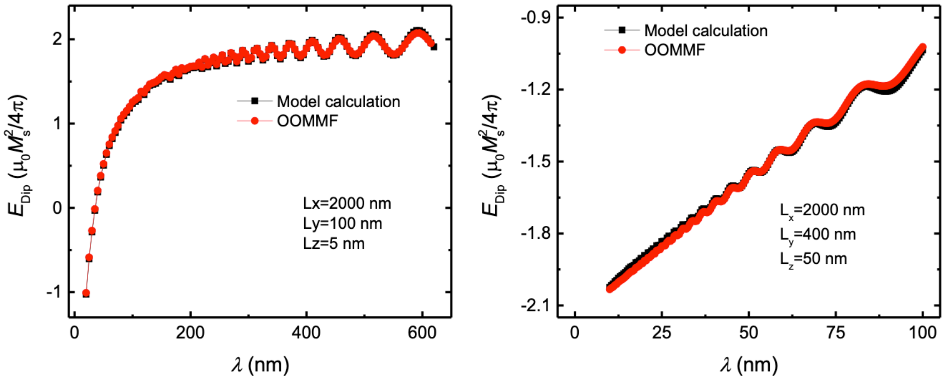

Figure 6.8: Model and OOMMF calculation of E_{Dip} as a function of λ. The size of the sample is: (a) L_x =2000 nm, L_y =100 nm and L_z =5 nm (b) L_x =2000 nm, L_y =400 nm and L_z =50 nm.

6.3.5 Position dependence of the magnetic dipolar energy density

The averaged dipolar energy density is discussed in section 6.3.1. From the model calculation the dipolar energy density has the following expression:

$$E_{Dip,density}(x,y,z) = \frac{\mu_0 M_s^2}{4} \cos^2\left(\frac{2\pi x}{\lambda}\right)\left[e^{-\frac{2\pi}{\lambda}\left(\frac{L_z}{2}-z\right)} + e^{-\frac{2\pi}{\lambda}\left(z+\frac{L_z}{2}\right)}\right] \quad (6.22)$$

Here, we plot the energy density as a function of position in the XZ cross-section plane. This will be helpful in understanding the dipolar energy as a function of thickness.

Dipolar energy density in a sample with a thickness of 200 nm is shown in Fig. 6.9 . The helix period changes from 50 nm to 600 nm, as shown in Fig. 6.9 a-l. Whereas in Fig. 6.10 the helix period is fixed at 500 nm. The thickness changes from 100 nm to 650 nm, as shown in Fig. 6.10a-l. From the expression of Equ. (6.22), the dipolar energy density is composed of a $\cos^2\left(\frac{2\pi x}{\lambda}\right)$ changing along the x direction and along the z direction two exponentially decaying terms where the characteristic length is λ . Under the situation that λ is much smaller compared to t, the dipolar energy is mostly pronounced at the surfaces and decays rapidly to the middle of the layer's thickness. As λ is increased at a constant thickness of 200 nm (Fig. 6.9) the dipole energy density increases at the surfaces of the slab. As the thickness of the slab is decreased for a constant λ of 500 nm (Fig. 6.10) the dipole energy density increases at the surfaces and finally for thin layers in the middle of the slab. The dipolar energy density decreases when λ becomes smaller and/or the thickness becomes larger. This is due to the magnetic structure with less twist will increase the so called ‘magnetic charge’ accumulated .

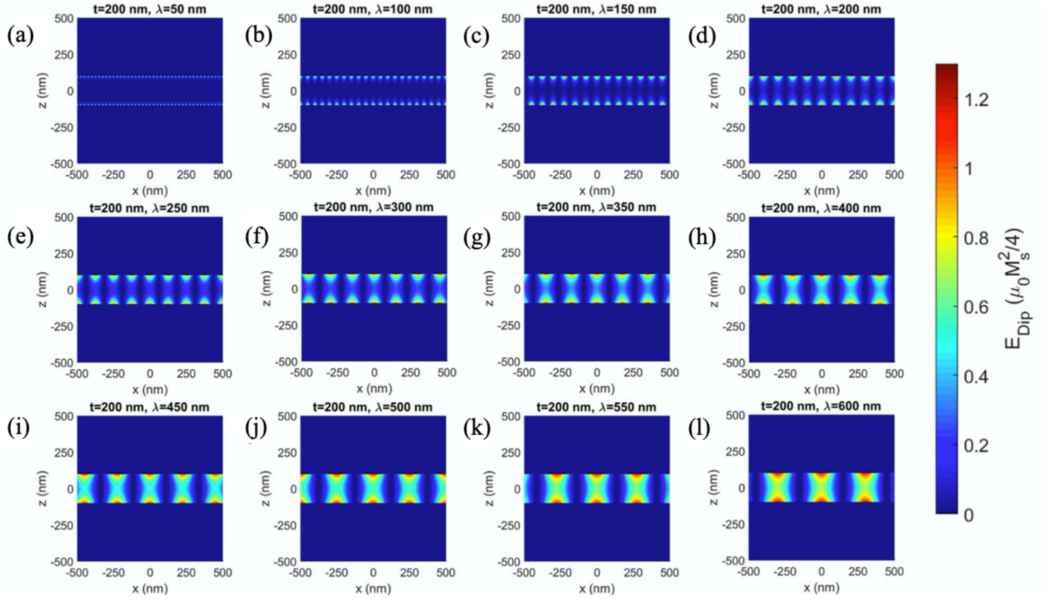

Figure 6.9: Position dependent dipolar energy density t =200 nm. (a-l) λ changes from 50 nm to 600 nm.

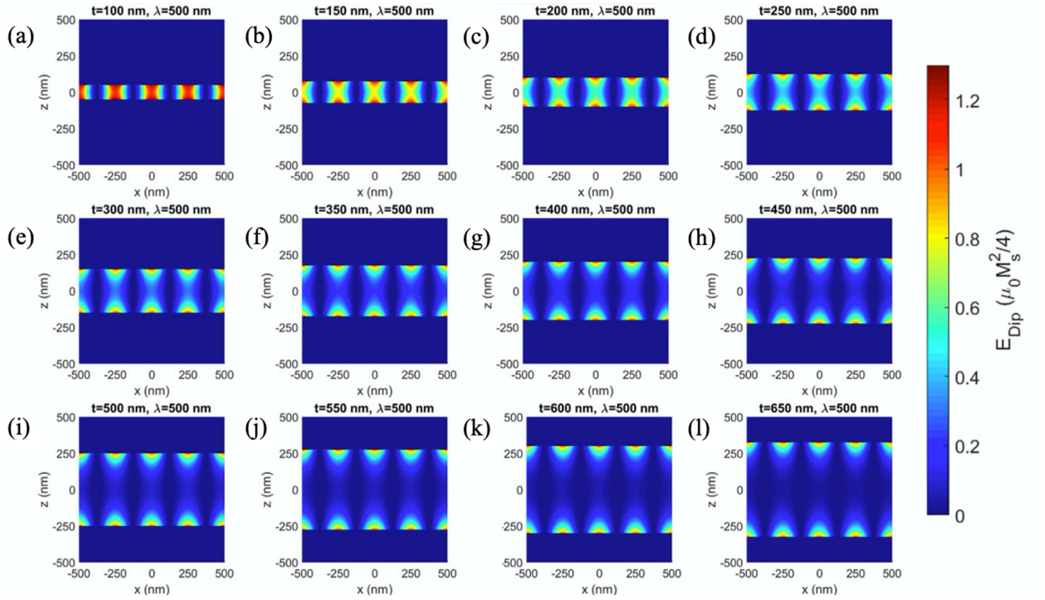

Figure 6.10: Position dependent dipolar energy density for λ =500 nm. (a-l) t changes from 100 nm to 650 nm.

6.3.6 Helix wavelength calculation

After the above model preparation, we now calculate the helix wavelength. The total energy density is described by:

$$E_{Tot} = E_{Exc} + E_{DMI} + E_{Ani} + E_{Dip} = \frac{4\pi^2 A}{\lambda^2} - \frac{2\pi|D|}{\lambda} + \frac{K}{2} + \frac{\mu_0 M_s^2 \lambda}{8\pi t}\left(1 - e^{-\frac{2\pi t}{\lambda}}\right) \tag{6.23}$$

where A is the exchange stiffness in $[\mathrm{J\,m^{-1}}]$, K is the anisotropy energy in $[\mathrm{J\,m^{-3}}]$, E_{Exc} is the exchange energy density in $[\mathrm{J\,m^{-3}}]$, E_{DMI} is the DMI energy density, E_{Ani} is the magnetic anisotropy energy density, E_{Dip} is the magnetic dipolar energy density and E_{Tot} is the total energy density. Since the exchange interaction, DMI, and anisotropy of this system all originate from the bulk, there are no pre-factors regarding the thickness in the energy terms.

The magnetic geometry is shown in Fig. 6.11a. The dipolar energy density for various t with respect to the helix period are shown in Fig. 6.11b. At very small film thicknesses ($t \ll \lambda$), E_{Dip} can be approximated by $E_{Dip} = \frac{\mu_0 M_s^2}{4}\left(1 - \frac{\pi t}{\lambda}\right)$, which changes very little within this thickness range. At large film thickness ($t \gg \lambda$), E_{Dip} is approximated to $E_{Dip} = \frac{\mu_0 M_s^2 \lambda}{8\pi t}$, which shows a linear relationship with λ and the slope is very small. Under these two extreme situations, as shown in Fig. 6.11b for t =1 nm and t =2500 nm, the dipolar energy does not depend on λ much. On the contrary, for the intermediate thickness range (e.g. t =200 nm), the λ dependent E_{Dip} will changes on the order of $\frac{\mu_0 M_s^2}{4}$ within the parameter range of interest.

The helix period corresponds to the value that gives the lowest energy of E_{Tot}. The calculation results are shown in Fig. 6.11c-d for different parameters. In Fig. 6.11c, the A and M_s are set to a constant value, and the thickness and DMI strength are varied. In Fig. 6.11d, A and D are fixed, and the thickness and M_s are varied. When the DMI is very strong, shown in Fig. 6.11c, λ has the value of $\frac{4\pi A}{|D|}$. When the DMI strength becomes weaker, λ drops first at small t then slowly increases to $\frac{4\pi A}{|D|}$ when t is large. When M_s is becoming larger, as shown in Fig. 6.11d, λ becomes smaller.

The dipole energy density is mostly around the surfaces of the lamella except when t is very small. E_{Dip} has the largest value at the surfaces, then decays exponentially towards the middle of the lamella with a characteristic length related λ. So, at large t, the helix wavelength is not much influenced by the magnetic dipolar interaction, and is mostly determined by the ratio of the Heisenberg and DMI energy terms. However, for the thickness range studied here the dipole energy will influence λ a lot. This is due to the fact that the twist of the helical structure will reduce the 'magnetic charge' at the surfaces. In this range, due to the fact that the total dipolar energy density decreases according to the form $\sim\frac{1}{t}$, the resulting λ will monotonically increase as the thickness is increased. This is the origin of the experimental observation that λ increases linearly as a function of thickness. This model nicely agrees with the observed trend of the increase in λ with increasing thickness, but an exact agreement is difficult to find. These deviations could originate from the assumed pure helical Bloch-type structure that is a constant along the thickness. MFM measurements show that the helix contrast is almost sinusoidal. The MFM signal amplitude also increases linearly as a function of thickness. However, the actual magnetic structure could be more complex than our simple assumption.

The calculation of the magneto-dipolar energy density for the antiskyrmion lattice structure is much more complicated. But the experimental results show that the helix period and antiskyrmion size are very similar to one other. So it is reasonable to make the assumption that the same mechanism,

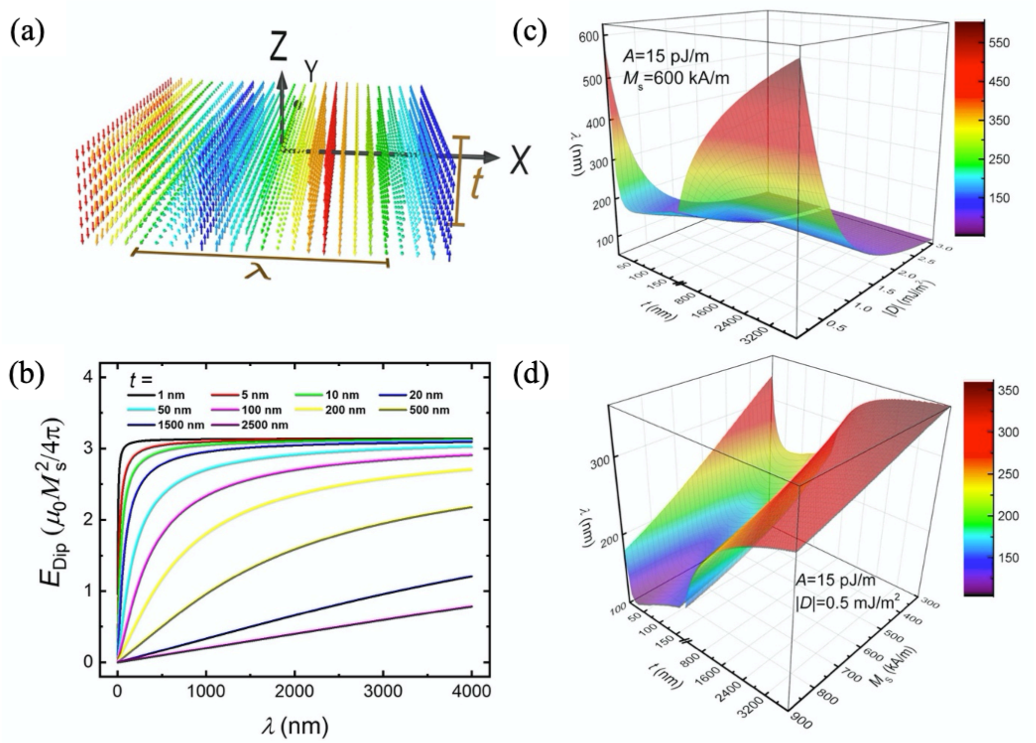

Figure 6.11: Calculation of helix period in D_{2d} system as a function of thickness. (a) Schematic diagram of the helical magnetization structure. (b) Magneto-dipolar energy density as a function of λ at different t. (c) Calculated λ as a function of t and DMI strength. (d) Calculated λ as a function of t and M_s.

which is the thickness dependence of the dipolar energy density, also leads to the size variation of the antiskyrmion.

Fig. 6.12, shows a comparison between the experimental results of the thickness dependent helix period with a model calculation. The calculation parameters used are A =30 pJ m^{-1}, D =0.1 mJ m^{-2} and M_s =445 kA m^{-1}. The trend of the experimental results are reproduced. The actual magnetic structure may be distorted from the assumed simple sinusoidal Bloch-like helix. Also, the calculated λ - t relationship results from a complex competition between Heisenberg exchange, DMI and the dipolar and anisotropy energies terms, so the extraction of the magnetic parameters is difficult. Thus, the parameters used above are for a qualitative understanding.

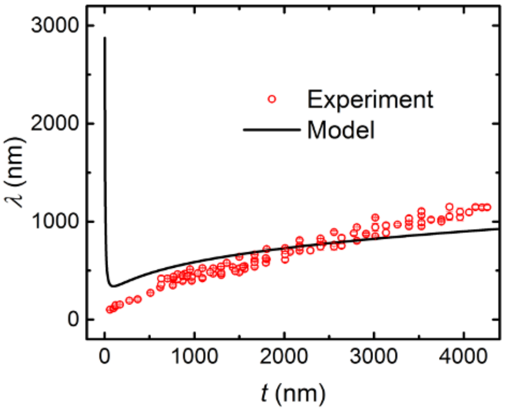

Figure 6.12: Comparison of the helix period λ as a function of thickness between experiment and model. The parameters used in this calculation are: A =30 pJ m^{-1}, D =0.1 mJ m^{-2} and M_s =445 kA m^{-1}.

6.4 Discussion

The thickness-dependent antiskyrmion size and helix period reported in this work are distinct from other material systems, because of the fundamental differences in their physical origin. In systems that show magnetic bubbles [83, 84, 85], there is no DMI, so the magnetic structure is achiral. For a certain thickness, the size of the bubble will has a large dependence on the external magnetic field amplitude. In a recent work from our group, we reported the experimental observation of Néel skyrmions in PtMnGa, which has a crystal structure belong to the C_{3v} group [38]. The Néel skyrmion size was also found to be dependent on thickness. However, LTEM measurements shown the boundary width of the Néel skyrmion is small compared to the skyrmion size, so the thickness-size relationship in this system is more similar to the conventional magnetic "bubbles". In the system of interfacial DMI [23, 24], although some theoretical studies suggest that dipolar interactions could play an important role [90, 91] as the magnetic layer thickness is changed, the effective DMI strength also changes (decreases inversely with thickness) so measurements in these systems is limited to a thickness range of just a nanometer or so.

In B20 material systems [30, 37, 31, 82], in all the three coordinate directions, the DMI has a non-zero value. Thus, a twist structure will exist in the skyrmion tubes, as simulated in the last chapter. This twist structure could weaken the influence of the magnetic dipolar interaction. So, the thickness's influence on skyrmion size is also weak. Another type of twisted magnetic structure, reported in magnetic multilayer systems [92, 93, 54], is called 'Néel Cap'. It can also be named as 'horizontal Bloch line' [6]. However, these dipolar induced structures are at the surface and will not influence much as compared to those induced by DMI. Nevertheless, this effect may be the reason for the small differences between our experimental results and model calculations.

So, to date, the D_{2d} antiskyrmion material is the only system that has both a volume type DMI and magnetic dipolar interactions that together have a large influence. This uniqueness results in the high stability of antiskymrions and the large size tunability shown in this chapter. Meanwhile, the competition between the D_{2d} volume DMI and magnetic dipolar interaction energy terms can even lead to the stabilization of metastable elliptical Bloch skyrmions [94, 95].

6.5 Summary

In conclusion, this chapter shows the importance of the magneto-dipolar interaction which can influence the size of non-collinear magnetic structures, depending on the crystal symmetry. The high tunability of the size of the antiskyrmion and helical period in the D_{2d} system is not only remarkable but makes these materials of great interest for spintronic applications. These results also clearly show how magnetization, instead of DMI, can tune the size of antiskyrmions, thereby providing a new path for the manipulation of non-collinear magnetic structures.

Chapter 7

Conclusion and outlook

In this thesis, I have summarized our studies on the first experimental discovery of antiskyrmions as well as subsequent work.

We have studied samples fabricated from high-quality crystals of $Mn_{1.4}PtSn$ and $Mn_{1.4}Pt_{0.9}Pd_{0.1}Sn$ which exhibit the D_{2d} crystal symmetry. Based on unique LTEM contrast patterns, antiskyrmions are shown to exist in this and related materials. From micromagnetic simulations and LTEM image calculations, this unique LTEM contrast pattern is shown to indicate the stabilization of antiskyrmions. Temperature and field-dependent phase diagrams are measured and analyzed to show the unusual and highly interesting properties of antiskyrmions, especially when compared to skyrmions which have been extensively studied in earlier work.

We studied the thickness-dependent temperature and field phase diagrams in wedged shape lamellae. The antiskyrmion shows much a much larger stability than Bloch skyrmions in the heavily explored B20 material systems. Micromagnetic simulations were carried out that shows that such a large stability originates from the zero value of DMI along the [001] crystal direction in the low symmetry D_{2d} material system.

We further showed that not only antiskyrmions can be stabilized over a large thickness range, but that the size of antiskyrmion can be widely tuned. From LTEM and MFM measurements, the antiskyrmion size can be tuned over one order of magnitude. A model was developed to show that such a thickness-dependent size behavior originates from the competition between the D_{2d} type of DMI and long-range magnetic dipolar interactions, which is unique to the D_{2d} material system.

The discovery of skyrmions is continuing, and the number of members of the skyrmion Zootopia is still increasing. Till now, the well-known skyrmion types are Bloch skyrmion in B20 systems, Néel skyrmion in C_{nv} or multilayer systems, antiskyrmions in D_{2d} material systems and 'bi-skyrmion' in centrosymmetric material systems. As shown in Chapter 2, lots of other DMI types exist in other material systems so that other types of skyrmion remain to be explored. The dynamical behavior of skyrmions, especially their current-induced motion remains to be explored for many distinct types of skyrmions. They have considerable potential for device applications and are of great interest for both fundamental physics as well as many different spintronics applications.

Appendix DMI energy term under various crystal

According to the derivations discussed in Chapter 2.2, generally, the DMI energy term can be written as:

$$\begin{aligned}H_{DMI} = & D_{xx}\left(M_y\frac{\partial M_z}{\partial x} - M_z\frac{\partial M_y}{\partial x}\right) + D_{xy}\left(M_y\frac{\partial M_z}{\partial y} - M_z\frac{\partial M_y}{\partial y}\right) + D_{xz}\left(M_y\frac{\partial M_z}{\partial z} - M_z\frac{\partial M_y}{\partial z}\right) \\ & + D_{yx}\left(M_z\frac{\partial M_x}{\partial x} - M_x\frac{\partial M_z}{\partial x}\right) + D_{yy}\left(M_z\frac{\partial M_x}{\partial y} - M_x\frac{\partial M_z}{\partial y}\right) + D_{yz}\left(M_z\frac{\partial M_x}{\partial z} - M_x\frac{\partial M_z}{\partial z}\right) \\ & + D_{zx}\left(M_x\frac{\partial M_y}{\partial x} - M_y\frac{\partial M_x}{\partial x}\right) + D_{zy}\left(M_x\frac{\partial M_y}{\partial y} - M_y\frac{\partial M_x}{\partial y}\right) + D_{zz}\left(M_x\frac{\partial M_y}{\partial z} - M_y\frac{\partial M_x}{\partial z}\right)\end{aligned} \tag{A.1}$$

So, we use a matrix to present the DMI parameters

$$\begin{pmatrix} D_{xx} & D_{xy} & D_{xz} \\ D_{yx} & D_{yy} & D_{yz} \\ D_{zx} & D_{zy} & D_{zz} \end{pmatrix} \tag{A.2}$$

In a centrosymmetric crystal structure, the DMI term has a zero value. Below is the list of DMI parameter matrixs for all point groups.

$$
\begin{array}{lll}
C_2 \begin{pmatrix} D_{11} & 0 & D_{13} \\ 0 & D_{22} & 0 \\ D_{31} & 0 & D_{33} \end{pmatrix} &
C_s \begin{pmatrix} 0 & D_{12} & 0 \\ D_{21} & 0 & D_{23} \\ 0 & D_{32} & 0 \end{pmatrix} &
D_2 \begin{pmatrix} D_{11} & 0 & 0 \\ 0 & D_{22} & 0 \\ 0 & 0 & D_{33} \end{pmatrix} \\
C_{2v} \begin{pmatrix} 0 & D_{12} & 0 \\ D_{21} & 0 & 0 \\ 0 & 0 & 0 \end{pmatrix} &
C_4 \begin{pmatrix} D_{11} & -D_{21} & 0 \\ D_{21} & D_{11} & 0 \\ 0 & 0 & D_{33} \end{pmatrix} &
S_4 \begin{pmatrix} D_{11} & D_{21} & 0 \\ D_{21} & -D_{11} & 0 \\ 0 & 0 & 0 \end{pmatrix} \\
D_4 \begin{pmatrix} D_{11} & 0 & 0 \\ 0 & D_{11} & 0 \\ 0 & 0 & D_{33} \end{pmatrix} &
C_{4v} \begin{pmatrix} 0 & -D_{21} & 0 \\ D_{21} & 0 & 0 \\ 0 & 0 & 0 \end{pmatrix} &
D_{2d} \begin{pmatrix} D_{11} & 0 & 0 \\ 0 & -D_{11} & 0 \\ 0 & 0 & 0 \end{pmatrix} \\
C_3 \begin{pmatrix} D_{11} & -D_{21} & 0 \\ D_{21} & D_{11} & 0 \\ 0 & 0 & D_{33} \end{pmatrix} &
D_3 \begin{pmatrix} D_{11} & 0 & 0 \\ 0 & D_{11} & 0 \\ 0 & 0 & D_{33} \end{pmatrix} &
C_{3v} \begin{pmatrix} 0 & -D_{21} & 0 \\ D_{21} & 0 & 0 \\ 0 & 0 & 0 \end{pmatrix} \\
C_6 \begin{pmatrix} D_{11} & -D_{21} & 0 \\ D_{21} & D_{11} & 0 \\ 0 & 0 & D_{33} \end{pmatrix} &
C_{3h} \begin{pmatrix} 0 & 0 & 0 \\ 0 & 0 & 0 \\ 0 & 0 & 0 \end{pmatrix} &
D_6 \begin{pmatrix} D_{11} & 0 & 0 \\ 0 & D_{11} & 0 \\ 0 & 0 & D_{33} \end{pmatrix} \\
C_{6v} \begin{pmatrix} 0 & -D_{21} & 0 \\ D_{21} & 0 & 0 \\ 0 & 0 & 0 \end{pmatrix} &
D_{3h} \begin{pmatrix} 0 & 0 & 0 \\ 0 & 0 & 0 \\ 0 & 0 & 0 \end{pmatrix} &
T \begin{pmatrix} D_{11} & 0 & 0 \\ 0 & D_{11} & 0 \\ 0 & 0 & D_{11} \end{pmatrix} \\
O \begin{pmatrix} D_{11} & 0 & 0 \\ 0 & D_{11} & 0 \\ 0 & 0 & D_{11} \end{pmatrix} &
T_d \begin{pmatrix} 0 & 0 & 0 \\ 0 & 0 & 0 \\ 0 & 0 & 0 \end{pmatrix} &
\end{array}
\tag{A.3}
$$

Bibliography

[1] Stuart Parkin and See-Hun Yang. Memory on the racetrack. *Nature nanotechnology*, 10(3):195–198, 2015.

[2] Christian H Back, Vincent Cros, Hubert Ebert, Karin Everschor-Sitte, Albert Fert, Markus Garst, Tainping Ma, Sergiy Mankovsky, Theodore Monchesky, Maxim V Mostovoy, et al. The 2020 skyrmionics roadmap. *Journal of Physics D: Applied Physics*, 2020.

[3] Albert Fert. Nobel Lecture: Origin, development, and future of spintronics. *Reviews of Modern Physics*, 80(4):1517, 2008.

[4] Stuart Parkin, Xin Jiang, Christian Kaiser, Alex Panchula, Kevin Roche, and Mahesh Samant. Magnetically engineered spintronic sensors and memory. *Proceedings of the IEEE*, 91(5):661–680, 2003.

[5] YJ Song, JH Lee, HC Shin, KH Lee, K Suh, JR Kang, SS Pyo, HT Jung, SH Hwang, GH Koh, et al. Highly functional and reliable 8Mb STT-MRAM embedded in 28nm logic. In *2016 IEEE International Electron Devices Meeting (IEDM)*, pages 27–2. IEEE, 2016.

[6] AP Malozemoff and JC Slonczewski. *Magnetic Domain Walls in Bubble Materials: Advances in Materials and Device Research*, volume 1. Academic Press, 2016.

[7] See-Hun Yang and Stuart Parkin. Novel domain wall dynamics in synthetic antiferromagnets. *Journal of Physics: Condensed Matter*, 29(30):303001, 2017.

[8] XZ Yu, Yoshinori Onose, Naoya Kanazawa, JH Park, JH Han, Yoshio Matsui, Naoto Nagaosa, and Yoshinori Tokura. Real-space observation of a two-dimensional skyrmion crystal. *Nature*, 465(7300):901–904, 2010.

[9] Gong Chen, Arantzazu Mascaraque, Alpha T N'Diaye, and Andreas K Schmid. Room temperature skyrmion ground state stabilized through interlayer exchange coupling. *Applied Physics Letters*, 106(24):242404, 2015.

[10] István Kézsmárki, Sándor Bordács, P Milde, E Neuber, LM Eng, JS White, Henrik M Rønnow, CD Dewhurst, M Mochizuki, K Yanai, et al. Néel-type skyrmion lattice with confined orientation in the polar magnetic semiconductor GaV_4S_8. *Nature materials*, 14(11):1116–1122, 2015.

[11] IE Dzialoshinskii. Thermodynamic theory of weak ferromagnetism in antiferromagnetic substances. *Soviet Physics Jetp-Ussr*, 5(6):1259–1272, 1957.

[12] Tôru Moriya. Anisotropic superexchange interaction and weak ferromagnetism. *Physical review*, 120(1):91, 1960.

[13] Naoto Nagaosa and Yoshinori Tokura. Topological properties and dynamics of magnetic skyrmions. *Nature nanotechnology*, 8(12):899, 2013.

[14] João Sampaio, Vincent Cros, Stanislas Rohart, André Thiaville, and Albert Fert. Nucleation, stability and current-induced motion of isolated magnetic skyrmions in nanostructures. *Nature nanotechnology*, 8(11):839–844, 2013.

[15] Takashi Kurumaji, Taro Nakajima, Victor Ukleev, Artem Feoktystov, Taka-hisa Arima, Kazuhisa Kakurai, and Yoshinori Tokura. Néel-type skyrmion lattice in the tetragonal polar magnet $VOSe_2O_5$. *Physical review letters*, 119(23):237201, 2017.

[16] Nicola A Spaldin. *Magnetic materials: fundamentals and applications.* Cambridge university press, 2010.

[17] Joachim Stöhr and Hans Christoph Siegmann. *Magnetism: from fundamentals to nanoscale dynamics*, volume 152. Springer Science & Business Media, 2007.

[18] S Blundell. Magnetism in condensed matter: oxford master series. *Condensed Matter Physics (Oxford Series Publications, 2001)*, page 29, 2001.

[19] DIETER Suess, JOSEF Fidler, and THOMAS Schrefl. Micromagnetic simulation of magnetic materials. *Handbook of Magnetic Materials*, 16:41–125, 2006.

[20] Robin Bläsing, Tianping Ma, See-Hun Yang, Chirag Garg, Fasil Kidane Dejene, Alpha T N'Diaye, Gong Chen, Kai Liu, and Stuart SP Parkin. Exchange coupling torque in ferrimagnetic Co/Gd bilayer maximized near angular momentum compensation temperature. *Nature communications*, 9(1):1–8, 2018.

[21] Alex Hubert and Rudolf Schäfer. *Magnetic domains: the analysis of magnetic microstructures*. Springer Science & Business Media, 2008.

[22] Y Yafet and EM Gyorgy. Ferromagnetic strip domains in an atomic monolayer. *Physical Review B*, 38(13):9145, 1988.

[23] G Chen, J Zhu, A Quesada, J Li, AT N'Diaye, Y Huo, TP Ma, Y Chen, HY Kwon, C Won, et al. Novel chiral magnetic domain wall structure in Fe/Ni/Cu (001) films. *Physical review letters*, 110(17):177204, 2013.

[24] Gong Chen, Tianping Ma, Alpha T N'Diaye, Heeyoung Kwon, Changyeon Won, Yizheng Wu, and Andreas K Schmid. Tailoring the chirality of magnetic domain walls by interface engineering. *Nature communications*, 4(1):1–6, 2013.

[25] Luqiao Liu, Chi-Feng Pai, Y Li, HW Tseng, DC Ralph, and RA Buhrman. Spin-torque switching with the giant spin Hall effect of tantalum. *Science*, 336(6081):555–558, 2012.

[26] Wanjun Jiang, Pramey Upadhyaya, Wei Zhang, Guoqiang Yu, M Benjamin Jungfleisch, Frank Y Fradin, John E Pearson, Yaroslav Tserkovnyak, Kang L Wang, Olle Heinonen, et al. Blowing magnetic skyrmion bubbles. *Science*, 349(6245):283–286, 2015.

[27] SX Huang and CL Chien. Extended skyrmion phase in epitaxial FeGe (111) thin films. *Physical review letters*, 108(26):267201, 2012.

[28] Sebastian Mühlbauer, Benedikt Binz, F Jonietz, Christian Pfleiderer, Achim Rosch, Anja Neubauer, Robert Georgii, and Peter Böni. Skyrmion lattice in a chiral magnet. *Science*, 323(5916):915–919, 2009. URL: `https://science.sciencemag.org/content/323/5916/915`.

[29] Niklas Romming, Christian Hanneken, Matthias Menzel, Jessica E Bickel, Boris Wolter, Kirsten von Bergmann, André Kubetzka, and Roland Wiesendanger. Writing and deleting single magnetic skyrmions. *Science*, 341(6146):636–639, 2013. URL: https://science.sciencemag.org/content/341/6146/636.

[30] XZ Yu, Naoya Kanazawa, Yoshinori Onose, K Kimoto, WZ Zhang, Shintaro Ishiwata, Yoshio Matsui, and Yoshinori Tokura. Near room-temperature formation of a skyrmion crystal in thin-films of the helimagnet FeGe. *Nature materials*, 10(2):106–109, 2011.

[31] K Shibata, XZ Yu, T Hara, D Morikawa, N Kanazawa, K Kimoto, S Ishiwata, Y Matsui, and Y Tokura. Towards control of the size and helicity of skyrmions in helimagnetic alloys by spin–orbit coupling. *Nature nanotechnology*, 8(10):723–728, 2013.

[32] Masahito Mochizuki, XZ Yu, Shinichiro Seki, Naoya Kanazawa, Wataru Koshibae, Jiadong Zang, Maxim Mostovoy, Yoshinori Tokura, and Naoto Nagaosa. Thermally driven ratchet motion of a skyrmion microcrystal and topological magnon Hall effect. *Nature materials*, 13(3):241–246, 2014.

[33] Xiuzhen Yu, Akiko Kikkawa, Daisuke Morikawa, Kiyou Shibata, Yusuke Tokunaga, Yasujiro Taguchi, and Yoshinori Tokura. Variation of skyrmion forms and their stability in MnSi thin plates. *Physical Review B*, 91(5):054411, 2015.

[34] Shinichiro Seki, XZ Yu, S Ishiwata, and Yoshinori Tokura. Observation of skyrmions in a multiferroic material. *Science*, 336(6078):198–201, 2012. URL: https://science.sciencemag.org/content/336/6078/198.

[35] Filipp N Rybakov, Aleksandr B Borisov, Stefan Blügel, and Nikolai S Kiselev. New type of stable particlelike states in chiral magnets. *Physical review letters*, 115(11):117201, 2015.

[36] AO Leonov, Yoshihiko Togawa, TL Monchesky, AN Bogdanov, J Kishine, Y Kousaka, M Miyagawa, T Koyama, Jun Akimitsu, Ts Koyama, et al. Chiral surface twists and skyrmion stability in

nanolayers of cubic helimagnets. *Physical review letters*, 117(8):087202, 2016.

[37] Fengshan Zheng, Filipp N Rybakov, Aleksandr B Borisov, Dongsheng Song, Shasha Wang, Zi-An Li, Haifeng Du, Nikolai S Kiselev, Jan Caron, Andras Kovacs, et al. Experimental observation of chiral magnetic bobbers in B20-type FeGe. *Nature nanotechnology*, 13(6):451–455, 2018.

[38] Abhay K Srivastava, Parul Devi, Ankit K Sharma, Tianping Ma, Hakan Deniz, Holger L Meyerheim, Claudia Felser, and Stuart SP Parkin. Observation of Robust Néel Skyrmions in Metallic PtMnGa. *Advanced Materials*, page 1904327, 2019.

[39] XZ Yu, Y Tokunaga, Y Kaneko, WZ Zhang, K Kimoto, Y Matsui, Y Taguchi, and Y Tokura. Biskyrmion states and their current-driven motion in a layered manganite. *Nature communications*, 5(1):1–7, 2014.

[40] James C Loudon, Alison C Twitchett-Harrison, David Cortés-Ortuño, Max T Birch, Luke A Turnbull, Aleš Štefančič, Feodor Y Ogrin, Erick O Burgos-Parra, Nicholas Bukin, Angus Laurenson, et al. Do Images of Biskyrmions Show Type-II Bubbles? *Advanced Materials*, 31(16):1806598, 2019.

[41] XZ Yu, W Koshibae, Y Tokunaga, K Shibata, Y Taguchi, N Nagaosa, and Y Tokura. Transformation between meron and skyrmion topological spin textures in a chiral magnet. *Nature*, 564(7734):95–98, 2018.

[42] Xichao Zhang, Jing Xia, Yan Zhou, Xiaoxi Liu, Han Zhang, and Motohiko Ezawa. Skyrmion dynamics in a frustrated ferromagnetic film and current-induced helicity locking-unlocking transition. *Nature communications*, 8(1):1–10, 2017.

[43] XZ Yu, Naoya Kanazawa, WZ Zhang, T Nagai, Toru Hara, Koji Kimoto, Yoshio Matsui, Yoshinori Onose, and Yoshinori Tokura. Skyrmion flow near room temperature in an ultralow current density. *Nature communications*, 3(1):1–6, 2012.

[44] Seonghoon Woo, Kai Litzius, Benjamin Krüger, Mi-Young Im, Lucas Caretta, Kornel Richter, Maxwell Mann, Andrea Krone, Robert M

Reeve, Markus Weigand, et al. Observation of room-temperature magnetic skyrmions and their current-driven dynamics in ultrathin metallic ferromagnets. *Nature materials*, 15(5):501–506, 2016.

[45] Wanjun Jiang, Xichao Zhang, Guoqiang Yu, Wei Zhang, Xiao Wang, M Benjamin Jungfleisch, John E Pearson, Xuemei Cheng, Olle Heinonen, Kang L Wang, et al. Direct observation of the skyrmion Hall effect. *Nature Physics*, 13(2):162–169, 2017.

[46] Kai Litzius, Ivan Lemesh, Benjamin Krüger, Pedram Bassirian, Lucas Caretta, Kornel Richter, Felix Büttner, Koji Sato, Oleg A Tretiakov, Johannes Förster, et al. Skyrmion Hall effect revealed by direct time-resolved X-ray microscopy. *Nature Physics*, 13(2):170–175, 2017.

[47] Yuushou Hirata, Duck-Ho Kim, Se Kwon Kim, Dong-Kyu Lee, Se-Hyeok Oh, Dae-Yun Kim, Tomoe Nishimura, Takaya Okuno, Yasuhiro Futakawa, Hiroki Yoshikawa, et al. Vanishing skyrmion Hall effect at the angular momentum compensation temperature of a ferrimagnet. *Nature nanotechnology*, 14(3):232–236, 2019.

[48] Tanja Graf, Claudia Felser, and Stuart SP Parkin. Simple rules for the understanding of Heusler compounds. *Progress in solid state chemistry*, 39(1):1–50, 2011.

[49] Ajaya K Nayak, Michael Nicklas, Stanislav Chadov, Panchanana Khuntia, Chandra Shekhar, Adel Kalache, Michael Baenitz, Yurii Skourski, Veerendra K Guduru, Alessandro Puri, et al. Design of compensated ferrimagnetic Heusler alloys for giant tunable exchange bias. *Nature materials*, 14(7):679–684, 2015.

[50] Olga Meshcheriakova, Stanislav Chadov, AK Nayak, UK Rößler, Jürgen Kübler, G André, AA Tsirlin, J Kiss, Steffen Hausdorf, Adel Kalache, et al. Large noncollinearity and spin reorientation in the novel Mn_2RhSn Heusler magnet. *Physical review letters*, 113(8):087203, 2014.

[51] Gy J Vida, E Simon, L Rózsa, K Palotás, and L Szunyogh. Domain-wall profiles in $Co/Ir_n/Pt$ (111) ultrathin films: Influence of the Dzyaloshinskii-Moriya interaction. *Physical Review B*, 94(21):214422, 2016.

[52] Alexei N Bogdanov and DA Yablonskii. Thermodynamically stable "vortices" in magnetically ordered crystals. The mixed state of magnets. *Zh. Eksp. Teor. Fiz*, 95(1):178, 1989.

[53] A Bogdanov and A Hubert. Thermodynamically stable magnetic vortex states in magnetic crystals. *Journal of magnetism and magnetic materials*, 138(3):255–269, 1994.

[54] SA Montoya, S Couture, JJ Chess, JCT Lee, N Kent, D Henze, SK Sinha, M-Y Im, SD Kevan, P Fischer, et al. Tailoring magnetic energies to form dipole skyrmions and skyrmion lattices. *Physical Review B*, 95(2):024415, 2017.

[55] Michael R. Scheinfein. LLG User Manual, 2015.

[56] Andrew J Newell, Wyn Williams, and David J Dunlop. A generalization of the demagnetizing tensor for nonuniform magnetization. *Journal of Geophysical Research: Solid Earth*, 98(B6):9551–9555, 1993.

[57] Karl Fabian, Andreas Kirchner, Wyn Williams, Franz Heider, Thomas Leibl, and Alex Huber. Three-dimensional micromagnetic calculations for magnetite using FFT. *Geophysical Journal International*, 124(1):89–104, 1996.

[58] Arne Vansteenkiste and Ben Van de Wiele. MuMax: A new high-performance micromagnetic simulation tool. *Journal of Magnetism and Magnetic Materials*, 323(21):2585–2591, 2011.

[59] Michael J Donahue and MJ Donahue. *OOMMF user's guide, version 1.0*. US Department of Commerce, National Institute of Standards and Technology, 1999.

[60] WH Escovitz, TR Fox, and R Levi-Setti. Scanning transmission ion microscope with a field ion source. *Proceedings of the National Academy of Sciences*, 72(5):1826–1828, 1975.

[61] JN Chapman. The investigation of magnetic domain structures in thin foils by electron microscopy. *Journal of Physics D: Applied Physics*, 17(4):623, 1984.

[62] Yakir Aharonov and David Bohm. Significance of electromagnetic potentials in the quantum theory. *Physical Review*, 115(3):485, 1959.

[63] M Beleggia, PF Fazzini, and G Pozzi. A Fourier approach to fields and electron optical phase-shifts calculations. *Ultramicroscopy*, 96(1):93–103, 2003.

[64] M Beleggia and Y Zhu. Electron-optical phase shift of magnetic nanoparticles I. Basic concepts. *Philosophical Magazine*, 83(8):1045–1057, 2003.

[65] Anjan Soumyanarayanan, M Raju, AL Gonzalez Oyarce, Anthony KC Tan, Mi-Young Im, Alexander Paul Petrović, Pin Ho, KH Khoo, M Tran, CK Gan, et al. Tunable room-temperature magnetic skyrmions in Ir/Fe/Co/Pt multilayers. *Nature materials*, 16(9):898–904, 2017.

[66] U Hartmann. Magnetic force microscopy. *Annual review of materials science*, 29(1):53–87, 1999.

[67] John Kerr. On rotation of the plane of polarization by reflection from the pole of a magnet. *The London, Edinburgh, and Dublin Philosophical Magazine and Journal of Science*, 3(19):321–343, 1877.

[68] J Stöhr. Exploring the microscopic origin of magnetic anisotropies with X-ray magnetic circular dichroism (XMCD) spectroscopy. *Journal of Magnetism and Magnetic Materials*, 200(1-3):470–497, 1999.

[69] Markus Weigand. *Realization of a new magnetic scanning X-ray microscope and investigation of Landau structures under pulsed field excitation.* Cuvillier Verlag, 2015.

[70] Ulrich K Roessler, AN Bogdanov, and C Pfleiderer. Spontaneous skyrmion ground states in magnetic metals. *Nature*, 442(7104):797–801, 2006.

[71] S Zhang, Amanda K Petford-Long, and C Phatak. Creation of artificial skyrmions and antiskyrmions by anisotropy engineering. *Scientific reports*, 6:31248, 2016.

[72] Toshiaki Tanigaki, Kiyou Shibata, Naoya Kanazawa, Xiuzhen Yu, Yoshinori Onose, Hyun Soon Park, Daisuke Shindo, and Yoshinori Tokura.

Real-space observation of short-period cubic lattice of skyrmions in MnGe. *Nano letters*, 15(8):5438–5442, 2015.

[73] Ajaya K Nayak, Vivek Kumar, Tianping Ma, Peter Werner, Eckhard Pippel, Roshnee Sahoo, Franoise Damay, Ulrich K Rößler, Claudia Felser, and Stuart SP Parkin. Magnetic antiskyrmions above room temperature in tetragonal Heusler materials. *Nature*, 548(7669):561–566, 2017.

[74] Marco Beleggia, MA Schofield, Y Zhu, M Malac, Z Liu, and M Freeman. Quantitative study of magnetic field distribution by electron holography and micromagnetic simulations. *Applied physics letters*, 83(7):1435–1437, 2003.

[75] Stephanie K Walton, Katharina Zeissler, Will R Branford, and Solveig Felton. MALTS: A tool to simulate Lorentz Transmission Electron Microscopy from micromagnetic simulations. *IEEE transactions on magnetics*, 49(8):4795–4800, 2013.

[76] Fumitaka Kagawa, Hiroshi Oike, Wataru Koshibae, Akiko Kikkawa, Yoshihiro Okamura, Yasujiro Taguchi, Naoto Nagaosa, and Yoshinori Tokura. Current-induced viscoelastic topological unwinding of metastable skyrmion strings. *Nature communications*, 8(1):1–8, 2017.

[77] Rana Saha, Abhay K Srivastava, Tianping Ma, Jagannath Jena, Peter Werner, Vivek Kumar, Claudia Felser, and Stuart SP Parkin. Intrinsic stability of magnetic anti-skyrmions in the tetragonal inverse Heusler compound $Mn_{1.4}Pt_{0.9}Pd_{0.1}Sn$. *Nature communications*, 10(1):1–7, 2019.

[78] Filipp N Rybakov, Aleksandr B Borisov, Stefan Blügel, and Nikolai S Kiselev. New spiral state and skyrmion lattice in 3D model of chiral magnets. *New Journal of Physics*, 18(4):045002, 2016.

[79] FN Rybakov, AB Borisov, and AN Bogdanov. Three-dimensional skyrmion states in thin films of cubic helimagnets. *Physical Review B*, 87(9):094424, 2013.

[80] Adam S Ahmed, James Rowland, Bryan D Esser, Sarah R Dunsiger, David W McComb, Mohit Randeria, and Roland K Kawakami. Chiral bobbers and skyrmions in epitaxial FeGe/Si (111) films. *Physical Review Materials*, 2(4):041401, 2018.

[81] S Rohart and A Thiaville. Skyrmion confinement in ultrathin film nanostructures in the presence of Dzyaloshinskii-Moriya interaction. *Physical Review B*, 88(18):184422, 2013.

[82] Hyun Soon Park, Xiuzhen Yu, Shinji Aizawa, Toshiaki Tanigaki, Tetsuya Akashi, Yoshio Takahashi, Tsuyoshi Matsuda, Naoya Kanazawa, Yoshinori Onose, Daisuke Shindo, et al. Observation of the magnetic flux and three-dimensional structure of skyrmion lattices by electron holography. *Nature nanotechnology*, 9(5):337, 2014.

[83] Zdeněk Málek and Vladimír Kamberskỳ. On the theory of the domain structure of thin films of magnetically uni-axial materials. *Cechoslovackij fiziceskij zurnal*, 8(4):416–421, 1958.

[84] JA Cape and GW Lehman. Magnetic domain structures in thin uniaxial plates with perpendicular easy axis. *Journal of Applied Physics*, 42(13):5732–5756, 1971.

[85] PJ Grundy and SR Herd. Lorentz microscopy of bubble domains and changes in domain wall state in hexaferrites. *physica status solidi (a)*, 20(1):295–307, 1973.

[86] Wenhong Wang, Ying Zhang, Guizhou Xu, Licong Peng, Bei Ding, Yue Wang, Zhipeng Hou, Xiaoming Zhang, Xiyang Li, Enke Liu, et al. A centrosymmetric hexagonal magnet with superstable biskyrmion magnetic nanodomains in a wide temperature range of 100–340 K. *Advanced Materials*, 28(32):6887–6893, 2016.

[87] Xiuzhen Yu, Maxim Mostovoy, Yusuke Tokunaga, Weizhu Zhang, Koji Kimoto, Yoshio Matsui, Yoshio Kaneko, Naoto Nagaosa, and Yoshinori Tokura. Magnetic stripes and skyrmions with helicity reversals. *Proceedings of the National Academy of Sciences*, 109(23):8856–8860, 2012.

[88] Tianping Ma, Ankit K Sharma, Rana Saha, Abhay K Srivastava, Peter Werner, Praveen Vir, Vivek Kumar, Claudia Felser, and Stuart SP Parkin. Tunable Magnetic Antiskyrmion Size and Helical Period from Nanometers to Micrometers in a D_{2d} Heusler Compound. *Advanced Materials*, page 2002043, 2020.

[89] Amikam Aharoni et al. *Introduction to the Theory of Ferromagnetism*, volume 109. Clarendon Press, 2000.

[90] Ivan Lemesh, Felix Büttner, and Geoffrey SD Beach. Accurate model of the stripe domain phase of perpendicularly magnetized multilayers. *Physical Review B*, 95(17):174423, 2017.

[91] Felix Büttner, Ivan Lemesh, and Geoffrey SD Beach. Theory of isolated magnetic skyrmions: From fundamentals to room temperature applications. *Scientific reports*, 8(1):1–12, 2018.

[92] William Legrand, Nathan Ronceray, Nicolas Reyren, Davide Maccariello, Vincent Cros, and Albert Fert. Modeling the shape of axisymmetric skyrmions in magnetic multilayers. *Physical Review Applied*, 10(6):064042, 2018.

[93] Ivan Lemesh and Geoffrey SD Beach. Twisted domain walls and skyrmions in perpendicularly magnetized multilayers. *Physical Review B*, 98(10):104402, 2018.

[94] Licong Peng, Rina Takagi, Wataru Koshibae, Kiyou Shibata, Kiyomi Nakajima, Taka-hisa Arima, Naoto Nagaosa, Shinichiro Seki, Xiuzhen Yu, and Yoshinori Tokura. Controlled transformation of skyrmions and antiskyrmions in a non-centrosymmetric magnet. *Nature Nanotechnology*, 15(3):181–186, 2020.

[95] Jagannath Jena, Börge Göbel, Tianping Ma, Vivek Kumar, Rana Saha, Ingrid Mertig, Claudia Felser, and Stuart SP Parkin. Elliptical Bloch skyrmion chiral twins in an antiskyrmion system. *Nature communications*, 11(1):1–9, 2020.

List of figures

1.1 Illustration of magnetic ordering. 14
1.2 Illustration of the magnetic structure of different types of magnetic domain walls. 17
1.3 Chirality of magnetic domain wall as a function of Ir inserting layer thickness in Ni/[Co/Ni]$_2$/Ir/Pt(111) sample structure. . 18
1.4 Typical neutron small-angle scattering intensity, which indicating the stabilization of skyrmion lattice. 20
1.5 Simulation and experiment result of the magnetization distribution of helix and skyrmion lattice. 21
1.6 Simulation and experiment result of temperature and field dependence of the magnetic structure phase diagram. 22
1.7 Skyrmion magnetic structures measured by SP-STM technique. 23
1.8 Thickness dependence of the skyrmion lattice phase in the temperature-field phase diagram in FeGe. 24
1.9 The discovery of magnetic skyrmion in multiferroic material Cu_2OSeO_3. 25
1.10 Schematic drawing of the magnetization and cross-section of the (a) skyrmion tube, and (b) chiral bobber. 25
1.11 Experimental confirmation of the existence of chiral bobber. . 26
1.12 Experimental confirmation of the existence of interface DMI induced Néel skyrmion. 27
1.13 Magnetic structure of a biskyrmion and its corresponding LTEM pattern. 28
1.14 Magnetic structure of square (anti)meron lattice, hexagonal skyrmion lattice, and the transition state in between. 29
1.15 Magnetic structure of skyrmions in frustrated J1-J2-J3 ferromagnetic. 29

1.16 Current-induced skyrmion motion measured by magnetic transmission soft X-ray microscopy. 30

2.1 Coordinate definition and typical magnetic topology of skyrmion. 39
2.2 Self-programmed software for Current-Induced Domain Wall Motion analysis. 45

3.1 FIB workstations. 48
3.2 A typical FIB lamella fabrication procedure. 49
3.3 Lorentz Transmission Electron Microscopy model Titan from the company FEI. 51
3.4 MFM setup with model AttoLiquid MFM I from the company Attocube. 52
3.5 Kerr microscope system from EVICO GmbH and upgraded with a variable temperature function. 54

4.1 Magnetic structure of skyrmions and antiskyrmions. 59
4.2 Simulated magnetic structure of skyrmions. 60
4.3 Simulated LTEM images as a function of Δz. 62
4.4 LTEM contrast at room temperature. 63
4.5 Room temperature antiskyrmions. 65
4.6 Simulated antiskyrmion phase as a function of H_z. 67
4.7 Simulated antiskyrmion lattice under tilt angle. 67
4.8 Antiskyrmions at 350 K and 100 K. 68
4.9 Typical results of analysis of the antiskyrmion lattice image. . 69
4.10 Antiskyrmions phase diagram and analysis. 70

5.1 Determination of three different thickness regions. 75
5.2 LTEM result at 300 K as a function of the magnetic field. . . . 75
5.3 LTEM results as a function of temperature. 76
5.4 Ratio of the area of the sample occupied by the antiskyrmion lattice. 77
5.5 Magnetic phase diagram of different thicknesses. 78
5.6 Simulation with different cell sizes. 81
5.7 Simulations result of 7 layers with $B = 2000\,\mathrm{Oe}$. 82
5.8 Simulation results of 13 layers with $B = 2000\,\mathrm{Oe}$. 82
5.9 Simulations result of13 layers with $B = 300\,\mathrm{Oe}$. 83
5.10 Summary of micromagnetic simulation results of the phase diagrams of B20 and D_{2d} systems. 84

6.1 LTEM images of $\mathrm{Mn_{1.4}PtSn}$. 89
6.2 MFM images of the helical magnetization structure in $\mathrm{Mn_{1.4}PtSn}$. 91
6.3 MFM measurements of the antiskyrmion phase. 92
6.4 Antiskyrmion size analysis 93
6.5 Comparison of helical period and antiskyrmion size. 93
6.6 Comparison of numerical and analytical results. 96
6.7 Comparison of numerical calculations with an analytical formula for various φ_0 that correspond to distinct spin textures. . 98
6.8 Model and OOMMF calculation of E_{Dip} as a function of λ. . 100
6.9 Position dependent dipolar energy density for t =200 nm. . . . 101
6.10 Position dependent dipolar energy density for λ =500 nm. . . . 102
6.11 Calculation of helix period in D_{2d} system as a function of thickness. 104
6.12 Comparison of the helix period λ as a function of thickness between experiment and model. 105

Abbreviations

AFM	Antiferromagnetism
CMN	Chiral magnetic nanostructure
CPU	Central processing unit
DMI	Dzyaloshinskii–Moriya interaction
DW	Domain Wall
FC	Field cooling
FFT	Fast-Furrier-Transformation
FIB	Focused ion beam
FM	Ferromagnetism
GMR	Giant Magnetoresistance effect
GPU	Graphics Processing Unit
GUI	Graphical User Interface
LH	Left-hand
LLG	Landau–Lifshitz–Gilbert
LTEM	Lorentz transmission electron microscopy
MAXYMUS	MAgnetic X-ray Microscope with UHV Spectroscopy
MFM	Magnetic force microscopy
ML	Monolayer
MRAM	Magnetoresistive Random Access Memory
OOMMF	The Object Oriented MicroMagnetic Framework (OOMMF) project at ITL/NIST
PMA	Perpendicular magnetic anisotropy
RH	Right-hand
SAED	Selected area diffraction patterns
SAF	Synthetic antiferromagnet
SHE	Spin Hall effect
SNAS	Small-angle neutron scattering
SP-STM	Spin-polarized scanning tunneling microscopy

SPLEEM	Spin-Polarized Low-Energy Electron Microscope
SQUID	Superconducting quantum interference device
STEM	Scanning transmission electron microscope
STM	Scanning tunneling microscopy
STXM	Scanning transmission X-ray microscopy
TIE	Transport-of-intensity equation
XRD	X-ray diffraction
ZFC	Zero field cooling

Parameter definition

$\mu_0 = 1.256\,637 \times 10^{-6}\,\mathrm{H\,m^{-1}}$	Vacuum permeability
$e = 1.602\,176 \times 10^{-19}\,\mathrm{C}$	Elementary electric charge
$m_e = 9.109\,383\,7 \times 10^{-31}\,\mathrm{kg}$	Electron rest mass
$k_b = 1.380\,649 \times 10^{-23}\,\mathrm{J\,K^{-1}}$	Blotzmann constant
$h = 6.626 \times 10^{-34}\,\mathrm{J\,s}$	Planck constant
$\mu_B = 9.274 \times 10^{-24}\,\mathrm{J\,T^{-1}}$	Bohr magneton

Curriculum vitae

Name	Tianping, Ma
Date of Birth	13th October 1988
Gender	Male
Birth Place	Nanjing, China
E-mail	tpma@mpi-halle.mpg.de

Education

2015 - present	Ph.D. in Spintronics Max-Planck Institute of Microstructure Physics, Halle (Saale), Germany Martin Luther University Halle-Wittenberg, Halle (Saale), Germany Supervisor: Prof. Stuart S.P. Parkin
2011 - 2014	Master in Condensed Matter Physics Fudan University, Shanghai, China Supervisor: Prof. Yizheng Wu
2007 - 2011	Bachelor in Applied Physics Nanjing Univ. of Science & Technology, Nanjing, China

List of publications

Thesis related publications

[1] T. Ma, A. K. Sharma, R. Saha, A. K. Srivastava, P. Werner, P. Vir, V. Kumar, C. Felser, S. S. P. Parkin, Tunable Magnetic Antiskyrmion Size and Helical Period from Nanometers to Micrometers in a D_{2d} Heusler Compound, Advanced Materials, 32 (2020) 2002043.
[2] R. Saha, A.K. Srivastava, T. Ma, J. Jena, P. Werner, V. Kumar, C. Felser, S.S. Parkin, Intrinsic stability of magnetic anti-skyrmions in the tetragonal inverse Heusler compound $Mn_{1.4}Pt_{0.9}Pd_{0.1}Sn$, Nature communications, 10 (2019) 1-7. (co-first author)
[3] A.K. Nayak, V. Kumar, T. Ma, P. Werner, E. Pippel, R. Sahoo, F. Damay, U.K. Rößler, C. Felser, S.S. Parkin, Magnetic antiskyrmions above room temperature in tetragonal Heusler materials, Nature, 548 (2017) 561-566.

Other publications during Ph.D. period

[4] A.K. Srivastava, P. Devi, A.K. Sharma, T. Ma, H. Deniz, H.L. Meyerheim, C. Felser, S.S. Parkin, Observation of Robust Néel Skyrmions in Metallic PtMnGa, Advanced Materials, 32 (2019) 1904327. (co-first author)
[5] T. Ma, Y. Yang, Z. Ding, Z. Chen, H. Zhao, P. Werner, S.S. Parkin, Y. Wu, Manipulating charge ordering in Fe_3O_4 by field cooling, Physical Review B, 95 (2017) 014103.
[6] C. Back, V. Cros, H. Ebert, K. Everschor-Sitte, A. Fert, M. Garst,

T. Ma, S. Mankovsky, T. Monchesky, M. Mostovoy, The 2020 Skyrmionics Roadmap, Journal of Physics D: Applied Physics, 53 (2020) 363001-37.
[7] J. Jena, B. Göbel, T. Ma, V. Kumar, R. Saha, I. Mertig, C. Felser, S.S. Parkin, Elliptical Bloch skyrmion chiral twins in an antiskyrmion system, Nature communications, 11 (2020) 1-9.
[8] J. Jena, R. Stinshoff, R. Saha, A.K. Srivastava, T. Ma, H. Deniz, P. Werner, C. Felser, S.S. Parkin, Observation of Magnetic Antiskyrmions in the Low Magnetization Ferrimagnet $Mn_2Rh_{0.95}Ir_{0.05}Sn$, Nano letters, 20 (2019) 59-65.
[9] R. Bläsing, T. Ma, S.-H. Yang, C. Garg, F.K. Dejene, A. T N'Diaye, G. Chen, K. Liu, S.S. Parkin, Exchange coupling torque in ferrimagnetic Co/Gd bilayer maximized near angular momentum compensation temperature, Nature communications, 9 (2018) 1-8.
[10] B. Cui, P. Werner, T. Ma, X. Zhong, Z. Wang, J.M. Taylor, Y. Zhuang, S.S. Parkin, Direct imaging of structural changes induced by ionic liquid gating leading to engineered three-dimensional meso-structures, Nature communications, 9 (2018) 1-8.
[11] Q. Li, T. Ma, M. Yang, L. Sun, S. Huang, R. Li, C. Won, Z. Qiu, Y. Wu, Field dependence of antiferromagnetic domain switching in epitaxial Fe/CoO/MgO (001) systems, Physical Review B, 96 (2017) 024420.

Other publications

[12] T. Ma, S. Zhang, Y. Yang, Z. Chen, H. Zhao, Y. Wu, Distinguishing the laser-induced spin precession excitation mechanism in Fe/MgO (001) through field orientation dependent measurements, Journal of Applied Physics, 117 (2015) 013903.
[13] Q. Li, G. Chen, T. Ma, J. Zhu, A. N'Diaye, L. Sun, T. Gu, Y. Huo, J. Liang, R. Li, Activation of antiferromagnetic domain switching in exchange-coupled Fe/CoO/MgO (001) systems, Physical Review B, 91 (2015) 134428.
[14] H. Yuan, S. Nie, T. Ma, Z. Zhang, Z. Zheng, Z. Chen, Y. Wu, J. Zhao, H. Zhao, L. Chen, Different temperature scaling of strain-induced magneto-crystalline anisotropy and Gilbert damping in Co_2FeAl film epitaxied on GaAs, Applied Physics Letters, 105 (2014) 072413.
[15] W. Liu, W. Xie, W. Guo, D. Xu, T. Hu, T. Ma, H. Yuan, Y. Wu,

H. Zhao, X. Shen, Coherent scattering of exciton polaritons and acoustic phonons in a ZnO single crystal, Physical Review B, 89 (2014) 201201.

[16] Y. Fan, X. Ma, F. Fang, J. Zhu, Q. Li, T. Ma, Y. Wu, Z. Chen, H. Zhao, G. Luepke, Photoinduced spin angular momentum transfer into an antiferromagnetic insulator, Physical Review B, 89 (2014) 094428.

[17] G. Chen, T. Ma, A.T. N'Diaye, H. Kwon, C. Won, Y. Wu, A.K. Schmid, Tailoring the chirality of magnetic domain walls by interface engineering, Nature communications, 4 (2013) 1-6.

[18] Z. Ding, J. Li, J. Zhu, T. Ma, C. Won, Y. Wu, Three-dimensional mapping of the anisotropic magnetoresistance in Fe_3O_4 single crystal thin films, Journal of Applied Physics, 113 (2013) 17B103.

[19] G. Chen, J. Zhu, A. Quesada, J. Li, A. N'Diaye, Y. Huo, T. Ma, Y. Chen, H. Kwon, C. Won, Novel chiral magnetic domain wall structure in Fe/Ni/Cu (001) films, Physical review letters, 110 (2013) 177204.

Eidesstattliche Erklärung

Ich, Tianping Ma, erkläre an Eides statt, dass ich die Arbeit selbstständig und ohne fremde Hilfe verfasst, keine anderen als die von mir angegebenen Quellen und Hilfsmittel benutzt und die den benutzten Werken wörtlich oder inhaltlich entnommenen Stellen als solche kenntlich gemacht habe.

Halle (Saale), den 05.10.2020......................................
Tianping Ma